Development of Single-Cell Techniques to Investigate Heterogeneity in Virus-Cell Interactions

By

Andrea C. Timm

A dissertation submitted in partial fulfillment of

the requirements for the degree of

Doctor of Philosophy

(Chemical and Biological Engineering)

at the

UNIVERSITY OF WISCONSIN-MADISON

2013

Date of final oral examination: 12/10/13

The dissertation is approved by the following members of the Final Oral Committee:

John Yin, Professor, Chemical Engineering

James Rawlings, Professor, Chemical Engineering

Regina Murphy, Professor, Chemical Engineering

Sean Palecek, Professor, Chemical Engineering

Nathan Sherer, Assistant Professor, Oncology

Acknowledgements

This work would not have been possible without the contributions and support of many people. I am deeply grateful for the support of my family, friends, and colleagues.

First, I would like to thank my parents, Lawrence and Marilyn Cascio, for their love and support. I would like to specifically thank my mother for showing me the value of hard work. She always did whatever was needed to get the job done, both professionally and for her family and friends. My mother is and has always been the most supportive person in my life. I thank my sister, Cheryl Cascio, for her constant encouragement. I have succeeded in part because of my desire to live up to your belief in me. I am also very grateful to Cheryl and to Justin Gutoski for being so gracious and allowing me, my husband Collin, and our cat, Jack, to live with them for the past few months while we finished school and looked for jobs. I would also like to thank my extended family, Joyce and Harold Emling, Angie and Bob Gonsowski, Jerry and Carla Bruns, and Barb and Greg Bruns for all their love and support.

I would like to thank my wonderful husband, Collin, who I was fortunate enough to be able to work with for the last five years. I have learned so much from Collin, but I appreciated working with him mostly because he loves science and he makes everyone he works with love science more. I would not have made it to this point without Collin's love and encouragement. You make me so happy and always give me something to look forward to.

I would like to thank my friends and colleagues in the Department of Chemical and Biological Engineering. Collin, Becky, Jeff, Dan, Derek, Josh, Maggie, and Claudio have been fantastic friends and hopefully we will continue to be close friends for a very long time.

I thank my undergraduate advisor, Daniel Forciniti, who is most responsible for helping me decide to pursue a PhD and for my being accepted at and choosing the University of Wisconsin.

Finally, I am grateful for the discussion and ideas from the Yin Group: Musarat Ishaq, Kathy Vielhuber, Emily Voigt, Ashley Baltes, Bahar Inankur, and Collin Timm have been great people to work with and learn from. I would like to thank my advisor, John Yin, in particular for teaching and training me for the last five years. I would also like to specifically thank Stephen Lindsay, Ankur Gupta, Fulya Akpinar, Adam Swick, and Jay Warrick, with whom I have collaborated on various projects. This work was funded in part by a Virology Training Program Fellowship, which is a great program funded by the NIH (T32 AI078985).

Abstract

Viruses cause many human diseases including the flu (influenza A), liver cancer (hepatitis C), and AIDS (HIV). A significant obstacle in developing treatments for viruses – particularly RNA viruses – is that they mutate rapidly and are able to escape the inhibitory effects of anti-viral drugs or vaccines. The resulting genetic diversity does not only allow viruses to escape treatments at the whole organism level, but is also relevant at the cellular level. Viruses have evolved a multitude of mechanisms to evade certain aspects of the innate immune response, which has in turn developed into a multifaceted, highly regulated, and redundant system that utilizes several pathogen recognition mechanisms.

The complexity of virus-host interactions is difficult to understand and characterize, particularly because there is so much cell-to-cell variability that cannot be resolved using standard population-based assays. Technological advances, particularly in live-cell microscopy have allowed researchers to make single-cell measurements that capture this variability. Here, we present one such method that utilizes a microwell based cell-culture environment, combined with a dual-color reporter system, and also employs automated imaging and high-throughput image processing and data analysis techniques to study isolated infections. Our system allows for frequent, sensitive, and quantitative measurements that provide a good representation of the state of infection and innate immune activation in isolated cells.

We employed these new methods to investigate the effects of the innate immune response and the effects of DIP co-infections on VSV replication. Using these methods we found that a small, but potentially important sub-population of cells became activated prior to our detection of infection. These fast acting cells may be important for warning their neighbors of infection, and we explored these affects by treating cells with IFN-β before infection. Combining information

gathered from multiple measures on single-cells, we identified various ways ISGs may be targeting VSV replication. Finally, by studying co-infections of single-cells with DIPs and viable VSV, we found that most cells produced infectious virus although one DIP is considered sufficient to eliminate infectious virus production. These results demonstrate that by harnessing their natural heterogeneity, we can gain insight into the complexity of virus-host interactions.

Table of Contents

Figure List

Table List

Chapter 1: Introduction

1.1 Motivation

Viruses are obligate intracellular parasites that have the ability to infect every form of life, from bacteria to humans. The ability of viruses to affect so many different organisms is due to the extraordinary diversity of virus species that includes both enveloped and non-enveloped viruses, containing genomes composed of RNA or DNA, which can also be circular or linear, segmented or non-segmented, and can range in size from as little as a few kilobases to more than 1 megabase (García-Arenal 2001; Davidson 2008; Lang 2009). Interestingly, the complexity of the virus is not correlated with the complexity of the organism it targets, nor is it predictive of the pathogenicity of the virus. The heterogeneity in virus types and structure is exceeded, however, by all the remarkable ways in which the virus and host interact.

Our particular interest is in the virus-host interactions of RNA viruses, which are best known for having highly error-prone replication processes. The result of this error-prone replication is a virus population with exceptional genetic diversity (Domingo 1985). RNA viruses cause many diseases in humans, which range in severity from the mild common cold (human rhinovirus) to more severe diseases like the flu (influenza A) and liver cancer (hepatitis C virus). Despite the frequency and severity of RNA virus infections, few treatments exist. This is largely due to the genetic variability of RNA virus populations that allows them to evolve very quickly, enabling viruses to evade detection by their host's adaptive immune system or become resistant to anti-viral drug treatments. Influenza A is an excellent example of a virus that presents challenges in the development of treatments. Influenza has pandemic potential and is a continual threat to human health. Each year a new vaccine is required to protect against infection, and many of the

classes of drugs that have been developed to treat the flu are no longer effective against many strains of the virus (Simonsen 2007; Hayden 2009; Martínez-Sobrido 2010).

Technological advances now allow us to better characterize the heterogeneity in virus populations. Deep sequencing technologies have advanced so that virus populations can be sequenced to measure the genetic diversity (Allen 2011). However, for most drug screening applications, cell-based assays are of more use because they offer a more realistic biological context for testing the drug and can also provide information about drug toxicity. Fluorescent or bioluminescent reporters are invaluable for cell-based assays. Image based readouts are generally much cheaper and quicker than other methods. Reporter genes have been added to the genomes of many viruses for easy verification of infection, and can be used for cell-based drug screening applications (Marschall 2000; Zuck 2004; Blair 2005; Towner 2005; Shaneyfelt 2006; Panchal 2010; Liu 2012). Some viral reporters have even been used to study spread of infection *in vivo* in mice (Luker 2005; Raaben 2009). Fluorescent or bioluminescent reporters allow for easier verification of anti-viral affect, but must be combined with some sort of microfluidic or microwell system in order to be useful as a high-throughput screen. For a cell-based assay, the limit, of course, is a one-cell environment. Single-cell assays have advantages beyond the small volumes and compact devices that allow screening of many drugs. Single-cell assays also allow one to analyze the variability in the virus population, and how the heterogeneity in cell populations might affect virus growth.

1.2 Background

Researchers have been studying the heterogeneity in single-cell virus production for more than eight decades. The first experiments attempting to measure the number of bacteriophage produced by a single-cell were done by Burnet in 1929 (Burnet 1929). This work was improved

upon by Delbruck in 1945, who was able to measure the burst sizes from a sufficient number of cells to determine the burst size distributions of three different bacteriophages when infecting *E. coli* (Delbruck 1945). In obtaining these distributions, Delbruck was able to show that the burst sizes was not directly related to the number of infecting particles, and that cell size alone could not predict the variability in burst sizes. Later, Lwoff et al. measured the kinetics of plaque-forming unit production for the first human virus, poliovirus, in 4 isolated monkey kidney cells (Lwoff 1955). More recently, our group was able to measure the yield distribution from hundreds of cells by infecting with a reporter virus encoding GFP and using FACS to isolate single-cells in culture wells (Zhu 2009). We were also able to measure the complete kinetics of VSV production from 12 isolated BHK cells (Timm 2012). The methods used in those two projects are too limiting to really characterize the variability in virus-host systems. Cell sorting of infectious materials presents several issues including cross-contamination of other samples and can also present a biosafety hazard. The manual techniques used to gather the kinetics of VSV production are too onerous and expensive to perform on large numbers of isolated single-cells. Hundreds or thousands of cells are required to begin to characterize the heterogeneity in these systems; and so new techniques and technologies are required to advance the cell-based methods for studying virus-host interactions and variability.

Large numbers of individual cells can be analyzed in populations by using fluorescent reporters or other staining methods. Our group and others have used in well cytometry methods, using fluorescent microscopy to isolate the reporter signal from individual cells in order to obtain flow-cytometry like results (Ecker 2004; Warrick 2013). One group was even able to correlate these measures with bacteriophage production (De Paepe 2010). An advantage of this type of analysis is that one also obtains spatial information. Snijder et al. used this type of analysis to

understand how viral endocytosis is affected by the location of a cell in a colony (Snijder 2009). Our group has used spatial information to study the relationship between innate immunity and plaque spread of viral infections (Swick, not published). Imaging cells in populations provides a more natural context, but can complicate image analysis. Micro-patterning can be used to image physically isolated cells (Chen 1997). Microwells take an additional step and permit the detection or quantification of cell secretions (Choi 2011; Torres 2013). Other microwell applications allow individual cells to be collected for further analysis, such as the collection of B-cells producing certain monoclonal antibodies (Tokimitsu 2007; Ozawa 2009), or for the development of clonal cell populations with desired properties (Lindström 2008).

The improvements to microfluidic devices for cell culture use, especially when combined with fluorescent or bioluminescent reporters, have been very useful for screening applications and for the study of virus-host heterogeneity. We believe that the methods described here improve upon existing technologies. The microwell device we use was designed for easy pipette based cell seeding and enables multiple experiments to be carried out on the same device. The assay we have developed can be easily adopted into any lab that does any live-cell microscopy and the methods of image analysis and quantification can be done using open source software. The following sections provide details on commonly used methods developed by myself and my collaborator, Jay Warrick, PhD (Warrick TBD).

1.2.1 Single-cell infection techniques

We are able to characterize a wide variety of virus-host behavior by studying the kinetics of virus production in isolated single-cell infections. The following is the general protocol used to perform these infections.

1.2.1.1 General Infection Protocol

Cultured cells grown in 75 cm^2 cell culture flasks are released with 2 ml 0.05%trypsin/0.53 mM EDTA (Cellgro) after washing with Dulbecco's phosphate buffered saline (DPBS, Gibco). The trypsin is neutralized with 8 ml infection media and the cell suspension is placed in a 15 ml conical tube. Both cell counts and the percentage of live cells are determined with the Bio-Rad TC20 Cell Counter. The cell suspension is placed on ice, cooled virus solution is added, and the suspension is mixed gently every 7 min over 30min to minimize cell aggregation and allow for virus attachment to cells without entry. Performing the adsorption in the cold allows for attachment of virions, but the infection does not proceed until the temperature is raised to 37°C (Miller 1980). The cell suspension is then prepped for a specific experiment.

1.2.1.2 Determination of effective virus titer

The effective titer for a virus is determined by following a procedure similar to the general infection protocol. Stock virus is added to a cell suspension at an approximate MOI of 1 based on the titer found using monolayer based adsorption on the desired cell line. Adsorption to cells in the cold is less efficient than a warm monolayer adsorption and the effective MOI will be less than 1. The virus solution is added to a cell suspension on ice and mixed every 7 minutes during the 30 minute incubation. This concentration is added to mimic the high multiplicity conditions of the actual infections, but reduce the probability that single cells could be infected by multiple virus particles. These cell suspensions are warmed for several minutes in a water bath set to 37 °C to allow attached virus to endocytose. The suspensions are then centrifuged at 1000 rpm for 4 min to pellet the cells. The supernatant containing any unattached virus is decanted and the pellets are re-suspended, serially diluted in un-infected cell suspensions of the same density, then added to wells of a 6-well plate. The cells are allowed 1 h to settle to attach to the bottom of the

well and then overlaid with an agar solution (0.6% Difco Agar Noble dissolved in sterile water which makes up 10% of the total volume and 90% infection media by volume). At this time, most of the cells are adhered. After incubating for 22 h, the agar gels were removed and the cells were fixed with a paraformaldehyde (PFA) solution (4% Paraformaldehyde and 5% sucrose in 10mM phosphate buffered saline (PBS, Sigma)), rinsed twice with PBS, and stained with 0.1% crystal violet in 20% ethanol. The plaques were counted and the effective titer of the original stock solution was determined, taking into account all the serial dilutions and the initial amount of virus added to the cell solution. Typically, for these experiments, the density of the cell solution was about 10^6 cells/ml and the virus solution added is small so that the cell solution is not diluted significantly when adding a high multiplicity of virus.

1.2.1.3 Manual single-cell infections

To obtain kinetics of virus production from single-cells, the general infection protocol is followed and then the cell suspension is warmed to initiate an infection. The cell suspension is centrifuged two or three times depending on the amount of virus estimated to remain in solution. Infected cells are separated from this extra virus by centrifuging and re-suspending in fresh media and then the cells are serially diluted and plated at a density of 1 cell/well in a 96-well plate. Wells containing isolated cells are identified and sampled multiple times over the course of the infection by gently removing and replacing the media. The virus contained in these samples is quantified via plaque assay. A diagram of this procedure is shown in Figure 1.2-1.

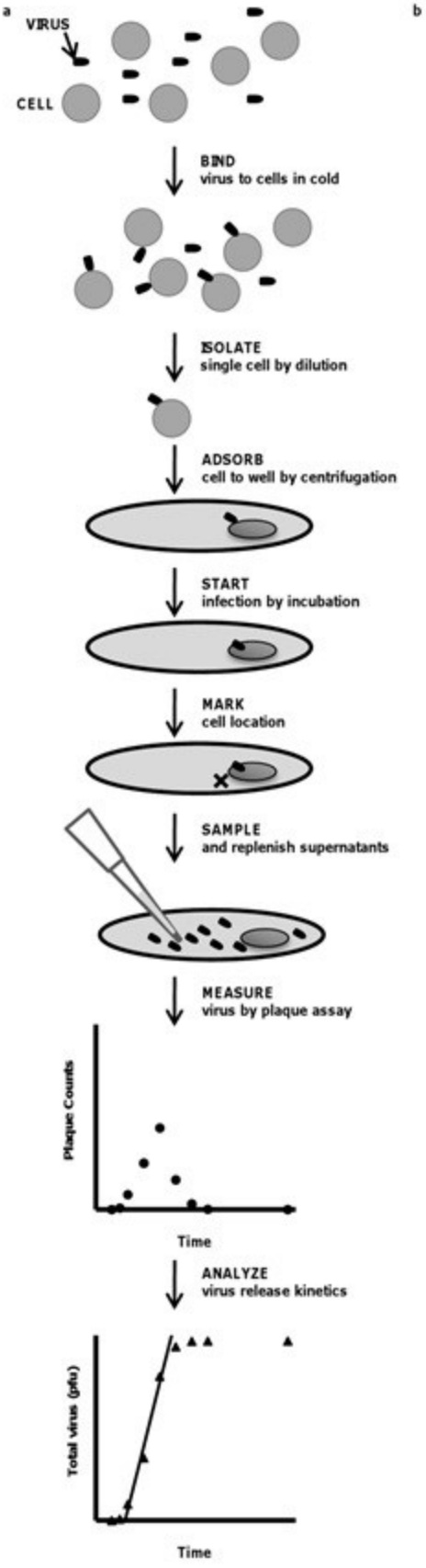
a
VIRUS
CELL
BIND
virus to cells in cold
ISOLATE
single cell by dilution
ADSORB
cell to well by centrifugation
START
infection by incubation
MARK
cell location
SAMPLE
and replenish supernatants
MEASURE
virus by plaque assay
Plaque Counts
Time
ANALYZE
virus release kinetics
Total virus (pfu)
Time

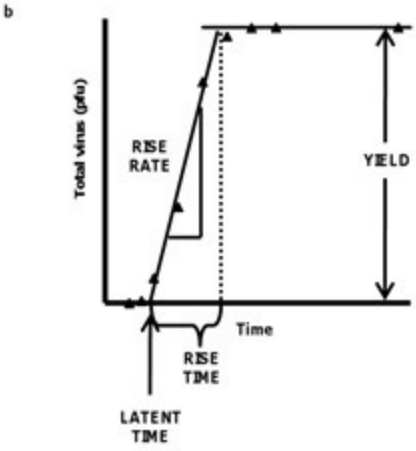
b
Total virus (pfu)
RISE
RATE
YIELD
Time
RISE
TIME
LATENT
TIME

Figure 1.2-1: Workflow for manual single-cell infections and samplings. Cells are synchronously infected in soltion, on ice then serially diluted to ~1 cell/well and plated. The temperature of the culture plate is raised to 37°C to initiate infection. The single-cell wells are identified and sampled by completing removing and replacing the media in the wells several times over the course of the infection. The virus in the samples is quantified via plaque assay and when summed over-time creates a 'one-step' infection curve (Timm 2012).

1.2.2 PDMS device fabrication and specifications

Our microwell devices are molded from a master created by soft-lithography using ~12 g of polydimethylsiloxane (PDMS, Dow-Corning) (Xia 1998). The microwell device is a 2 x 6 array of bull's-eyes and is approximately the same size as a standard glass slide. Each bull's-eye contains ~2500 microwells that are approximately 50μm x 50μm x 50μm with a 50μm space in between the edges of the microwells. The center-port and the moat of the bull'-eyes are recessed (~0.4 mm) to allow for easy liquid manipulations by pipette. This allows multiple, separate experiments on the same device. A diagram of the device is shown in Figure 1.2-2.

For experiments, cells are seeded into the device and then sandwiched between 2 standard glass slides. For most experiments, we apply pressure to keep the device sealed using an aluminum slide holder and clamp (Figure 1.2-3). To use this slide holder, we cut off 2 bull's-eyes to create a 2 x 5 array and center the PDMS device on a glass slide. The clamp, which has 8 holes slightly larger than the bull's-eyes and spaced to cover the first and last four bull's-eyes, applies even pressure on the glass slide sealing the microwells. Running lengthwise down the center of the clamp is a spine approximately 0.7 cm in height. To apply pressure a bar is placed over the spine in the center secured with 2 screws that when tightened apply gradual pressure, evenly over the glass slide by the clamp. The aluminum holder is too reflective for imaging, but this is remedied by coating the surface with black ink. The slide holder is the same size as a

standard Omni Tray and fits into the environmental control stage-top chamber (Pathology Devices) on the fluorescent microscope.

Figure 1.2-2: Diagrams and images of the PDMS microwell device. The center picture is of media droplets being pipetted onto a bull's-eye and on the right is thresholded image of nuclear stains representing cells. The dashed lines represent the boundaries of the microwells.

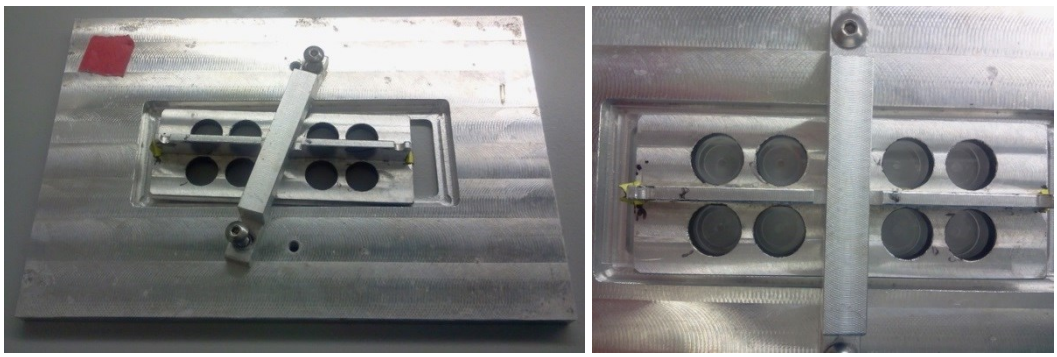

Figure 1.2-3: Images of the aluminum holder for the PDMS device. The devices are sandwiched between 2 glass slides and pressure is applied by screwing down the arm and aluminum clamp. The clamp has 8 holes through which the bull's-eyes are visible.

1.2.3 Quantitative imaging

1.2.3.1 Image processing – background and illumination field corrections

To obtain quantitative measurements of fluorescent reporters in single-cells requires several corrections. First, we collect bright-field and dark-field images to correct for camera noise and variability in the illumination field. Before or after imaging, bright-field (BF) and dark-field (DF) correction images are taken. For each correction image 25 2x2 image arrays are collected under the following conditions: (BF) ~5 ms exposures of a standard fluorescent slide resulting in a signal in the 14 bit range; (DF) exposures the same length as the longest exposure time required by the experiment with the light source turned off. The BF images are of a fluorescent standard that should have the same intensity at every location. By collecting images of this standard we can correct for variance in the illumination field, which we have determined to be approximately 40%. The DF images correct for the inherent noise in the CCD camera. The correction image is obtained by determining the median image of the four images taken at every time-point, and then averaging all the median images together. This is done for both the DF and BF images and the final correction image is created by subtracting the DF from the BF image. The methods for how this correction is applied to the microwell data are discussed in Section 1.2.3.2. The processing of the dark correction images and the illumination field correction images is done in Je'Xperiment (JEX, http://sourceforge.net/projects/jextools/).

1.2.3.2 Image processing – cell identification and collection of measurements

Je'Xperiment (JEX) is an image processing and data-basing software package. Using this program, our time-lapse images are sorted according to array location, color, and time. The image processing steps are described below and the individual programs required to perform these steps are listed in italics. The first step in collecting data from these images is an image

registration (*Image processing -> Register a Multi-color Image Set)*, which is generally done using the phase contrast images. For the most efficient registration, a rectangular region of interest (ROI) is drawn around one empty microwell at each image location. The registration aligns this selected microwell at all time-points and outputs a cropped image set. Second, the locations of all microwells are determined using a convolved image, which identifies the microwells using the red channel (*Single Cell Analysis -> Microwell Convolver*). To obtain this image we multiply the red channel images taken at the first time-point with a convolution kernel that is a white square with a black background. When this kernel is aligned with the center of the microwells, the resulting convolved images have a maxima at each microwell center. The microwells are then identified based on the maxima locations and these locations are constrained by designating the spacing between microwells, with some tolerance, and by designating a minimum number of microwells that should be detected in a given area (*Single Cell Analysis -> Microwell Finder*). The next step is to identify the cell locations, which is done by identifying maxima in the blue channel (*Single Cell Analysis -> Find Maxima in One Color*). Finally, programs in JEX specifically written for the analysis of microwell experiments, count the cells in each microwell at all times, store the locations of these cells, and measure the Hoechst, RFP, and GFP signals within a designated radius of the maxima found in each channel (*Single Cell Analysis -> Microwell Measurements*). The two measurements used for single-cell analysis are the mean intensity surrounding the maxima in each ROI and the mode of the signal in each ROI. The mode is based on the signals collected in a 33 x 33 pixel area centered at each predetermined microwell location. At this time, the maxima in each channel are found separately and so the location of the RFP and GFP measurements are independent of the cell location found in the blue channel. The data is stored in ARFF files, which can be exported (*Table Tools -> Export Table*

Files). The data in these files can then be extracted by Matlab or used more directly in R for analysis. I have used Matlab here, but these files could also be used in the open-source version called Octave.

During data analysis in Matlab or R, several steps are required for background and illumination variation (Figure 1.2-4). First, a local background subtraction is performed for all empty-well and single-cell well data. The single-cell and empty well data is collected and the background signal mode is subtracted from the measurement; recall that for each wavelength a maxima is identified and an area around that maxima is identified, so a cell expressing a signal is not required for a measurement. Next, the median of the average signal from all empty-wells in a given array location, and at all times is determined. We call this the null signal (ϕ). The null signal found for each position in the image array (4x3 array of images covers one bull'-eye) is then subtracted from all the single-cell data at that same array location. Subtraction of the null signal accounts for the background signal of the PDMS device. Finally, we perform the illumination correction using the correction image described in Section 1.2.3.1. When imaging a population of cells in culture, it is possible to make this correction on whole images. However, if we did a whole image correction, the microwell borders would be distorted and create a source of well-to-well variability. Instead, we use the cell location information found using JEX to make this correction in Matlab or R by multiplying the measured signal for each cell by the normalized signal intensity at the same x and y location on the correction image. The final step requires the determination of a limit of detection (LOD), which is based on the corrected empty well measurements. We find the median and standard deviation of the corrected empty well signals at all times and at all locations (entire PDMS device), calculate the median plus 3 standard deviations, and designate the highest value calculated at any location to be the LOD. Any

measurement below the LOD is set to zero. A summary of the corrections and a cartoon of the microwell device is shown in Figure 1.2-4.

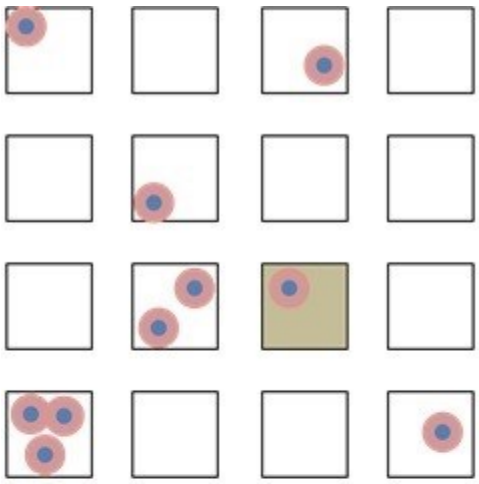

$$\phi = M\left(\mu_{EmptyWells}\right)_{\forall T}$$

$$R_0 = R - \phi_R$$

$$R_F = R_0 - m_R$$

$$\theta_i = \phi_i + 3 \cdot \sigma_i$$

$$\theta = \max\left(\theta_i\right)$$

- M is the median
- R equals the RFP signal from the area around the nucleus, which has a size designated in the JEX measurement function.
- R_0 is the zeroed measurement function (accounts for PDMS background signal)
- R_F is the final background corrected measurement
- m is the mode of the RFP signal from inside the microwell (background signal) – represented by the tan background
- Θ is the detection threshold

- The same sequence of measurements is taken for each fluorescent wavelength

Figure 1.2-4: Background and illumination corrections of single-cell microwell data. Blue represents the nuclear stain and the pink surrounding the blue is the RFP signal emanating from the cytoplasm. The blue nuclear stain is used to identify the cell count in each well.

1.3 References

1. **Allen, L. Z., T. Ishoey, M. a Novotny, J. S. McLean, R. S. Lasken, and S. J. Williamson**. 2011. Single virus genomics: a new tool for virus discovery. PloS one 6:e17722.

2. **Blair, W. S., J. Isaacson, X. Li, J. Cao, Q. Peng, G. F. Z. Kong, and A. K. Patick**. 2005. A novel HIV-1 antiviral high throughput screening approach for the discovery of HIV-1 inhibitors. Antiviral Research 65:107–116.

3. **Burnet, F.** 1929. A method for the study of bacteriophage multiplication in broth. British journal of experimental pathology X:109–115.

4. **Chen, C. S., M. Mrksich, S. Huang, G. M. Whitesides, and D. E. Ingber**. 1997. Geometric control of cell life and death. Science 276:1425–1428.

5. **Choi, J., and K. R. Love**. 2011. Immuno-hybridization chain reaction for enhancing detection of individual cytokine-secreting human peripheral mononuclear cells. Analytical … 83:6890–6895.

6. **Davidson, I., and R. F. Silva**. 2008. Creation of diversity in the animal virus world by inter-species and intra-species recombinations: lessons learned from poultry viruses. Virus genes 36:1–9.

7. **De Paepe, M., S. De Monte, L. Robert, A. B. Lindner, and F. Taddei**. 2010. Emergence of Variability in Isogenic Escherichia coli Populations Infected by a Filamentous Virus. (A. Yates, ed.)PLoS ONE 5:9.

8. **Delbruck, M.** 1945. The burst size distribution in the growth of bacterial viruses (bacteriophages). Journal of bacteriology 50:131–5.

9. **Domingo, E., and E. Martínez-Salas**. 1985. The quasispecies (extremely heterogeneous) nature of viral RNA genome populations: biological relevance—a review. Gene 40:1–8.

10. **Ecker, R. C., and G. E. Steiner**. 2004. Microscopy-based multicolor tissue cytometry at the single-cell level. Cytometry Part A the journal of the International Society for Analytical Cytology 59:182–190.

11. **García-Arenal, F.** 2001. Variability and genetic structure of plant virus populations. Annual Review of Phytopathology 39:157–186.

12. **Hayden, F.** 2009. Developing new antiviral agents for influenza treatment: what does the future hold? Clinical Infectious Diseases 48 Suppl 1:S3–S13.

13. **Lang, A. S., M. L. Rise, A. I. Culley, and G. F. Steward**. 2009. RNA viruses in the sea. FEMS microbiology reviews 33:295–323.

14. **Lindström, S., R. Larsson, and H. A. Svahn**. 2008. Towards high-throughput single cell/clone cultivation and analysis. Electrophoresis 29:1219–1227.

15. **Liu, S.-Y., D. J. Sanchez, R. Aliyari, S. Lu, and G. Cheng**. 2012. Systematic identification of type I and type II interferon-induced antiviral factors. Proceedings of the National Academy of Sciences of the United States of America 109:4239–4244.

16. **Luker, K. E., M. Hutchens, T. Schultz, A. Pekosz, and G. D. Luker**. 2005. Bioluminescence imaging of vaccinia virus: effects of interferon on viral replication and spread. Virology 341:73–81.

17. **Lwoff, a, R. Dulbecco, M. Vogt, and M. Lwoff**. 1955. Kinetics of the release of poliomyelitis virus from single cells. Virology 1:801–805.

18. **Marschall, M., M. Freitag, S. Weiler, G. Sorg, and T. Stamminger**. 2000. Recombinant Green Fluorescent Protein-Expressing Human Cytomegalovirus as a Tool for Screening Antiviral Agents. Antimicrobial Agents and Chemotherapy 44:1588–1597.

19. **Martínez-Sobrido, L., R. Cadagan, J. Steel, C. F. Basler, P. Palese, T. M. Moran, and A. García-Sastre**. 2010. Hemagglutinin-pseudotyped green fluorescent protein-expressing influenza viruses for the detection of influenza virus neutralizing antibodies. Journal of Virology 84:2157–2163.

20. **Miller, D. K., and J. Lenard**. 1980. Inhibition of vesicular stomatitis virus infection by spike glycoprotein. Evidence for an intracellular, G protein-requiring step. The Journal of Cell Biology 84:430–437.

21. **Ozawa, T., K. Kinoshita, S. Kadowaki, K. Tajiri, S. Kondo, R. Honda, M. Ikemoto, et al.** 2009. MAC-CCD system: a novel lymphocyte microwell-array chip system equipped with CCD scanner to generate human monoclonal antibodies against influenza virus. Lab on a chip 9:158–163.

22. **Panchal, R., K. Kota, K. Spurgers, and G**. 2010. Development of High-Content Imaging Assays for Lethal Viral Pathogens. Journal of Biomolecular Screening 15:650–651.

23. **Raaben, M., H.-J. Prins, A. C. Martens, P. J. M. Rottier, and C. a M. De Haan**. 2009. Non-invasive imaging of mouse hepatitis coronavirus infection reveals determinants of viral replication and spread in vivo. Cellular Microbiology 11:825–841.

24. **Shaneyfelt, M. E., A. D. Burke, J. W. Graff, M. a Jutila, and M. E. Hardy**. 2006. Natural products that reduce rotavirus infectivity identified by a cell-based moderate-throughput screening assay. Virology Journal 3:68.

25. **Simonsen, L., C. Viboud, B. T. Grenfell, J. Dushoff, L. Jennings, M. Smit, C. Macken, et al.** 2007. The genesis and spread of reassortment human influenza A/H3N2 viruses conferring adamantane resistance. Molecular Biology and Evolution 24:1811–1820.

26. **Snijder, B., R. Sacher, P. Rämö, E.-M. Damm, P. Liberali, and L. Pelkmans**. 2009. Population context determines cell-to-cell variability in endocytosis and virus infection. Nature 461:520–3.

27. **Timm, A., and J. Yin**. 2012. Kinetics of virus production from single cells. Virology 424:11–7.

28. **Tokimitsu, Y., H. Kishi, S. Kondo, R. Honda, K. Tajiri, K. Motoki, T. Ozawa, et al.** 2007. Single lymphocyte analysis with a microwell array chip. Cytometry. Part A : the journal of the International Society for Analytical Cytology 71:1003–10.

29. **Torres, A. J., R. L. Contento, S. Gordo, K. W. Wucherpfennig, and J. C. Love**. 2013. Functional single-cell analysis of T-cell activation by supported lipid bilayer-tethered ligands on arrays of nanowells. Lab on a chip 13:90–9.

30. **Towner, J. S., J. Paragas, J. E. Dover, M. Gupta, C. S. Goldsmith, J. W. Huggins, and S. T. Nichol**. 2005. Generation of eGFP expressing recombinant Zaire ebolavirus for analysis of early pathogenesis events and high-throughput antiviral drug screening. Virology 332:20–27.

31. **Warrick, J., A. Timm, A. Swick, and J. Yin**. n.d. A massively-parallel, pipette-based platform for single-cell kinetic studies of virus-host interactions. PloS ONE in prep.

32. **Xia, Y., and G. M. Whitesides**. 1998. Soft Lithography. Annual Review of Materials Science 28:153–184.

33. **Zhu, Y., A. Yongky, and J. Yin**. 2009. Growth of an RNA virus in single cells reveals a broad fitness distribution. Virology 385:39–46.

34. **Zuck, P., E. M. Murray, E. Stec, J. a Grobler, A. J. Simon, B. Strulovici, J. Inglese, et al.** 2004. A cell-based beta-lactamase reporter gene assay for the identification of inhibitors of hepatitis C virus replication. Analytical Biochemistry 334:344–355.

Chapter 2: A high-throughput platform for quantitative analysis of single-cell infections

2.1 Introduction

In the battle between a virus and its host cell, early events often dictate the eventual winner (Flint., 2009). Over time, host cells have evolved many mechanisms to protect themselves from challenge by viral or bacterial attack. For example, pattern recognition receptors identify 'foreign' materials such as dsRNA, which once identified, initiate signaling cascades leading to protective cytokine production. These innate defense mechanisms are countered by viruses, which have also evolved numerous ways to evade or shut down host defenses. For example, the virus studied in this work, vesicular stomatitis virus (VSV), uses its matrix protein to block export of cellular mRNA from the nucleus, shutting down the cell's ability to mount an immune response. These early processes often begin with low copy numbers (e.g. a few viral genomes or toll-like receptors), which need to be amplified in some manner to affect the outcomes of infections. The dynamics of this amplification can be variable and can be thought of as stochastic in nature (Elowitz 2002; Levin 2011; Rand 2012; Zhao 2012). Stochasticity in gene expression is one source of variability, but there are many other causes of the phenotypic variability seen in clonal cell populations such as cell-cell signaling and contact which can affect a variety of things such as cell size and the cellular replication cycle. This type of variability has been shown to affect the ability of a virus to infect a cell (Oliere 2008; Snijder 2009; Zhu 2009; He 2010) and also affect cellular gene expression (Volfson 2006). Standard cell culture assays mask this variability, which can have huge implications on how a virus is able to replicate and spread. For example, by quantifying virus production from individual cells our group and others have shown that there is actually a great deal of variability in per-cell virus yields (Delbruck 1945; Lwoff

1955; Zhu 2009; Timm 2012). In order to better understand the effects of stochasticity and other phenotypic variability in these virus-host systems, we have developed tools to study the dynamics of single-cells infections.

Here, we introduce a high-throughput single-cell infection assay platform to study virus-host interactions using the model RNA virus, vesicular stomatitis virus (VSV), and the immortalized prostate cancer cell line, PC3. VSV is known for its broad cellular tropism, exceptionally fast replication kinetics in permissive cell types, and its extreme sensitivity to interferon stimulated genes (Fensterl 2012; Müller 2013). PC3 cells have a robust innate immune response to infection by VSV, largely due to the fact that these cells have an intact interferon pathway. This property of PC3 cells is unlike many other immortalized cancer cell lines, and makes these cells a very useful tool in the study of the innate immune response to viral infections. The extent of PC3 resistance to infection by VSV has been characterized (Carey 2008). For both the virus and the host, we utilize previously developed fluorescent reporter strains. Fluorescent protein genes can be incorporated into viruses or cell lines in order to report on the state of virus infection or the expression of certain cellular genes. These reporters can be valuable tools to study the dynamics of virus-host interactions *in situ,* especially when combined with microfluidics. The high-throughput single-cell infection assay platform that we have developed allows us to study the variability inherent in virus-host systems. We are able to study hundreds of isolated single-cells in a uniform cell culture environment, and in the absence of cell-cell signaling. We demonstrate here that the biology reflected by the dual-color reporter system is in agreement with what has been described in the literature and that we have developed a tool capable of providing new biological insights.

2.2 Materials and Methods

2.2.1 Cell and virus culture

BHK (baby hamster kidney), PC3 (prostate cancer) and PC3-IFIT2-ZsGreen1-DR (PC3-IFIT2) reporter cells were used in this work. The generation of the PC3-IFIT2 reporter cell line was described in Swick et al. (Swick n.d.). Briefly, a ZsGreen1-DR gene controlled by an IFIT2 promoter was stably transduced into PC3 cells. Activation of innate immune pathways that leads to production of the interferon stimulated gene, IFIT2, in PC3 reporter cells, also leads to the production of the ZSGreen protein.

BHK cells were passaged every 2-3 days and grown in MEM (Cellgro) supplemented with 10% FBS (Atlanta Biologicals) and 2mM GlutaMAX (Gibco) and the PC3 and PC3-IFIT2 cells were passaged every 3-4 days and grown in RPMI 1640 (Gibco) supplemented with 10% FBS. Infections of the cells lines were done in the same media, but with the FBS content reduced to 2%. The viruses used in this study were recombinant strains of VSV encoding the gene for DSRed-Express protein in the fifth position of the genome, after the glycoprotein gene and before the polymerase gene. By placing the reporter gene in this position, attenuation caused by adding an additional gene is limited, but virus replication still results in a strong fluorescent signal (Swick n.d.). Both a wild-type (N1-DSRedEx) and mutant form (M51R-DSRedEx) were used and both stocked on BHK cells. The M51R strain has a methionine to arginine point mutation in the matrix protein. This mutation prevents the matrix protein from functioning properly in its role to block nuclear export (Ahmed 1997).

2.2.2 Population one-step infection assay

One day before infection, PC3 cells were plated in 12-well plates at a density of 1.8 x 10^5 cells/well. PC3 cells are highly resistant to infection by VSV, so to achieve a synchronous infection 200µl of stock virus (N1-DSRed) was added directly to cell monolayers and allowed to adsorb for one-hour in an incubator, rocking plates every 20 minutes. The virus was titered on PC3 cell monolayers, and based on this number the effective MOI, was approximately 15 (~3500 MOI on permissive BHK cells). After adsorption, the stock solution was removed and the cells were rinsed with sterile PBS and overlaid with 1 ml PC3 infection media. Two other 12 well plates were used for infected and un-infected monolayer controls. At various time-points, these plates were imaged with a Typhoon FLA 9000 (GE) and then one-well at each time-point was sacrificed to sample for virus production. The infected and un-infected controls were used to normalize the RFP fluorescent signal from the Typhoon scanner. Images and samples were taken at the times designated in the figures. The host GFP signal could not be resolved using the Typhoon scanner due to a very high background signal.

2.2.3 Typhoon image analysis

Analysis of the typhoon image data was done with ImageJ. An ellipse was drawn covering the majority of each well of a 12-well plate. Signals from un-infected control cells were subtracted from the average of all un-sampled control wells. At different sampling times, the background signals changed. To normalize the measurements taken at different times, the signal at each time point was divided by the ratio of the background signal at that time point and the maximum background signal. The signals were also normalized according to position. There was a very regular gradient in the signal from the top left well, to the bottom right well that was observed in

the uninfected control plate. This gradient was likely due to uneven illumination of the cell-culture plates.

2.2.4 Nuclear labeling and VSV infections for microwell experiments

PC-3 IFIT2 reporter cells were infected in solution with either the M51R-DSRed or the N1-DSRed virus strains at stock virus concentrations. However, due partially to the inefficiency of cold adsorption on PC3 cells, viral infection was detected in only 1/3 of cells. The methods for performing the in solution infections have been previously described (Timm 2012, Chapter 1). Following the virus adsorption period, the temperatures of the virus-cell solutions were raised to 37°C in a water bath for 7 minutes to allow for internalization of the attached virus. To remove any excess virus, the cell solutions were centrifuged (1000 rpm, 4 min), the infection media decanted, and the infected cell pellet re-suspended in fresh media three times. With the final re-suspension, the cell density was adjusted to the optimal density for microwell seeding (1-2 x 10^5 cells/ml). The re-suspension infection media contained Hoechst 33342 (AnaSpec, 1μM) and HEPES (Sigma-Aldrich, 25mM). Hoechst 33342 is a live-cell nucleic acid stain that can be used to identify the location and number of cells in microwells. HEPES is a buffer commonly used in microfluidics applications to protect cells in systems with sub-optimal gas exchange.

2.2.5 Bull's-eye device seeding and assembly

2.2.5.1 Device preparation

Approximately 1 hour before beginning the infection procedure, the PDMS device was placed under a UV lamp for sterilization. (A description of the dimensions of the Bull's-eye device is described in Section 1.2.2. Also included in Section 1.2.2 are the methods used to make the devices). After 20-30 minutes, the device was moved to a vacuum chamber for de-gassing. This

step is critical, as it allows liquid to readily fill the wells instead of trapping air underneath the liquid layer. After 20 minutes in the vacuum chamber, 100µl droplets of infection media (containing HEPES and Hoechst) were placed on each bull's-eye to wet the device. There is sufficient surface tension to keep droplets from spilling into the moats. It is necessary to ensure that all wells are covered with fluid, as empty wells will speed up drying later in the infection. The PDMS device was placed in an incubator, with the droplets in place before beginning the infection procedure. The device was in this humid environment for approximately 1 hour before cell seeding began.

2.2.5.2 Cell seeding

To seed the infected cells into the microwell device, the existing droplets were removed and replaced with 70-80µl droplets of the infected cell solution (1-2 x 10^5 cells/ml). After 30-60 seconds, the droplets were removed swiftly by placing the pipette tip in the recessed center and replaced quickly, but gently with fresh media. The swift removal of the droplets sweeps cells off the top surface of the device, but does not disturb the cells that have settled into microwells. It is necessary to keep the pipette vertical and not pipette from an angle. The bull's-eyes were washed with fresh media twice more in the same manner. It is important not to overload the wells with cells, as they are difficult to wash away once seeded and overloading will cause cells to become trapped outside the wells and crushed during sealing. The nuclear stain of these cells will still be visible and will interfere with image analysis.

2.2.5.3 Device sealing

The device was sealed by quickly removing the droplets from all bull's-eyes and gently covering with a glass slide (top side treated with 0.1% Tween 20). It is important not to add and then release pressure to the microwells as this causes bubbles to form and displaces cells. The

Tween is applied by pipetting on ~ 1 ml of 0.1% Tween, then before sealing, removing all but a thin layer of the solution. Tween 20 (Fisher Scientific) is a surfactant that prevents condensation droplets from forming on the top side of the sandwich device when inside the humid microscope chamber – instead, an even layer of liquid forms. The liquid layer does not affect fluorescent imaging, and an even liquid layer instead of droplets allows for better topside phase contrast images. Pressure is applied to maintain the sealing as described in Section 1.2.2. Pressure was applied to enable complete sealing of the microwells, but without permitting glass slides to break.

In this experiment, two bull's-eyes were seeded with un-infected cells to determine cell viability after 24 hours of imaging, three bull's-eyes were seeded with M51R-infected cells, and three bull's-eyes were seeded with N1-infected cells. The viability measurements were inconclusive, but the method appears to keep cells relatively healthy because we observe viral protein production long into imaging.

2.2.6 Time-lapse imaging

As described in Section 1.2.3.1, correction images were taken before beginning the time-lapse to correct for uneven light intensity. The exposure time for the illumination correction images was 5ms and the exposure time for the dark field correction images was 1500ms (or the longest exposure time used).

The aluminum device holder containing the bull's-eye device and several DPBS soaked Kimwipes (Kimberley Clark) was placed on the automated microscope stage, using an Omni Trey bottom for a lid. The DPBS soaked Kimwipes help provide a humid environment for the PDMS device. Fluorescent time-lapse imaging was done on a Nikon Eclipse TE300 microscope,

using an EXI Aqua camera (Q Imaging). The environmental conditions were controlled by an outer warming chamber encompassing the microscope and a stage-top incubator chamber (Pathology Devices) set to 37°C, 5% CO_2, and approximately 85% RH. Once the system had equilibrated to the correct temperature, the center locations of the bull's-eyes were identified and memorized and the stage was focused to the Hoechst 33342 stained nuclei. Images were taken in a 4 x 3 array around the center of each bull's-eye in the following order: bright-field (5ms exposure), blue channel (20ms exposure), red channel (1500ms exposure) and green channel (1500ms exposure) using a Sedat quad cube. Imaging the entire array required approximately 18 minutes, and was looped at a 30 minute interval for 22 hours beginning 1.42 hpi.

2.2.7 Image processing workflow and data analysis

Image organization and processing was done in JEX as described in Section 1.2.3.2. Briefly, the images were sorted according to location, time, and color and then registered to correct for any small shifts in the device location. For this work, registration was done based on the phase contrast images. Following registration, a convolution image was created using the first red channel image (taken before any detectable signal from cells) and a convolution kernel. Microwell locations were located and numbered based on the convolution image. The maxima in the blue channel (# of nuclei) were located and the number in each microwell determined. Finally, a cell radius was chosen and measurements were taken in each fluorescent color at all times (method for determining correct radius are included in Section 2.2.7.1). The measurement and cell count data tables are exported and analyzed in Matlab.

2.2.7.1 Cell radius determination

The microwell measurements function in JEX works by searching each ROI (microwell) for a maximum signal and then drawing a circle with a designated pixel radius around that maximum

and measuring the average intensity of that area. In general, I use a radius of 13 for PC3 cells and 9 for BHK cells; however, the right radius might change based on experimental conditions. The radius should be large enough to encompass each cell accounting for variability in cell size, but not so large that cells in neighboring wells are detected in the analysis. The smallest size that surrounds the cells should be chosen for added sensitivity. I choose a size by taking measurements with a range of different designated radii and creating parity plots from the measurements. An example is shown in Figure 2.2-1

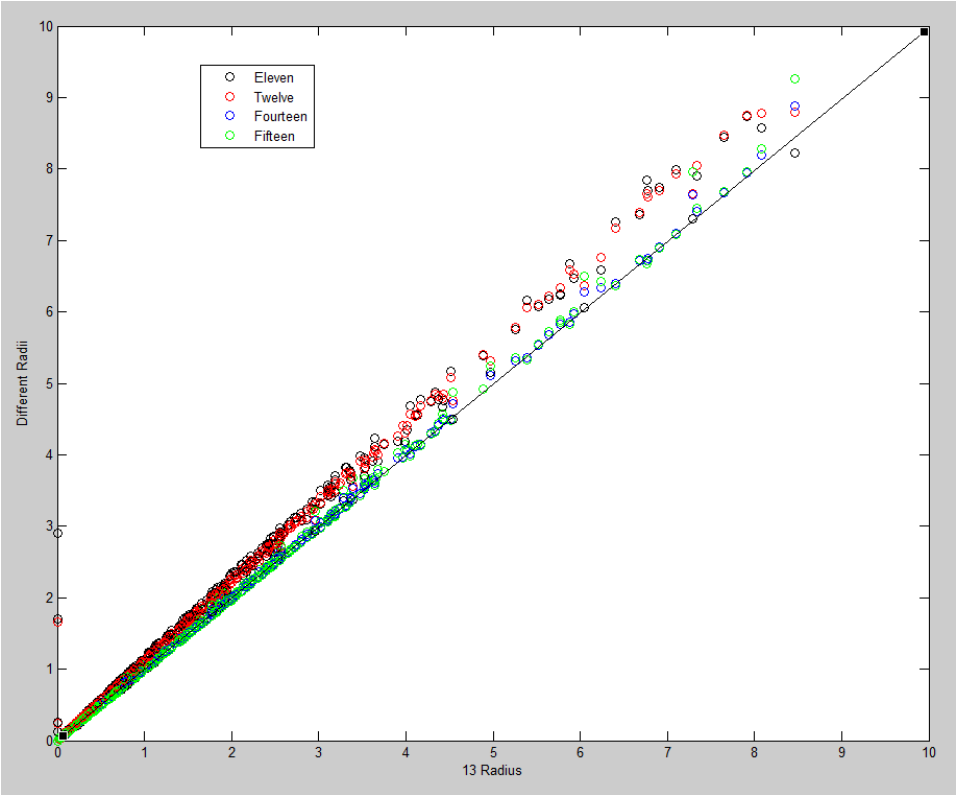

Figure 2.2-1: Parity plots of various cell radii compared to a radius of 13.

2.2.7.2 Matlab analysis

The code used to analyze the microwell data can be found on the Yin lab's shared server in Past Group Members\Andrea\MatlabCode\Chapter2. In order to perform the analysis in Matlab, the ARFF files exported by JEX must be converted into a format readable by Matlab. This is done with the Matlab Weka Interface. The file names of various scripts necessary for each step are written in italics.

Step 1: Extract cell counts and cell location information

Run *CellCountDriver.m* → requires *CellCountFunction, loadARFF, weka2matlab, convertIndex,* and *wekaPathCheck* scripts

Step 2: Extract measurements

Run *MeasuresDriver.m* → requires *MeasuresFunction, loadARFF, weka2matlab, covertIndex,* and *wekaPathCheck* scripts

Wells that contained zero or one cell were identified and the measurements corresponding to those wells collected and organized according to image location for easier analysis. After this data extraction step, the data must be cleaned. Cleaning of the data entails sorting through the images taken at each color and excluding microwell locations that contained fluorescent debris, bubbles, or other factors that might result in an incorrect measurement. A log of the errors is created, and those microwells are excluded from Matlab data tables.

Step 3: Create error log

Fill in *ErrorLogCreator.m* script file with the microwell numbers that must be eliminated from analysis. Run *ErrorLogCreator*, then run *ClearListsDriver* → requires *CleanROILists*

The empty wells were used to determine the signal from the PDMS (Ø signal) and the measurement threshold. The mode from the single-cell wells was subtracted from the cell signal at each time point. The mode is essentially the background signal at each well location. Finally, the measurement error was determined and found to be negligible until values drop below approximately 10 au (CV ~ 10%), near the limit of detection (details found in Section 2.2.7.4).

Step 4: Run *AnalysisDriver.m*

→ loads time information, loads cleaned ROI lists, loads measurements, loads cleaned cell locations, loads illumination correction image and runs *measureBackground, measureThreshold, illuminationCorrection, and thresholdData*.

At this point the cleaned, thresholded data is complete and is saved for more specific analysis. It is necessary at this point to check the maximum threshold used on all the data. Occasionally, a cell will not retain the nuclear stain and a well designated as empty will have a positive reporter signal. A positive signal in an 'empty' well will artificially raise the limit of detection. The individual thresholds for each image location should be checked for similarity. If one or more of the individual thresholds are too high, we identify the problem microwell, add that microwell number to the *ErrorLogCreator* and run through Steps 3 and 4 again.

Step 5: For the reporter cell data collected in this work, specific functions were created to identify and collect data from cells that were RFP+GFP+, RFP+GFP-, or RFP-GFP+,

plot reporter trajectories for these single-cell populations, and extract the desired kinetic parameters.

→ *RFP_GFPData* and *Delay_RFPDeath* → requires *fit_expo_fun, find_RSquared, expo_objfun, expofun* (fitting functions written primarily by Ankur Gupta)

2.2.7.3 Data fitting

To obtain a rate approximation we have fit the following exponential equation to the first four positive data points:

Equation 2.2-1

$$Intensity = A \cdot \exp(\alpha \cdot time)$$

The first four time-points can vary greatly in intensity. In order to fit the data correctly, we must account for the changing noise levels spanning different magnitudes of intensity. The majority of the noise is Poisson distributed and is a function of the number of photons detected (Waters 2009). The maximum variance is equivalent to the square root of the total number of detected photons, which is determined using the following equation:

Equation 2.2-2

$$photons = \left(\frac{f}{i_{\max} - o}\right) \cdot (i - o) \qquad \text{(Waters 2009)}$$

where f is the full well capacity of the camera, i_{max} is the maximum intensity value possible based on the detector, i is the measured intensity, and o is the detector offset. According to QImaging, the specifications of our 14-bit CCD camera are f = 18,000 electrons and i_{max} = 16,384 au. The offset term is eliminated during our image processing steps by subtracting the dark-field images,

which correct for camera noise. Finally, we assume the quantum efficiency, or number of photons required to release one electron, is 0.6 electron/photon. The measurements we collect are the average intensity over a circle area encompassing the cells, so we must also adjust for that number of pixels. Our equation for variance is now:

Equation 2.2-3

$$\sigma = \sqrt{\frac{f}{QE \cdot i_{\max}} \cdot i} = \sqrt{\frac{f}{QE \cdot i_{\max}} \cdot \frac{signal}{\pi \cdot r^2}} = \sqrt{\frac{18{,}000}{0.6 \cdot 16{,}384} \cdot \frac{signal}{\pi \cdot 13^2}} = 0.059 \sqrt{signal}$$

and we weight each data point using the factor of $1/\sigma^2$ and use a non-linear least squares fitting algorithm in Matlab to fit the exponential curve to each individual RFP and GFP trajectory.

2.2.7.4 Determination of measurement error

BHK cells were co-infected with two strains of VSV, one encoding a red fluorescent protein and another encoding a green fluorescent protein. A 4 row by 3 column image array was taken of infected BHK cells late in infection so that most cells were expressing both RFP and GFP. The images in the array had large overlapping sections so that the same microwells were imaged up to 4 times. An example of overlapping regions is shown in Figure 2.2-2 below. Using 5 regions of 4 overlapping images per region, we collected 4 replicate measurements of many isolated cells. Using this data we were able to approximate the error in reporter expression measurements over a range of intensities for both the viral (RFP) and viral (GFP) reporters. The error profiles are shown in Figure 2.2-3, where we plot the log10 of the coefficient of variation against the log10 of intensities.

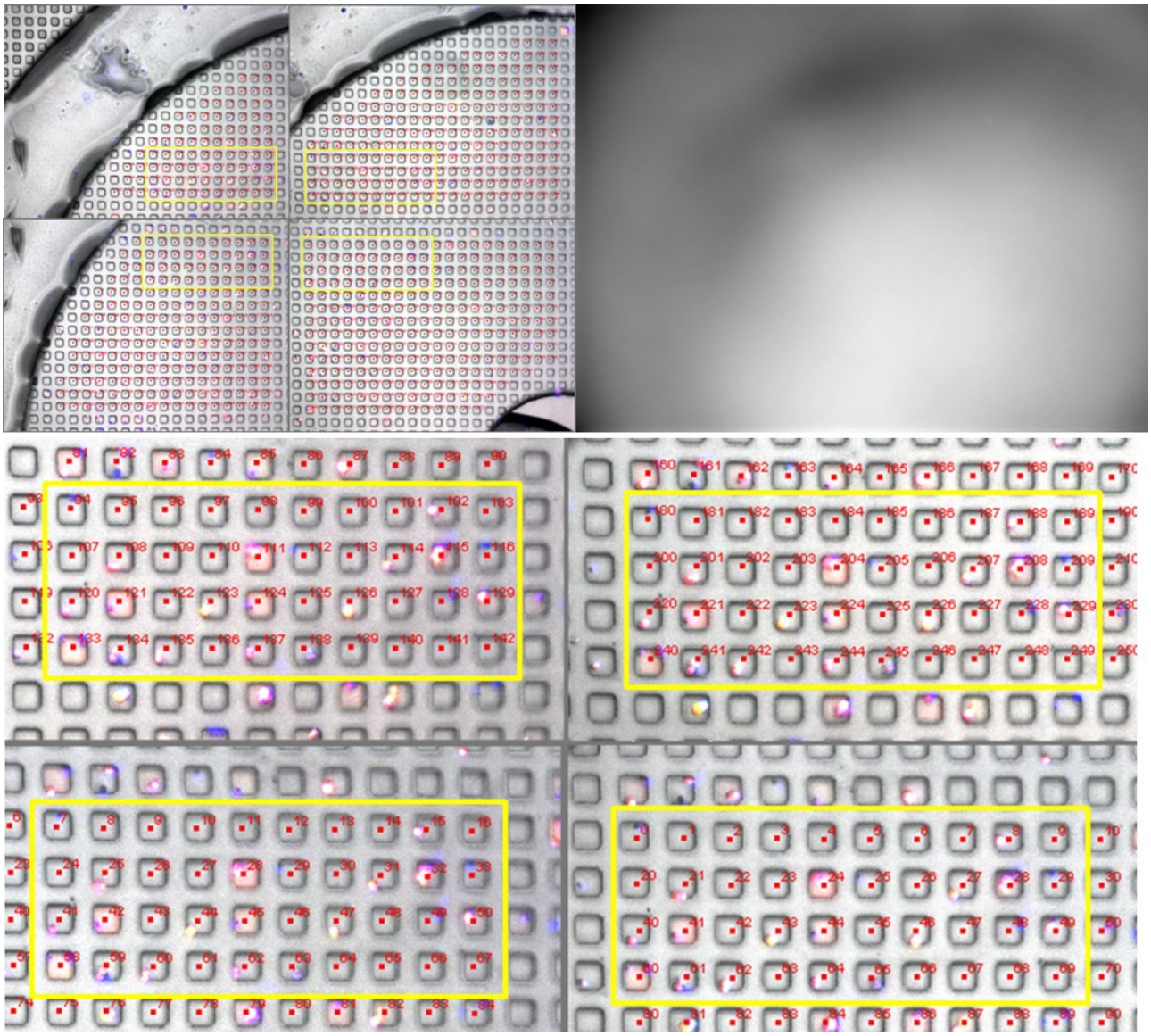

Figure 2.2-2: (top left) Four images from a 4x3 image array with large overlapping regions. These overlapping areas correspond to different areas of light exposure (top right). (bottom) Magnified image of the overlapping array showing the microwells common to the four images.

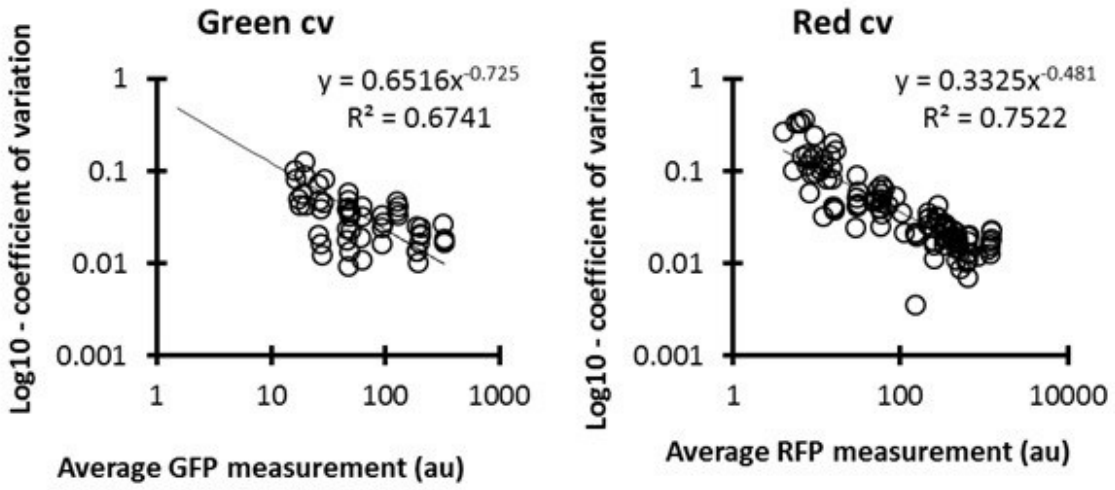

Figure 2.2-3: (left) Error profile for the GFP data (right) Error profile for the RFP data

2.3 Results

Microwells provide identical environments for each cell, creating a significantly more uniform context in which to quantify cell behavior compared to standard population level experiments. Isolation of each target cell enables very clean and robust data collection at multiple wavelengths and with no need for cell tracking or discrimination between the fluorescent signals of adjacent cells. The data collected is much like flow cytometry data, but with two primary advantages: first, the infected cells are sealed in the device throughout imaging, eliminating the risk associated with running infectious materials through a flow cytometer; and second, kinetic single-cell microscopy data can be collected with ease, while obtaining such data with a flow-cytometer would require multiple parallel experiments. Using the VSV-PC3 cell reporter system, we will demonstrate the advantages of this type of data and the novel results one can acquire using single-cell techniques.

2.3.1 Very high MOI necessary to synchronize infections in resistant PC3 cells

PC3 cells, a prostate cancer cell line known to be resistant to VSV infections (Carey 2008), were infected with N1-DSRed at two MOIs. The lower MOI corresponds to an MOI of 50 on VSV permissive cells and the higher MOI corresponds to an MOI of over 3000 on these same permissive cells. If we titer this virus on PC3 cells, the effective MOIs are approximately 0.2 PFU/cell and 15 PFU/cell. These titers are based on plaque growth on cell monolayers. The low efficiency of plaque formation is likely due to a combination of effects, including the immune response of the cells, which might slow virus spread enough to prevent macroscopic plaque formation, and non-replicating viruses trapped in cells. VSV particles internalized by PC3 cells often become trapped in endosomes and fail to initiate replication processes (Carey 2008).

N1-DSRed replication kinetics after infection at the high MOI were similar to the kinetics of this same virus on permissive BHK cells; however, when PC3 cells were infected at a much lower MOI, virus production was significantly delayed, likely because replication was occurring in more than 1 round of replication (Figure 2.3-1). While virus production occurred more slowly at the lower MOI, this cell population eventually produced about the same overall yield as the population infected at the higher MOI. For all subsequent experiments, we will use the higher MOI in an attempt to synchronize the virus infection in all cells. Virus yields of the high MOI infection of PC3 cells appear to produce infectious virus at the first time-point; however, this is like virus that was not washed away after adsorption. It is our convention to plot this amount of virus so that we can observe the change in production between the first two time-points.

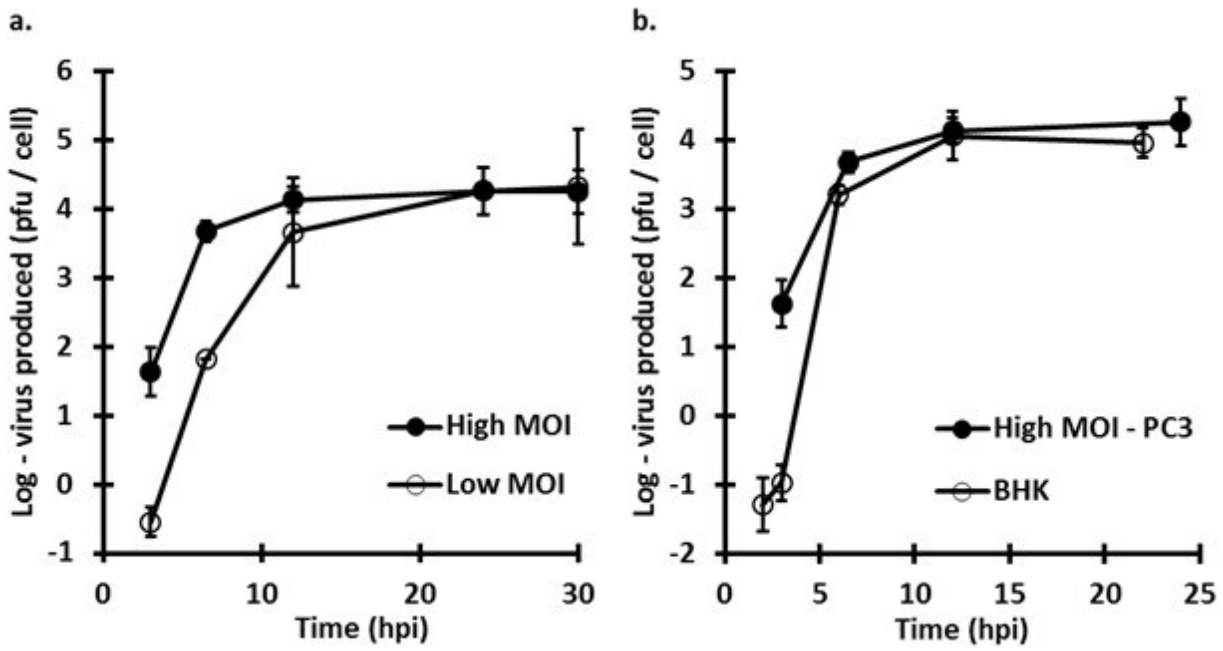

Figure 2.3-1: Synchronized VSV infections of resistant PC3 cells have yields similar to VSV infections of the permissive BHK cells. (a)High (~3500) and low (50) MOI infections on PC3 cells. (b)Synchronized VSV infections on PC3 (MOI ~ 3500) and BHK cells (MOI 10).

2.3.2 Viral reporter protein kinetics and yields are a reasonable indicator of virus production kinetics and yields

Fluorescent reporter proteins can be used for real-time readouts of what is happening in a biological system. The viruses used in these experiments all encode the gene for DSRed-Express in the fifth position of the VSV genome. As intracellular virus replication proceeds, the reporter gene is transcribed and translated into protein along with the other viral genes. VSV transcription is initiated from a single-promoter and at each intergenic junction the polymerase can continue and transcribe the next gene, or fall off causing an attenuation in gene expression that increases from the nucleoprotein gene to the polymerase gene (Barr 1997; Lyles 2007). This is the method by which VSV regulates its protein production. The rate of mRNA production has been shown to

be linearly related to number of genomes (Timm 2013). Based on these two pieces of information, our hypothesis is that fluorescent reporter protein production will generally be proportional to genome production and viral yields.

To determine if virus production and reporter expression were related, we performed population one-step infections and simultaneously measured the viral RFP expression. If we compare viral production kinetics and reporter protein kinetics, we find that they are correlated and can be used as a reasonable indicator of virus production. Figure 2.3-2 shows how well the RFP signal from infected cells correlates with virus production kinetics at a population level. In Figure 2.3-2a, the delay-time in RFP production between the high and low multiplicity infections is similar to the delay between initial virus production in these experiments. In the case of the PC3-IFIT2 cells infected with N1-DSRed or M51R-DSRed, the RFP production kinetics are very similar to each other and to the virus production kinetics. Throughout the infection process the relative kinetics (infection delay, rise-time, and yield) of virus production and RFP production were conserved.

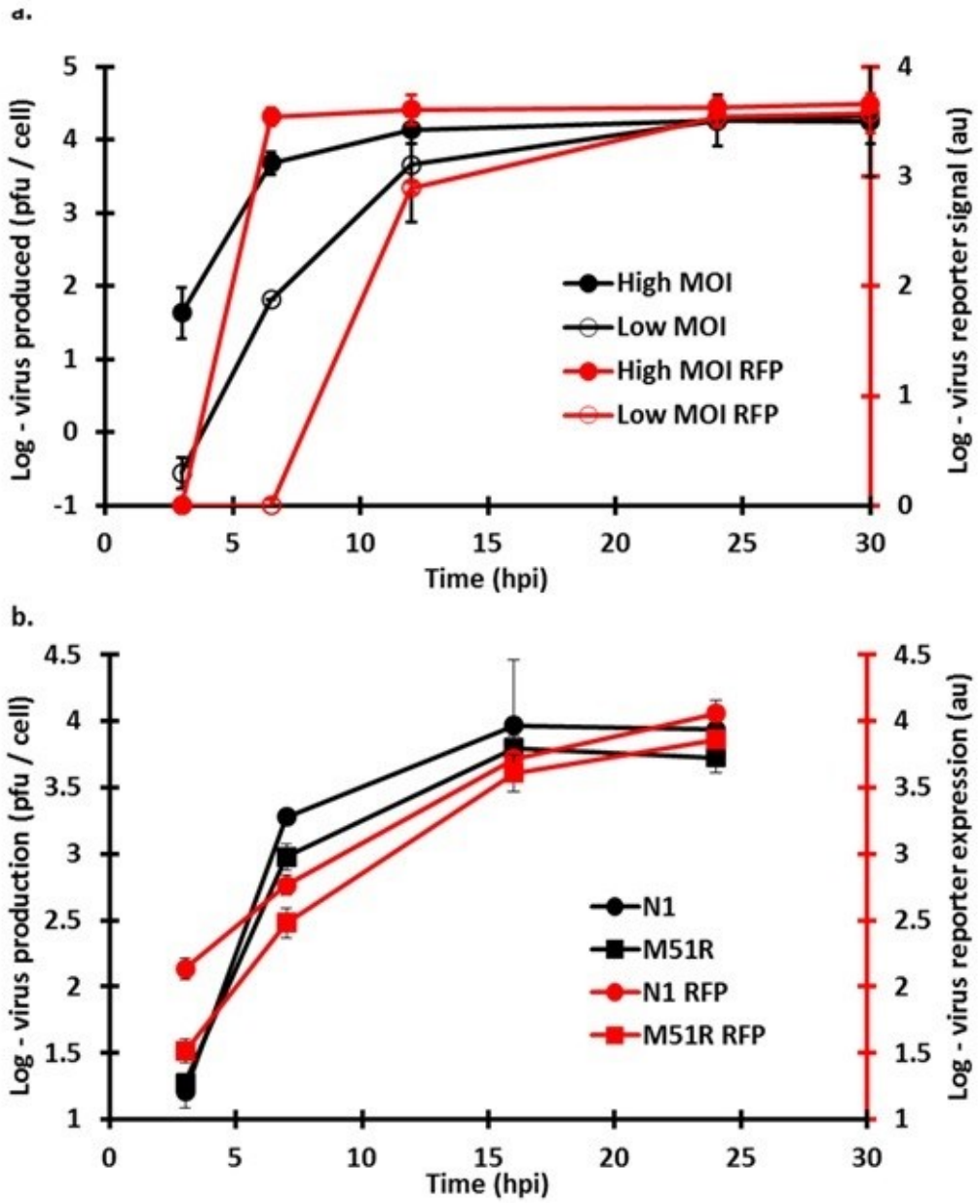

Figure 2.3-2: Viral RFP reporter is reasonable indicator of virus replication kinetics and yields. (a)High and low MOI N1-DSRed infections of PC3 cells, virus production (black) and fluorescent protein kinetics (red). (b)High MOI N1-DSRed and M51R-DSRed infections of PC3 cells, virus production (black) and fluorescent protein kinetics (red).

2.3.3 Proportions of infected and IFIT2 activated cells in N1 and M51R single-cell microwell infections

Population level measures of fluorescent reporter protein and virus production indicate that the reporter protein signal is a reasonable indicator of virus production kinetics. In addition, other work from our group has shown that the ZSGreen signal emanating from our immune activated IFIT2 reporter PC3 cell line also correlates with some indicators of anti-viral activity (Swick n.d.), including similar kinetics and levels for ZSGreen and IFIT2 mRNA in infected cells and an increase in Mx1 protein levels. Further, by placing either one of these two fluorescent reporters (ZSGreen or DSRed Express) in the same viral backbone, it was shown that these two reporters have very similar translation and maturation kinetics. Therefore, the IFIT2 and viral reporter protein kinetics can be directly compared to each other (Swick n.d.).

PC3-IFIT2 cells were infected in solution with either N1-DSRed virus or M51R-DSRed virus. These infected reporter cells were seeded into a PDMS microwell device and imaged over the next 25 hours. Approximately 1000 isolated single-cells were imaged at each virus condition and about one-third of that population became infected (as indicated by a positive virus-reporter signal). Figure 2.3-3 is a representation of the number of infected, activated, and infected-activated cells in both populations. In general, IFIT2 production was not detected in RFP+ PC3-IFIT2 cells infected with N1-DSRed, while most cells infected with the M51R strain did appear to mount an immune response. These results are consistent with population level studies of PC3-IFIT2 cells infected with these two virus strains. Note also that the cell population infected with M51R virus had a higher percentage of cells that were only positive for the host GFP than did the population infected with N1 (5.2% - M51R, 2.8% - N1, $p=0.04$). The basal level of GFP positive PC3-IFIT2 cells in a population is usually ~1%.

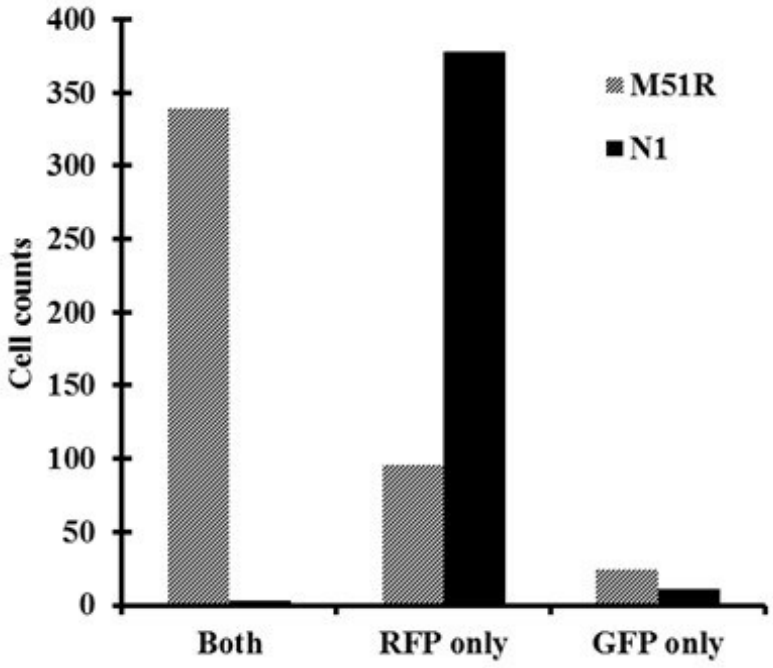

Figure 2.3-3: Counts of cells infected with either N1-DSRed (black) or M51R-DSRed (grey) that are positive for both RFP and GFP, RFP only, or GFP only.

2.3.4 Definitions of kinetic parameters

We plotted fluorescence intensity versus time of both the RFP (viral protein) and GFP (IFIT2 activation) data from each individual cell. Figure 2.3-4 illustrates the different measures and fitted parameters that were extracted from each single-cell trajectory. In general, the trajectories of both the virus and IFIT2 reporters are similar; beginning with a period of no detection that includes the time between the initial infection and initial protein production and then an additional delay while the reporter protein is accumulating, but is not yet detectable. Once the reporter protein is detected, a rapid growth phase follows, which eventually slows and levels off to a plateau. We found that an exponential function (Intensity = $Ae^{\alpha*time}$) fit the early time points well, and we only used the results when the R^2 value was ≥ 0.9 (88% of RFP+ cells, 86% of

GFP+ cells). We extracted an estimated production rate parameter, alpha, from the fluorescent intensity signal for both viral RFP and cellular GFP. We were able to extract several other kinetic parameters from both the virus and the innate immune reporters, including a delay-time to detection, a maximum intensity, and a rise-time for each individual cell (Figure 2.3-4). Finally, a lysis-time was extracted for cells that lysed before the end of the experiment. To obtain the results presented below, only single-cells that expressed *both the virus and IFIT2 reporter* were considered unless otherwise specified.

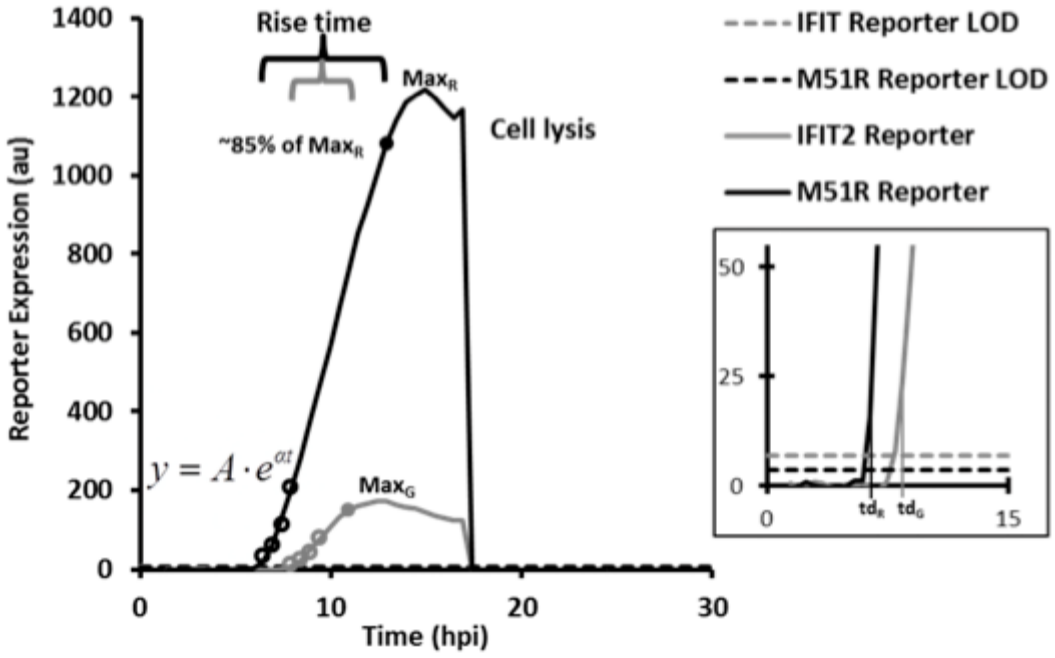

Figure 2.3-4: Illustration of the different kinetic parameters that are extracted from reporter trajectories. The inset figure magnifies the RFP and GFP trajectories near their respective limits of detection.

2.3.5 Immune activation affects virus reporter kinetics

We begin our analysis by investigating how the parameters of time (i.e., rise-time) and production rate (i.e., α) from the exponential function are related to virus reporter production. The rise-time encompasses the majority of the detectable reporter protein production time, and varies greatly from less than 30 minutes to nearly 15.5 hours (Figure 2.3-5). Two other key parameters are the production rate (alpha) and the maximum reporter intensity. Both the production rate and max intensity vary more than two orders of magnitude for both reporter proteins, demonstrating the incredible variability in these virus-host systems. We wished to determine if a relationship exists between these kinetic parameters of rise-time and production rate and the maximum intensity, so we plotted the maximum intensity on a natural log-scale versus the rise-time, the production rate, and a combination of the rise-time and production rate (Figure 2.3-5). Each data point on these plots represents kinetic parameters extracted from the virus reporter trajectories of a single-infected cell. We have also separated these data into lysed (red circles) and intact (black circles) cell populations to determine if any of these factors are more correlated with cell lysis events.

2.3.5.1 GFP+RFP+ cells

In these M51R-DSRed infections of resistant PC3 cells we find that in cells expressing both the virus and IFIT2 reporters (74% of cells), the rise-time (R^2 = 0.41) is actually a better predictor of virus reporter expression yields than is the production rate (R^2 = 0.24) (Figure 2.3-5a & b). Further, the multiplication of these two parameters is more predictive still with an R^2 value of 0.53 (Figure 2.3-5c). This result is somewhat intuitive – the production rate multiplied by the production time should be linearly related to the log of the yield. However, this relationship would depend upon the production rate and the rise-time being independent, so we have also

plotted this relationship. Figure 2.3-5d shows that the virus reporter production rates appear to be constant over the range of rise-times.

One of the advantages of imaging single-cells in microwells is that we can very easily see instances of cell lysis or any leaking of reporter signal from the cell into the surrounding media. We were interested in any correlations that might exist between cell lysis events and any of the kinetic parameters we measured. An examination of the lysed (red circles) and intact (black circles) populations revealed only one significant difference, a higher average viral reporter production rate in the lysed population ($\alpha = 1.34$) compared to the intact population ($\alpha = 1.22$) (Mann-Whitney, $p = 0.004$). Because the higher production rate is correlated with lysis, we might have expected the rise-times to be shorter in the lysed cell population; however, we have already shown that these two parameters are independent and the same statistical tests show that the average rise-time is not significantly reduced in the lysed cell population.

2.3.5.2 GFP-RFP+ cells

The same series of plots was created using the population of M51R infected cells in which we did not detect a GFP signal (22% of RFP positive cells). The relationship between the maximum reporter intensity and the rise-time and production rate (alpha) parameters differed in this population of cells, which are either weakly activated or un-activated. Here we find that the production rate ($R^2 = 0.72$), not the combination of production rate and rise-time ($R^2 = 0.61$), is the best predictor of reporter protein yield. It also appears that the rise-time and production rate parameters might not be independent.

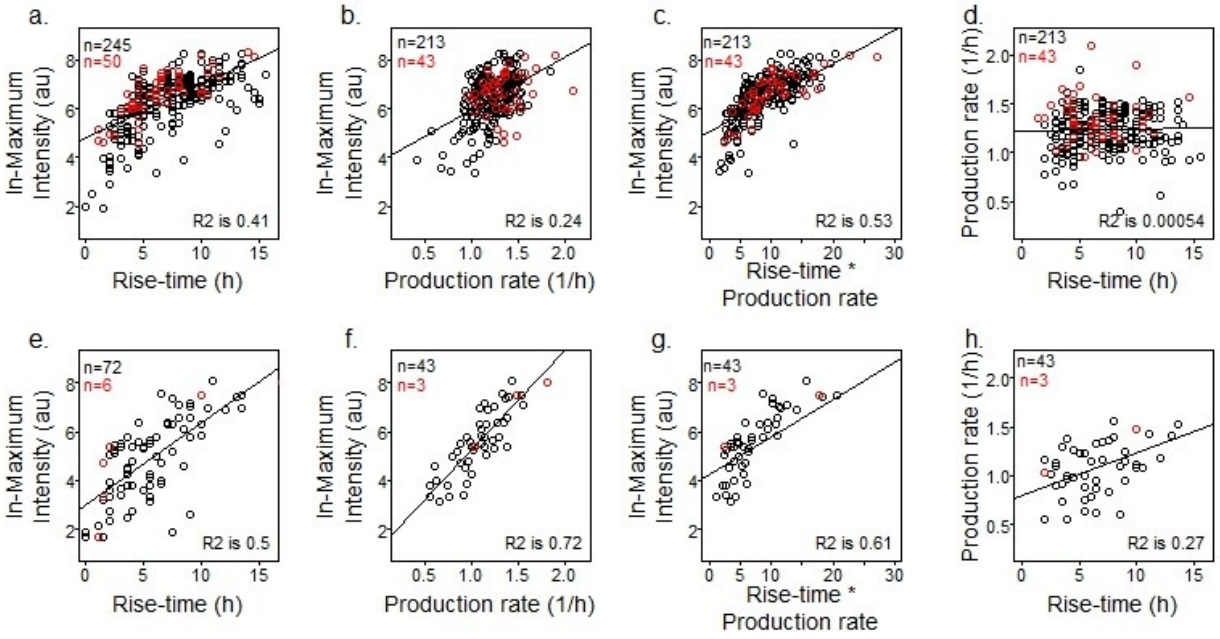

Figure 2.3-5: Relationship between maximum viral reporter intensities and the parameters of rate and time. (top, left to right) Virus reporter parameters from RFP and GFP positive cells, natural log of the maximum reporter intensity plotted against rise time, production rate, and the product of the rise-time and rates. Last plot is the production rate plotted against the rise-time. (bottom) Same series of figures for the RFP positive, GFP negative cells population.

2.3.6 Correlations between parameters of IFIT2 activation

2.3.6.1 GFP+RFP+ cells

We compiled the same series of figures for the host using parameters extracted from the IFIT2 reporter trajectories to determine if the relationships between the various kinetic properties were similar. Plotting the log of the maximum IFIT2 reporter expression versus the rise-time, the production rate, or the combination of the two revealed different results compared to the virus reporter. Unlike the virus reporter result, the maximum expression level is most correlated with the production rate ($R^2 = 0.54$) (Figure 2.3-6b), whereas the yields appear to depend very little on the rise-times ($R^2 = 0.14$) (Figure 2.3-6a). A comparison of the rise-time and production rate

suggests an answer (Figure 2.3-6d). The IFIT2 reporter rise-time distribution is narrower than that of the virus reporter, with a median time of 3.5 h (compared to 6.5 h for the virus) and with 75% of cells having a rise-time of 6 hours or less. There are no significant differences in the kinetic parameters of the IFIT2 reporter when comparing the lysed and intact cell populations.

2.3.6.2 GFP+RFP- cells

There were generally too few examples of cells that were GFP positive and RFP negative and so we did not perform an analysis similar to that performed for the virus reporter parameters in section 2.3.5. However, in this small population we observed that the percentage of cells that are GFP+ and RFP- is higher in the M51R-infected population than in the N1-infected population.

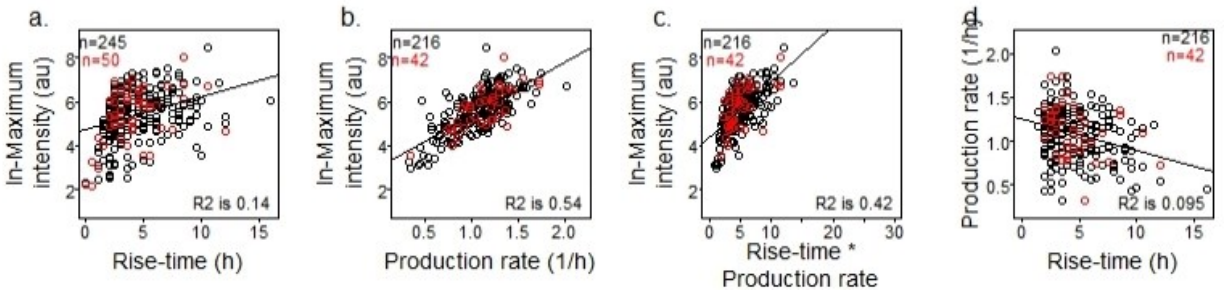

Figure 2.3-6: Relationship between the maximum IFIT2 reporter intensity and the parameters of rate and time. (Left to right) Natural log of maximum IFIT2 expression plotted against the rise-time, production rate approximation, and production of rise-time and production rate. Last plot is the production rate vs. the rise-time.

2.3.7 Relative reporter detection times influence resource allocation

Up to this point, our analysis has focused primarily on how one kinetic parameter relates to another within a single color - either the virus reporter or the innate immune reporter, but not both. The greatest strength of this new single-cell infection platform, however, is our ability to directly compare the virus and host state in isolated single-cells.

We have studied how detection times for both the virus and IFIT2 reporters relate to the fluorescent outcomes of these infections. The delay-time comparison plot shown in Figure 2.3-7c shows that detection of the IFIT2 reporter generally follows detection of the virus reporter (80% of cells). The IFIT2 median delay-time is 8.4 hpi, while the median delay-time for the virus reporter is 6.4 hpi. More thorough examinations of the delay-time distributions for the virus and IFIT2 reporters are shown in Figure 2.3-7a and b. Note there is a population of cells which express GFP well before any virus reporter is ever detected.

The delay-time comparison plot of IFIT2 and virus delays shows that the difference in detection times between the virus and IFIT2 reporter is highly variable. To determine how this might affect infection outcomes, we plotted the ratio of the virus and IFIT2 maximum intensity levels against the difference in delay-times (Figure 2.3-7d). The results appeared to show three different scenarios: when the delay-times are very similar, there is a lot of variability in the ratios, indicating competition between the virus and the host, but if the IFIT2 reporter is detected long after the virus reporter or if the virus reporter is detected long after the IFIT2 reporter, either the virus or the host cell appears to gain an advantage. To investigate these three potential populations further, we fit the following piecewise equation to this data:

Equation 2.3-1

$$y = \begin{cases} y_1 & x < x_1 \\ \dfrac{y_2 - y_1}{x_2 - x_1} \cdot (x - 1) + y_2 & x_1 < x < x_2 \\ y_2 & x > x_2 \end{cases}$$

The results of this fit showed that if the IFIT2 reporter was detected more than 4.7 hours before the virus reporter, the protein production resources appeared to shift in favor of the innate

immune response. If however, the virus reporter was detected more than 6 hours before the IFIT2 reporter, we observed the opposite result, and protein production resources appeared to shift in favor the virus.

Instead of comparing to relative max-intensities, we can also compare delay-times to absolute max intensities directly. A variety of factors, will affect the production capacity of a given cell, and so there is no fixed magnitude of reporter protein production that must be shared between the virus and host. Therefore, we next plotted the magnitudes of IFIT2 reporter expression when the virus reporter was detected first (Figure 2.3-7f) and the magnitudes of virus reporter expression when the IFIT2 reporter was detected first (Figure 2.3-7e). There is a great deal of variability in the max-intensity magnitudes, but as the time advantage increases for either the virus or the IFIT2 reporter, the range of potential max-intensity values decreases.

2.3.8 IFIT2 response depends on infection but not virus replication processes

It is clear from the delay-time results that the IFIT2 reporter generally responds to some virus infection process. The PC3-IFIT2 cell detects the virus and responds, and that response results in the production of IFIT2 and the IFIT2 reporter protein. We noted in Figure 2.3-7 that the timing of this response is very important to the infection outcome. We wanted to evaluate the kinetic data further, and determine if the host continues to respond to virus replication processes, or if the rates and magnitudes of IFIT2 production act independently of viral processes after the initial activation. The way in which IFIT2 kinetic parameters were related to the virus production rate was of particular interest because of our finding that a higher average virus reporter production rate was correlated with lysis. Therefore, we have plotted all IFIT2 kinetic parameters against the

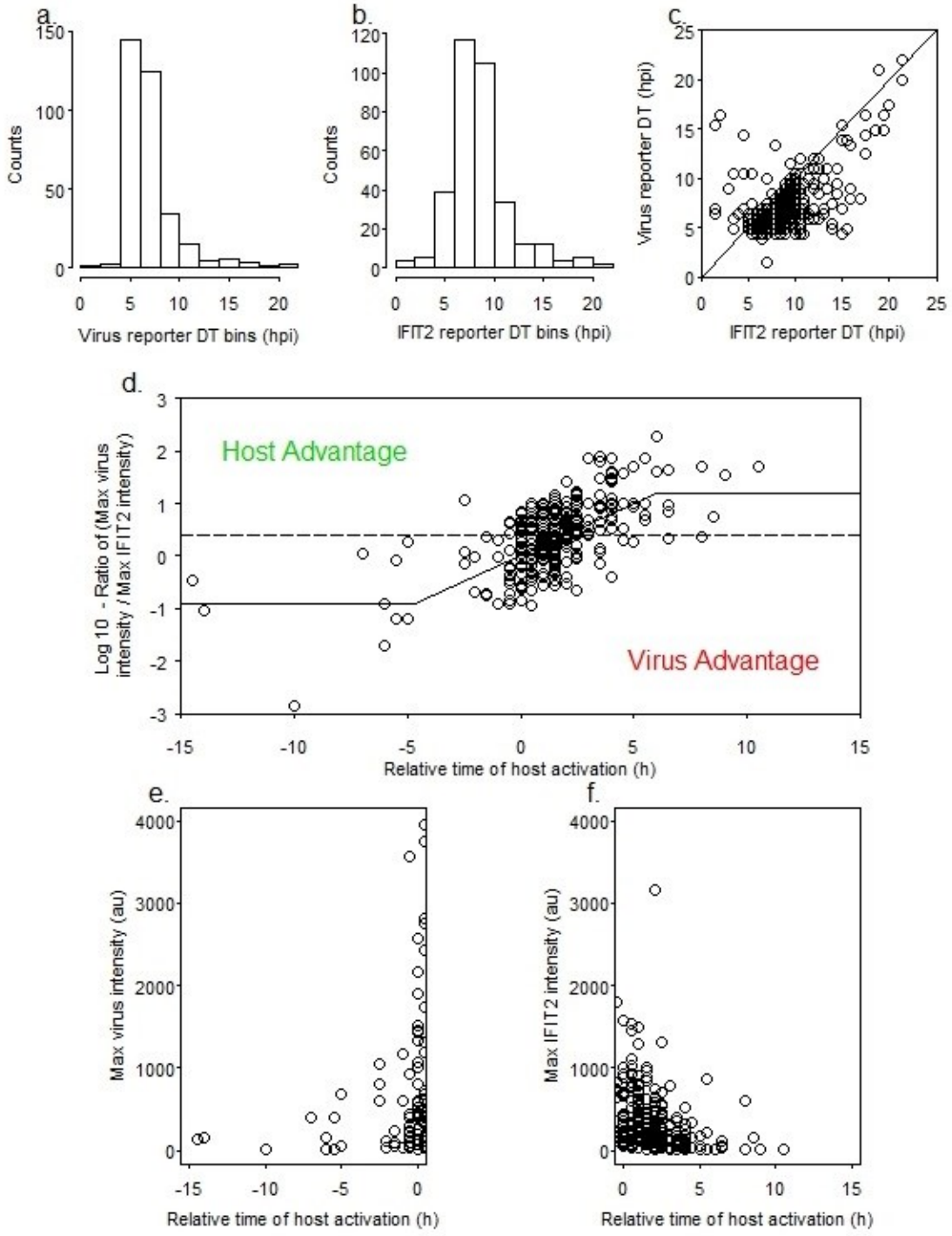

Figure 2.3-7: Relative delay-times to detection of the virus and IFIT2 reporters affect the outcomes of M51R-DSRed infections of PC3 cells. (a) Histogram of virus reporter delay-times. (b) Histogram of IFIT2 reporter delay-times. (c) Comparison plot of the virus and IFIT2 delay-times for each individual RFP and GFP positive cell. (d) Ratio of virus and IFIT2 maximum intensities plotted against the Relative time of host activation, which is equal to (IFIT2 delay-time – the virus reporter delay-time) (e) Maximum virus intensity

plotted against the relative time of host activation when the cell has the time advantage. (f) Maximum IFIT2 reporter intensity plotted against the relative time of host activation for when the virus has the advantage.

virus production rate in Figure 2.3-8. In every case we found that these parameters appeared to be independent - the production rates, magnitudes, delay-times and rise-times of IFIT2 production are not correlated to the rate of virus reporter production.

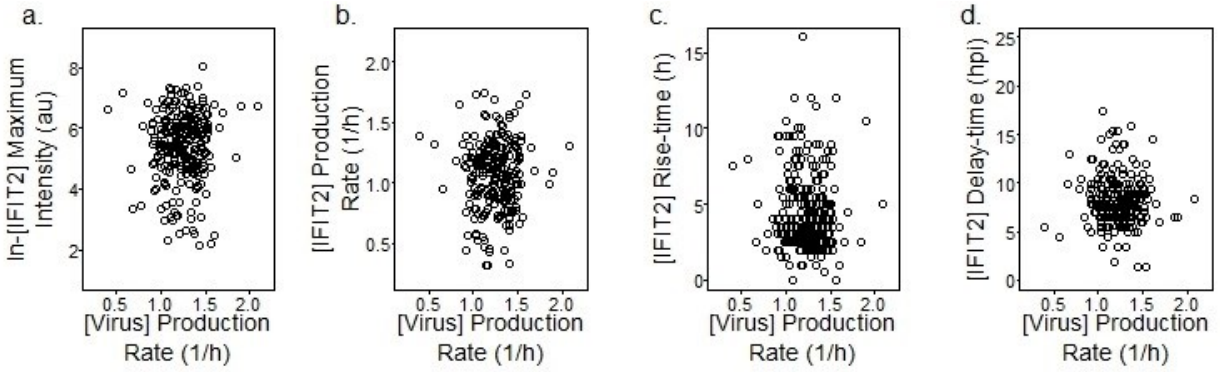

Figure 2.3-8: IFIT2 expression occurs in response to infection, but not specific viral replication processes. (Left to right) Natural log of maximum IFIT2 reporter intensity, IFIT2 production rate, IFIT2 rise-time, and IFIT2 delay-time all plotted against the virus reporter production rate.

2.4 Discussion

Virus-host interactions are complex, both in the myriad strategies viruses have evolved to infect cells and evade their innate immune systems to replicate and spread, and in the way host cells have evolved to detect and suppress virus infection, while warning neighboring cells of potential danger. In order to gain a better understanding of such interactions we have developed new tools that allow us to study single-cell behaviors in a high-throughput manner. Our high-throughput platform for studying single-cell virus infections includes a PDMS microwell device,

an automated live-cell imaging system, image processing and data-basing software (JEX), and computational tools for analyzing large data sets. Utilizing a dual-color reporter system, which was previously developed in our lab (Swick n.d.), and combining this system with our new platform for high-throughput single-cell analysis, we are able to analyze hundreds or thousands of isolated single-cells, under multiple conditions, in parallel.

Vital to this work is the reporter cell system used to demonstrate the type of data that we can acquire using our assay and to suggest potential applications using these single-cell tools. Biological tools such as reporter cell lines and viruses have become an invaluable research instruments and this type of simple, non-destructive image-based readout is very important for high-throughput technology. Properly designed reporter systems can provide so much more information than a simple indicator, and have the potential to become quantitative, kinetic readouts when used properly. Every test of the dual-color reporter system used in this work has suggested that both the virus and innate immune reporters are accurately relating the state of intracellular virus and host activity, both in population and single-cell experiments. Examples include the population level reporter kinetics, which correlate with virus production kinetics (Figure 2.3-2) and activation of the IFIT2 reporter, which is much more prevalent in M51R infections than in N1 infections where such activation should be suppressed (Figure 2.3-3). This reporter system is potentially powerful in enabling quantitative characterization of VSV infections of PC3 cells in real time. However, more work must be done to determine if the production rates, yields, or other kinetic parameters of these reporters can be quantitatively connected to infectious virus yields and anti-viral activity.

In addition to indicating a relationship between the viral RFP and yields, the population level one-step infections showed that in order to achieve a synchronized infection in resistant PC3

cells, a very high MOI is required (Figure 2.3-1, Figure 2.3-2). Additionally, PC3 cells infected with a high multiplicity of either N1-DSRed or the mutant strain, M51R-DSRed, produce thousands of infectious virus particles per cell, with less than a 2-fold decrease in yields between the N1 virus and the mutant M51R that is unable to shut down the host immune response (9200 PFU/cell – N1, 6200 PFU/cell – M51R). These similar yields indicate one of two things – either the high MOI is sufficient to overwhelm the host innate immune response or resistance requires forewarning of infection, which cannot occur in a synchronized infection. Without perturbing the system further, this is the limit of information that we can gather from these experiments. We cannot detect that heterogeneity we know exists using standard cell culture methods. Single-cell infections allow us to observe a range of different scenarios on both the virus and host side, all beginning with the same experimental conditions.

We have previously studied the kinetics of VSV production from isolated BHK cells. These results, however, were collected from only 12 isolated single-cells because we were limited by the 96-well format and the time consuming plaque assays required to quantify virus production. Here we use the fluorescent reporter as a proxy for virus production and by doing so, we can increase the throughput and study hundreds or thousands of cells under different conditions and in parallel. Our previous work in the permissive BHK cells was used as a benchmark for analysis of this new data. For example, measuring the kinetics of infectious WT-VSV production in single-cells showed that the maximum rate of virus production was highly correlated to virus yields in infections of BHK cells (Timm 2012). We also determined that the yields could vary greatly, more than 2 orders of magnitude, while the delay-times were quite uniform, varying less than 2-fold from the earliest to latest delay-time. In contrast, these M51R-DSRed infections of resistant PC3 cells showed that the virus reporter production rate was not as correlated with

maximum virus reporter intensities as the production rate combined with the rise-time. Also, other parameters varied greatly, including the delay-time to detection of infection, which varied from ~ 3 hpi to more than 22 hpi. In cells without a detectable immune response (GFP-), our results were more similar to WT-VSV infections of BHK cells in that the production rate was most correlated with the maximum virus reporter intensity. Table 2.4-1 shows how the other parameters compare between GFP+ and GFP- M51R infected cells. Initially, the lower virus reporter production rates (1.09 vs. 1.24) and maximum intensities (378 vs. 854) extracted from the virus reporter trajectories might suggest that cell health was compromised in cells that did not express detectable levels of the IFIT2 reporter (GFP-).

Table 2.4-1: Virus reporter parameter comparison between the GFP positive and GFP negative populations of M51R infected cells. The mean, mean adjusted deviation, and standard deviation of these parameters are shown.

	GFP Positive			GFP Negative		
Parameter	Mean	Mad	Standard Deviation	Mean	Mad	Standard Deviation
Delay-Time	7.1	1.48	2.7	9.6	3.71	5.13
Max Intensity	854	569	753	378	154	634
Rise-Time	6.84	2.97	3.23	5.12	3.71	3.63
Alpha	1.24	.20	.21	1.09	.27	.28
Lysis Rate	12%			4.9%		

However, the range of all these kinetic parameters is very similar, and the data is generally more uniform with better correlations (see Figure 2.3-5). Furthermore, the lysis rates are higher in

GFP+ cells than in GFP- cells (p=0.01). We would not expect to see more uniform behavior, and lower lysis rates in less healthy cells. These results do not indicate that cell health is the issue, but instead indicate some relationship between IFIT2 activation and production of the viral reporter.

We are aware of two aspects of IFIT2 activation that may relate to anti-viral activity, and potentially affect virus reporter production. First, IFIT2 is known to be an indicator of a pro-apoptotic environment (Stawowczyk 2011; Reich 2013), and second IFIT2 has been implicated as a suppressor of translation through an interaction with eIF3 (Terenzi 2006). When comparing the GFP+ and GFP- populations, we noted a higher lysis rate in GFP+ cells infected with M51R (12% vs. 5 %, p=0.01). This higher lysis rate may be caused by the anti-viral response in GFP+ PC3-IFIT2 cells. We looked for indications of this by analyzing the rise-time data, which may be shortened by lysis based on its definition. We found that the rise-time affected maximum virus reporter intensities more in GFP+ cells than in GFP- cells (Figure 2.3-5). We also found, that the virus reporter production rate was the only parameter that was significantly different when comparing lysed and intact cell populations (lysed α=1.34, intact α=1.22, p=0.004). While we know from our delay-time results that IFIT2 reporter activation usually occurs as a response to virus infection (Figure 2.3-7c), we were not sure if IFIT2 production would continue to be influenced by viral replication processes. The correlation between virus reporter production rates and lysis indicated that this viral process might be affecting IFIT2 production. We tested this hypothesis by looking for correlations between the virus reporter production rate and all IFIT2 reporter kinetic parameters and found no correlations existed. These results suggest that IFIT2 production occurs in response to virus infection, but that the duration and kinetics of IFIT2 production do not continue to respond to virus replication processes.

IFIT2 affects viral infections by inhibiting translation through interaction with eIF3 (Terenzi 2006). We expected to find higher IFIT2 reporter expression associated with lower virus reporter production rates or maximum intensities, but we did not observe a reduction in either parameter with any increase in IFIT2 reporter production. We did observe that the relative delay-times of IFIT2 and virus detection were important to infection outcomes. Three general infection phenotypes, or subpopulations, could be distinguished based on the delay-time results. When the host-cell has a delay-time advantage (relative time to host activation is negative), the max intensity ratio appears to shift in the host's advantage (Figure 2.3-7d). Likewise, when the virus seems to have a delay-time advantage, we observe that the max-intensity ratio shifts in favor of the virus. The shifting ratios are in agreement with a role for IFIT2 in suppression of viral translation when IFIT2 has a head start. It is also possible that some other ISG with similar activation kinetics is affecting VSV replication, and our IFIT2 reporter is acting as a general representative of the cellular immune response. The shifting ratios indicate that resources might be allocated depending on the relative timing of events in cells. We next plotted the magnitudes of maximum reporter intensities against the relative time of host activation. We observe a lot of variability initially in the virus reporter expression, but as the host's time advantage increases, we observe a significant limitation on the amount of virus reporter protein produced (Figure 2.3-7e). The relationship is the same when the virus reporter has a time advantage and we plot the IFIT2 reporter maximum intensities. Notably, an analysis of the relative kinetics of IFIT2 and virus reporters allows us to see that the timing of events is just as important as the events themselves. Endpoint or population level measures would mask these results.

One of the more surprising results of this work showed that the GFP+ cell population had a higher overall RFP intensity than the GFP- cell population. Additionally, the rate of virus

production (alpha) was higher in the GFP+ population than in the GFP- population. The decrease in intensity and rate in the GFP- population is not related to cell health, but instead seems to indicate that the anti-viral response can actually favor VSV production in the short term. In contrast, the delay-time data suggests that cells activated earlier, generally produced less viral protein (Figure 2.3-7). We know that activating a cell's innate immune response, perhaps with IFN treatments, before infection reduces viral yields (Trottier 2005). It is well known that the paracrine signaling resulting from activation of the type I interferon pathway slows the spread of VSV infection (Lam 2005). Therefore, if we consider this virus-host system in the more natural context of a spreading rather than a synchronized infection, the host might be best served to ramp up transcriptional and translational activity in the cells in order to signal uninfected neighboring cells of a potential threat. Evolutionarily, the virus must then meet that challenge by inhibiting cellular processes or out-competing the innate immune system. Two things VSV does to overwhelm the innate immunity of its host are block nuclear export of mRNA (wt only, not M51R) and replicate very fast and to very high titers. Therefore, we hypothesize that PC3 cells that initiate an immune response and successfully warn their uninfected neighbors, are also in a highly productive state that allows greater production of VSV (as evidence by the higher rates and intensities of the GFP+ single-cell population), but that given a sufficient time advantage the innate immune response of the cells can suppress virus production (delay-time results). This hypothesis, which is based on the data collected from hundreds of single-cells in one experiment, demonstrates the depth of information that can be gained from analyzing the heterogeneity in a biological system rather than average outcomes.

2.5 Acknowledgements

This work was aided by a collaboration with Jay Warrick, Ph.D. and is featured in a joint publication in progress.

2.6 References

1. **Ahmed, M., and D. S. Lyles**. 1997. Identification of a consensus mutation in M protein of vesicular stomatitis virus from persistently infected cells that affects inhibition of host-directed gene expression. Virology 237:378–388.

2. **Barr, J., S. Whelan, and G. Wertz**. 1997. Role of the intergenic dinucleotide in vesicular stomatitis virus RNA transcription. Journal of virology 71:1794–1801.

3. **Carey, B. L., M. Ahmed, S. Puckett, and D. S. Lyles**. 2008. Early steps of the virus replication cycle are inhibited in prostate cancer cells resistant to oncolytic vesicular stomatitis virus. Journal of virology 82:12104–15.

4. **Delbruck, M.** 1945. The burst size distribution in the growth of bacterial viruses (bacteriophages). Journal of bacteriology 50:131–5.

5. **Elowitz, M. B., A. J. Levine, E. D. Siggia, and P. S. Swain**. 2002. Stochastic gene expression in a single cell. Science 297:1183–1186.

6. **Fensterl, V., J. L. Wetzel, S. Ramachandran, T. Ogino, S. a Stohlman, C. C. Bergmann, M. S. Diamond, et al.** 2012. Interferon-induced Ifit2/ISG54 protects mice from lethal VSV neuropathogenesis. PLoS pathogens 8:1–13.

7. **Flint, S. J., L. W. Enquist, V. R. Racaniello, and A. M. Skalka**. 2009. Principles of Virology, Vol II (3rd ed., pp. 52–84). ASM Press, Washington D.C.

8. **He, Y., K. Xu, B. Keiner, J. Zhou, V. Czudai, T. Li, Z. Chen, et al.** 2010. Influenza A Virus Replication Induces Cell Cycle Arrest in G0/G1 Phase. Journal of Virology 84:12832–12840.

9. **Lam, V., K. a Duca, and J. Yin**. 2005. Arrested spread of vesicular stomatitis virus infections in vitro depends on interferon-mediated antiviral activity. Biotechnology and bioengineering 90:793–804.

10. **Levin, D., D. Harari, and G. Schreiber**. 2011. Stochastic receptor expression determines cell fate upon interferon treatment. Molecular and cellular biology 31:3252–66.

11. **Lwoff, a, R. Dulbecco, M. Vogt, and M. Lwoff**. 1955. Kinetics of the release of poliomyelitis virus from single cells. Virology 1:801–805.

12. **Lyles, D. S., and C. E. Rupprecht**. 2007. Rhabdoviridae. In D. Knipe & P. Howley, eds., Fields Virology (5th ed., pp. 1363–1408). Lippincott Williams & Wilkins, Philadelphia, PA.

13. **Müller, U., U. Steinhoff, L. F. L. Reis, S. Hemmi, J. Pavlovic, M. Zinkernagel, M. Aguet, et al.** 2013. Functional Role of Type I and Type 11 in Antiviral Interferons Defense 264:1918–1921.

14. **Oliere, S., M. Arguello, T. Mesplede, V. Tumilasci, P. Nakhaei, D. Stojdl, N. Sonenberg, et al.** 2008. Vesicular stomatitis virus oncolysis of T lymphocytes requires cell cycle entry and translation initiation. Journal of Virology 82:5735–5749.

15. **Rand, U., M. Rinas, J. Schwerk, G. Nöhren, M. Linnes, A. Kröger, M. Flossdorf, et al.** 2012. Multi-layered stochasticity and paracrine signal propagation shape the type-I interferon response. Molecular systems biology 8:584.

16. **Reich, N. C.** 2013. A death-promoting role for ISG54/IFIT2. Journal of interferon & cytokine research : the official journal of the International Society for Interferon and Cytokine Research 33:199–205.

17. **Snijder, B., R. Sacher, P. Rämö, E.-M. Damm, P. Liberali, and L. Pelkmans**. 2009. Population context determines cell-to-cell variability in endocytosis and virus infection. Nature 461:520–3.

18. **Stawowczyk, M., S. Van Scoy, K. P. Kumar, and N. C. Reich**. 2011. The interferon stimulated gene 54 promotes apoptosis. The Journal of biological chemistry 286:7257–66.

19. **Swick, A., A. Baltes, and J. Yin**. 2014. Visualizing infection spread: dual-color fluorescent reporting of virus-host interactions. Biotechnology and Bioengineering.

20. **Terenzi, F., D. J. Hui, W. C. Merrick, and G. C. Sen**. 2006. Distinct induction patterns and functions of two closely related interferon-inducible human genes, ISG54 and ISG56. The Journal of biological chemistry 281:34064–71.

21. **Timm, A., and J. Yin**. 2012. Kinetics of virus production from single cells. Virology 424:11–7.

22. **Timm, C., A. Gupta, and J. Yin**. 2013. Kinetics of transcription and replication for an RNA virus: from simple to complex. Journal of Virology, waiting for submission.

23. **Trottier, M. D., B. M. Palian, and C. S. Reiss**. 2005. VSV replication in neurons is inhibited by type I IFN at multiple stages of infection. Virology 333:215–25.

24. **Volfson, D., J. Marciniak, W. J. Blake, N. Ostroff, L. S. Tsimring, and J. Hasty**. 2006. Origins of extrinsic variability in eukaryotic gene expression. Nature 439:861–4.

25. **Waters, J. C.** 2009. Accuracy and precision in quantitative fluorescence microscopy. The Journal of cell biology 185:1135–48.

26. **Zhao, M., J. Zhang, H. Phatnani, S. Scheu, and T. Maniatis**. 2012. Stochastic expression of the interferon-β gene. PLoS biology 10:1–16.

27. **Zhu, Y., A. Yongky, and J. Yin**. 2009. Growth of an RNA virus in single cells reveals a broad fitness distribution. Virology 385:39–46.

Chapter 3: IFN-β pre-treatments shift advantage toward cells in competitive infections using a mechanism largely independent of IFIT2

3.1 Introduction

The parasitic relationship viruses have with their hosts is complex. In the simple case of a virus infecting a single cell in culture, the virus must be able to commandeer the host's resources, while either avoiding detection or suppressing the host's innate immune response. The cell must use its many detection methods and anti-viral signaling pathways to detect and suppress virus replication processes. Often, the outcome of the competition between a virus and its host depends on which side, the virus or the host, is able to 'win' early.

The interactions between viruses and their hosts is not nearly as simplistic as one virus infecting one host cell; this competition takes place over many scales that increase in complexity. However, the infection process must always begin with virus particles infecting individual cells in a tissue and spreading from there. The outcomes of isolated infections are variable in tissues and in the cell cultures used for scientific research. In Chapter 2, we discussed the development of methods that allow us to analyze this competition through the use of a virus-host system that contains fluorescent reporter genes. The PC3-IFIT2 reporter cell expresses ZSGreen when the IFIT2 gene becomes transcriptionally active, and the virus encodes the gene for DSRed-Express and this gene is transcribed along with all other viral genes during virus replication processes. The design of this reporter system was done by other members of the Yin lab and has been previously described and validated (Swick n.d., Chapter 2). We have shown that the relative reporter detection times appear to predict the infection outcomes. For example, when the IFIT2 reporter is detected long before the viral reporter in M51R-DSRed infected cells, the overall

intensity of the viral reporter is reduce compared to the average. Likewise, infections of cells in which we detect the virus reporter long before the IFIT2 reporter usually result in a lower overall level of the cellular GFP (Chapter 2). Another key finding from our previous work indicated that cells expressing the virus reporter, but not expressing the IFIT2 reporter, generally had lower average maximum intensities and slower production rates. Finally, we found that the lysis rates were higher in cells expressing both the viral RFP and cellular GFP, compared to the cells only expressing the viral RFP.

Based on these results, we hypothesized that in the more natural context of a spreading infection, it might be advantageous for infected cells to ramp up transcriptional activity in order to produce large quantities of anti-viral cytokines. VSV is known to be particularly sensitive to IFN treatments, and so secreted interferons activating an anti-viral response in un-infected peripheral cells could stall infection spread. Previous work has shown that treatment of a cell cultures with interferons slows the spread of a virus infection, and also shows that adding antibody against IFNs allows greater spread of virus infection than an untreated control sample (Lam 2005). An initial cell quickly producing cytokines that diffuse faster than the virus gives neighboring un-infected cells sufficient time to suppress a subsequent infection. Our hypothesis is in agreement with the higher levels of virus reporter protein in immune activated cells and the delay-time results (Chapter 2). Additionally, the higher lysis rates in immune activated cells may be a way to limit the amount of virus produced, while allowing higher amounts of viral protein (Chapter 2). We will explore this hypothesis further in this work.

Our goal here was to perturb the virus-host interaction by pre-treating the host-cells with IFN-β at different time intervals before infection. The PC3-IFIT2 cell line produces IFIT2 and ZSGreen when transcription of IFIT2 is stimulated. This activation is possible either through

activation of the IFN-β pathway or more directly after detection of viral infection (Terenzi 2006; Perwitasari 2011; Reich 2013). Using the IFN-β pretreatments, we hope to manipulate the delay-time distributions and investigate how this perturbation affects the activation of IFIT2 and the kinetics of the viral reporter protein production.

3.2 Materials and Methods

3.2.1 Cell and virus culture

BHK (baby hamster kidney), PC3 (prostate cancer) and PC3-IFIT2-ZsGreen1-DR (PC3-IFIT2) reporter cells were used in this work. The generation of the PC3-IFIT2 reporter cell line is described in Swick et al. (Swick n.d.). Briefly, a ZsGreen1-DR gene controlled by an IFIT2 promoter was stably transduced into PC3 cells. Activation of innate immune pathways that lead to production of IFIT2 in PC3 reporter cells, also lead to the production of the ZSGreen protein.

BHK cells were passaged every 2-3 days and grown in MEM (Cellgro) supplemented with 10% FBS (Atlanta Biologicals) and 2mM GlutaMAX (Gibco) and the PC3 and PC3-IFIT2 cells were passaged every 3-4 days and grown in RPMI 1640 (Gibco) supplemented with 10% FBS. Infections of the cells lines were done in the same media, but with the FBS content reduced to 2%. The viruses used are recombinant strains of vesicular stomatitis virus (VSV) encoding the gene for DSRed-Express protein in the fifth position of the genome, after the glycoprotein gene and before the polymerase gene. By placing the reporter gene in this position, attenuation caused by adding an additional gene is limited, but virus replication still results in a strong fluorescent signal. Both a wild-type (N1-DSRedEx) and mutant form (M51R-DSRedEx) were used and both stocked on BHK cells. The M51R strain has a methionine to arginine point mutation in the

matrix protein. This mutation prevents the matrix protein from functioning properly in its role to block nuclear export (Ahmed 1997).

3.2.2 Infections for mRNA kinetics and population one-step infections

The IFIT2 and IFN-β mRNA kinetics from IFN-β treated, M51R infected, or mock treated cells were determined using the following methods. PC3-IFIT2 cells were plated in four 12-well plates. Wells of one plate were used to determine a cell count for MOI calculations. Each of the other three plates were treated and sampled at multiple times to determine IFN-β and IFIT2 mRNA quantities. IFN-β was diluted in 2% FBS RPMI to 1000 units/well and this solution was added to the PC3-IFIT2 cell monolayers at the same time as virus was added to the M51R treated wells. Cell monolayers in 12 other wells were infected with an approximate MOI of 12 with M51R-VSV, and the remaining 10 wells were mock treated with 2% FBS RPMI. At times indicated on the plots, two wells at each condition were sampled by trypsinizing cells, neutralized with FBS-containing media, pelleted, and then re-suspended in RNAprotect Cell Reagent (Qiagen) for later use. These samples were frozen at -20°C. Immediately before the samples were collected, one plate was imaged using a Nikon Eclipse TE300 microscope to compare IFIT2 reporter expression to the mRNA kinetics.

3.2.3 RNA extraction, reverse transcription, and qPCR

Cell-associated RNA samples frozen in RNAprotect were thawed and the RNA extracted using the RNeasy Mini Kit (Qiagen). RNA extraction was followed immediately by reverse transcription using the GoScript Reverse Transcriptase system (Promega) and random priming. 3.15µl of undiluted RNA was mixed with 2µl of 10µM random primers (0.223µg/µl) and incubated at 70°C for 5 min, then immediately transferred to a frozen tray. After 10 min, 1.85µl

of 25 mM $MgCl_2$, 0.5µl nucleotides (0.5mM each), and 0.5µl GoScript Reverse Transcriptase was added to a final volume of 10µl.

Total RNA content after RNA extraction was measured for each sample with the NanoDrop and this information was used to normalize the various samples to total RNA content after qPCR, which was performed using the cDNA product of the reverse transcription, SsoFast Supermix (BioRad), and primer sets for the following genes: IFIT2, IFN-β, IFITM3, CH25H, and PARP12. All primers were purchased from IDT. The IFIT2 and IFN-β primers have been used in Swick et al. (Swick n.d.). Sequences of the other primers are listed below. Prior to qPCR, the cDNA product was diluted 1:5 and then 2µl of these samples were added to 8µl of a reaction master mix. The master mix contained 5µl SsoFast Supermix, 1.2µl of 5µM each primer mix, and 1.8µl RNase free water. Serial dilutions of the sample containing highest predicted mRNA amounts were used to make a standard curve. Measurements were compared to the mock-treated sample taken at the first time-point.

IFITM3 primer 1: **5'-CGTGCACTTTATTGAATGCCA-3'**
IFITM3 primer 2: **5'-CGTACTCCAACTTCCATTCCTC-3'**

CH25H primer 1: **5'-TGTGTAAAGTACGGAGCGAAG-3'**
CH25H primer 2: **5'-CTTGGTCCACTCACAGACTG-3'**

PARP12 primer 1: **5'-CTTCTCCACGTCGCTACTG-3'**
PARP12 primer2: **5'-CCTCCACACTTCATCCTCAC-3'**

3.2.4 Bull's-eye device seeding and assembly

3.2.4.1 Device preparation

Approximately 1 hour before beginning the infection procedure, the PDMS device was placed under a UV lamp for sterilization. (A thorough description of the dimensions of the Bull's-eye device is described in Section 1.2.2. Also included in Section 1.2.2 are the methods used to make the devices). After 20-30 minutes, the device was moved to a vacuum chamber for de-gassing. This step is critical, as it allows liquid to readily fill the wells instead of trapping air underneath the liquid layer. After 20 minutes in the vacuum chamber, 100µl droplets of infection media (containing HEPES and Hoechst) were placed on each bull's-eye to wet the device. There is sufficient surface tension to keep droplets from spilling into the moats. It is necessary to ensure that all wells are covered with fluid, as empty wells will speed up drying later in the infection. The PDMS device was placed in an incubator, with the droplets in place before beginning the infection procedure. The device was in this humid environment for approximately 1 hour before cell seeding began.

3.2.4.2 Cell seeding

To seed the infected cells into the microwell device, the existing droplets were removed and replaced with 70-80µl droplets of the infected cell solution (1-2 x 10^5 cells/ml). After 30-60 seconds, the droplets were removed swiftly by placing the pipette tip in the recessed center and replaced quickly, but gently with fresh media. The swift removal of the droplets sweeps cells off the top surface of the device, but does not disturb the cells that have settled into the microwells. It is necessary to keep the pipette vertical and not pipette from an angle. The bull's-eyes were washed with fresh media twice more in the same manner. It is important not to overload the wells with cells, as they are difficult to wash away once seeded and overloading will cause cells

to become trapped outside the wells and crushed during sealing. The nuclear stain of these cells will still be visible and will interfere with image analysis.

3.2.4.3 Device sealing

The device was sealed by quickly removing the droplets from all bull's-eyes and gently covering with a glass slide (top side treated with 0.1% Tween 20). It is important not to add and then release pressure to the microwells as this causes bubbles to form and displaces cells. The tween is applied by pipetting on ~ 1 ml of 0.1% tween, then before sealing, removing all but a thin layer of the solution. Tween 20 (Fisher Scientific) is a surfactant that prevents condensation droplets from forming on the top side of the sandwich device when inside the humid microscope chamber; instead, an even layer of liquid forms. The liquid layer does not affect fluorescence, and an even liquid layer instead of droplets allows for better topside phase contrast images. Pressure is applied to maintain the sealing as described in Section 1.2.2. Pressure was applied to enable complete sealing of the microwells, but without permitting glass slides to break.

In this experiment, two bull's-eyes were seeded with un-infected cells to determine cell viability after 24 hours of imaging, three bull's-eyes were seeded with M51R-infected cells pretreated with IFN-β for 6-hours, three were seeded with M51R-infected cells pretreated with IFN-β for 3-hours, and two were seeded with M51R-infected cells that received a mock pre-treatment of fresh 10% FBS media.

3.2.5 Time-lapse imaging

As described in Section 1.2.3.1, correction images were taken before beginning the time-lapse to correct for uneven light intensity. The exposure times for the illumination correction

images was 5ms and the exposure time for the dark field correction images was 2000ms (or the longest exposure time used).

The aluminum device holder containing the bull's-eye device and several DPBS soaked Kim-wipes was placed on the automated microscope stage. The DPBS soaked Kim-wipes help provide a humid environment for the PDMS device. Fluorescent time-lapse imaging was done on a Nikon Eclipse TE300 microscope, using an EXI aqua camera (Q Imaging). The environmental conditions were controlled by an outer warming chamber encompassing the microscope and a stage-top incubator chamber (Pathology Devices) set to 37°C, 5% CO_2, and approximately 85% RH. Once the system had equilibrated to the correct temperature, the center locations of the bull's-eyes were identified and memorized and the stage was focused to the Hoechst 33342 stained nuclei. The distance in the z-direction between average bright-field, IFIT2 reporter (GFP), and Hoechst was memorized and the stage height adjusted before each individual image. It was assumed that the virus reporter (RFP) would have a very similar focus point to the GFP. Images were taken in a 4 x 3 array around the center of each bull's-eye in the following order: bright-field (5ms exposure), blue channel (15ms exposure), red channel (2000ms exposure) and green channel (20000ms exposure) using a Sedat quad filter cube. Imaging the entire array required approximately 18 minutes, and was looped at a 30 minute interval for about 28 hours beginning 2.58 hpi.

3.2.6 Image processing workflow and data analysis

Image organization and processing was done in JEX as described in Section 1.2.3.2. Briefly, the images were sorted according to location, time, and color and then registered to correct for any small shifts in the device location. For this work, registration was done based on the phase contrast images. Following registration, the first red channel image (taken before any detectable

signal from cells) was convolved using a kernel to identify microwell locations, and then a function was run to locate and number the microwell locations based on the convolution. The maxima in the blue channel (# of nuclei) were located and the number in each microwell determined. Finally, a cell radius was chosen (11 pixels) and measurements were taken in each fluorescent color at all times (method for determining correct radius are included in Section 2.2.7.1). The measurement and cell count data tables are exported and analyzed in Matlab.

The code used to analyze the microwell data can be found on the Yin lab's shared server in Past Group Members\Andrea\MatlabCode\Chapter3. In order to perform the analysis in Matlab, the ARFF files exported by JEX must be converted into a format readable by Matlab. This is done with the Matlab Weka Interface. The sequence for processing this data is identical to sequence described in Chapter 2.

3.3 Results

Interferons trigger massive signaling cascades involving hundreds of genes (García-Sastre 2006). Vesicular stomatitis virus growth has been shown many times to be inhibited in cells capable of a robust anti-viral response, specifically by an interferon mediate response (Trottier 2005; Carey 2008). In fact, a significant amount of work has been done studying how specific type-I interferon stimulated genes, or ISGs, affect VSV replication, including at the stages of endocytosis, transcription, translation, and virion release (Staeheli 1991; Schwemmle 1995; Trottier 2005; Weidner 2010; Fensterl 2012; Liu 2012). One ISG that is specifically known to act on VSV replication is IFIT2. We have previously shown that there is a relationship between the timing of IFIT2 induction and virus replication and that this relationship affects virus production in VSV-resistant PC3 cells (Chapter 2). The following results demonstrate how IFN-β pre-treatments affect IFIT2 reporter kinetics and overall virus replication.

3.3.1 IFN-β pre-treated and un-treated one-step infections

PC3-IFIT2 reporter cells were infected with either the N1-DSRed or M51R-DSRed strains of VSV using a multiplicity of infection (MOI) high enough to obtain a synchronous infection (Effective MOI ~ 15). Six hours before infection, cell monolayers were either pre-treated with IFN-β (~200 units/well) or mock treated. Infectious virus production was determined at multiple time points and plotted together with viral protein production (RFP) (Figure 3.3-1). The viral RFP signal was measured on the Typhoon FLA 9000. This instrument is ideal for measuring large areas, but lacks the sensitivity of a fluorescent microscope, explaining why we cannot detect early RFP production in the IFN pre-treated condition, M51R infected cells. However, by comparing the RFP and PFU measurements of the four conditions we do observe that there is fidelity of relative time delays, production rates, and yields between the virus reporter signal and the virus particle production at the various conditions. The two measurements also spanned similar scales. Although we do not show a direct correlation here, these results indicate that the virus reporter protein is a reasonable indicator of the infection state in cells.

When comparing the one-step virus production kinetics, we found that the anti-viral state created with IFN-β pre-treatments reduced the yields of both N1-DSRed and M51R-DSRed. The six-hour IFN-β pre-treatment caused yields of N1-DSRed to decrease 3.4-fold, even though this strain is able to block nuclear export of cellular mRNA, and in general, shut down the immune response of the host. The decrease in M51R yields with IFN-β pre-treatments was greater than the decrease in N1-DSRed yields (~4.9-fold). The larger decrease is likely owing to the mutated matrix protein in M51R that cannot block mRNA export. Notably, these M51R infected cells still produced over 1000 PFU per cell after IFN-β pre-treatments.

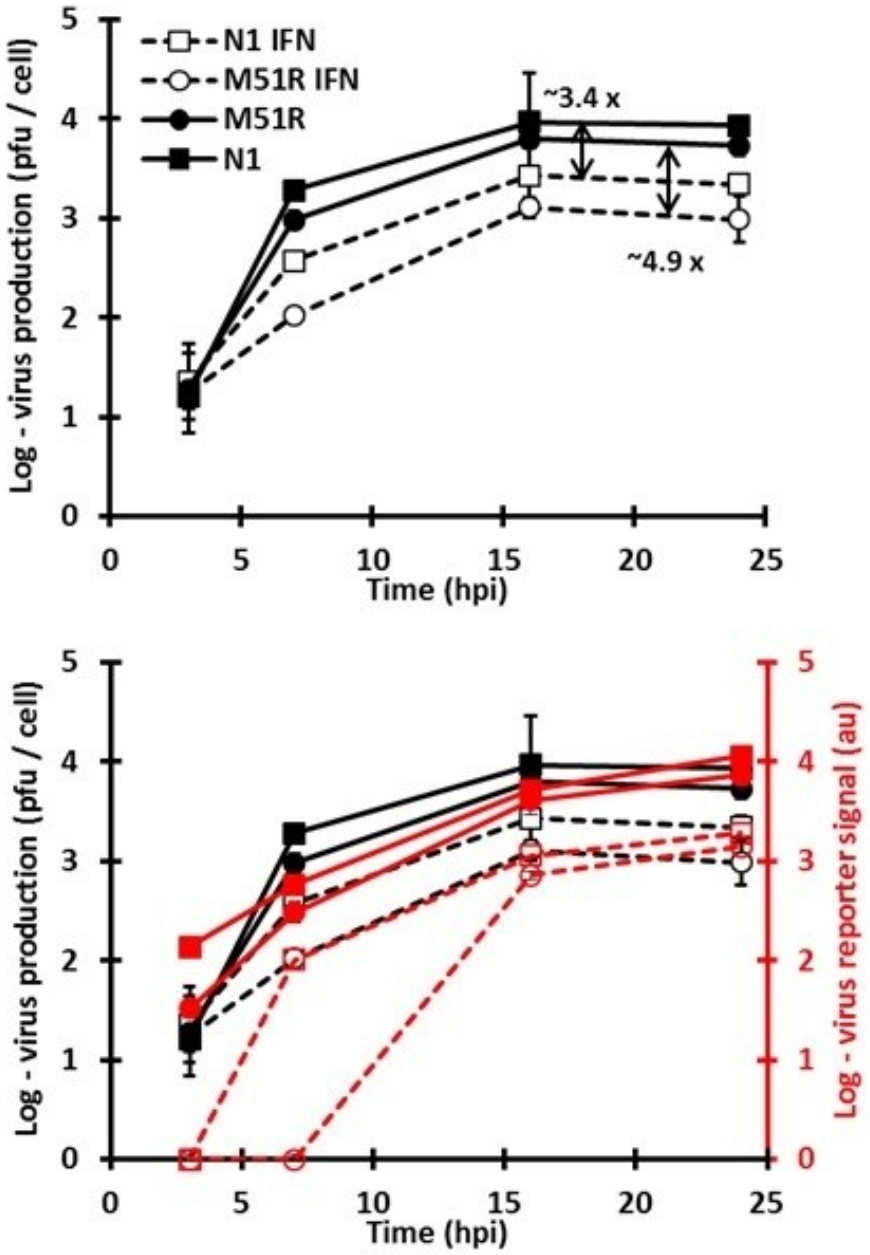

Figure 3.3-1: IFN pre-treated and un-treated N1-VSV and M51R-VSV one-step infections. (top) IFN pre-treatments have a protective effect against both, but the decrease in viral yields is larger with M51R infections (4.9-fold decrease vs. 3.4-fold decrease). (bottom) Viral reporter expression kinetics determined with Typhoon imaging. While the Typhoon scanner is not as sensitive as a fluorescent microscope, we are able to determine that the relative RFP trajectories have fidelity of relative time delays, relative production rates, and relative yields for all 4 conditions compared to virus production.

3.3.2 Mechanisms for IFIT2 activation

We are aware of two mechanisms for transcriptional activation of the IFIT2 gene. Simplified versions of these two mechanisms are shown in Figure 3.3-2. The first mechanism, shown on the left side of Figure 3.3-2 depends on the detection of a viral infection. In this case, VSV infection is likely detected by a cytoplasmic sensor such as RIG-I, leading to phosphorylation of IRF-3, which then binds to the interferon-sensitive response element (ISRE) of IFIT2 and also binds the positive regulatory domain (PRD) of IFN-β (Sen G.C. 2007). In our reporter cells, activated IRF-3 would, therefore, also lead directly to transcription of the ZSGreen gene. The second mechanism, pictured on the right side of Figure 3.3-2, requires activation of the Jak/Stat pathway through binding of type-I IFNs to their receptor. In the context of cell culture experiments, this activation can occur in three ways: first, through binding of exogenous IFN-β to the type-I interferon receptor; second, through autocrine IFN-β signaling instigated by detection of virus by RIG-I leading to phosphorylation of IRF-7 (Kato 2006); or third, through paracrine signaling of IFN-β secreting cells to neighboring cells (Rand 2012). Once the type-I interferon receptor is bound, activation of the Jak/Stat pathway leads to transcriptional activation of IFIT2 and ZSGreen.

IFIT2 gene expression levels may vary depending on the mode of transcriptional activation. We measured the fold-increase over mock of IFIT2 mRNA production when our PC3-IFIT2 reporter cells are stimulated with high doses of IFN-β (~1000 units/well) or infected at a high MOI with M51R-DSRed. The IFN-β and IFIT2 mRNA production kinetics, after stimulation with IFN-β or M51R infection, are shown in Figure 3.3-3. Virus infection resulted in large fold-changes in both IFN-β and IFIT2 transcripts, and fold-increases for both species of ~25 were detected as early as 3 hours after infection. Imaging of the infected PC3-IFIT2 cells showed that

the expression of the IFIT2 reporter gene was also detected at high levels several hours post infection (Figure 3.3-3 a. right). Treatment of cells with a high dose of IFN-β did not result in similar levels of IFIT2 and IFN-β induction. After IFN-β stimulation, IFIT2 transcripts increased a much more modest 7-fold over mock, while IFN-β transcripts did not appear to increase at all. ZSGreen expression in PC3-IFIT2 cells was barely detectable after IFN-β treatment. IFN-β does not appear to lead to autocrine signaling without the contribution of other factors, such as detection of virus. Others in our lab have observed this behavior as well. It is likely a method of regulation to control the anti-viral signaling system.

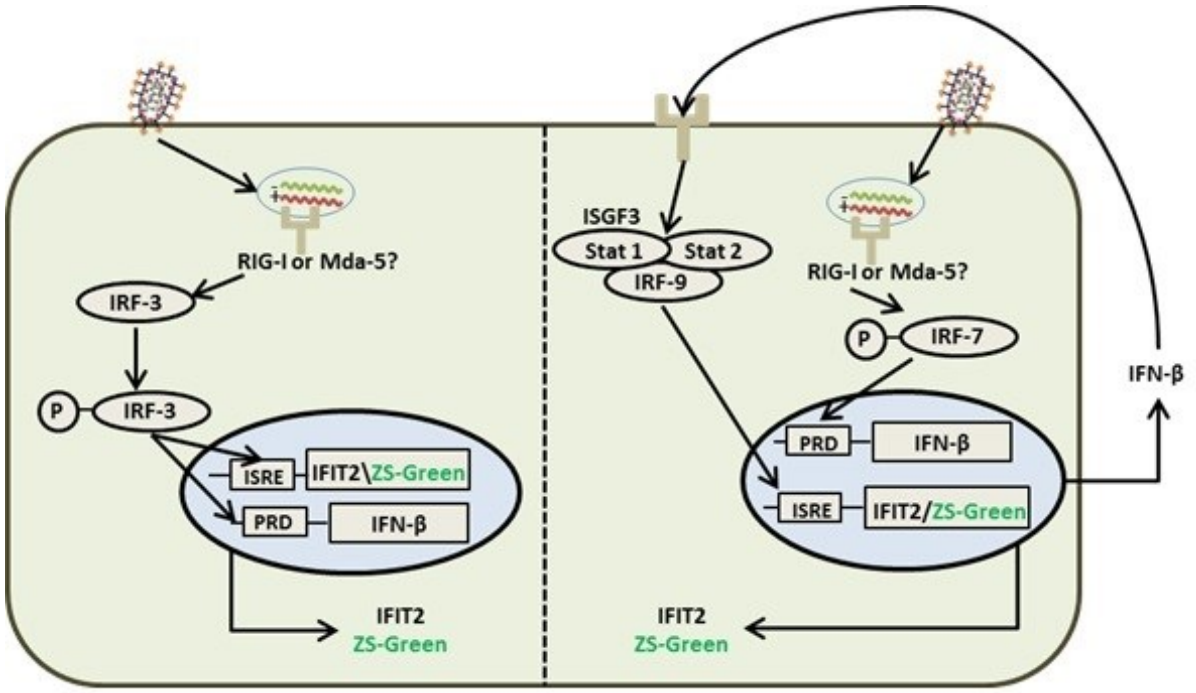

Figure 3.3-2: Simplified diagram of two mechanisms for IFIT2 transcriptional activation. (left) VSV is detected, likely by RIG-I, leading to phosphorylation of IRF-3, which binds to the ISRE of IFIT2 and causes transcription. In our reporter cells, ZSGreen transcription is also activated. (right) VSV detection leads to secretion of IFN-β and subsequent autocrine signaling leads to activation of the Jak/Stat pathway (addition of exogenous IFN-β can also activate this pathway) and transcriptional activation of both IFIT2 and ZSGreen.

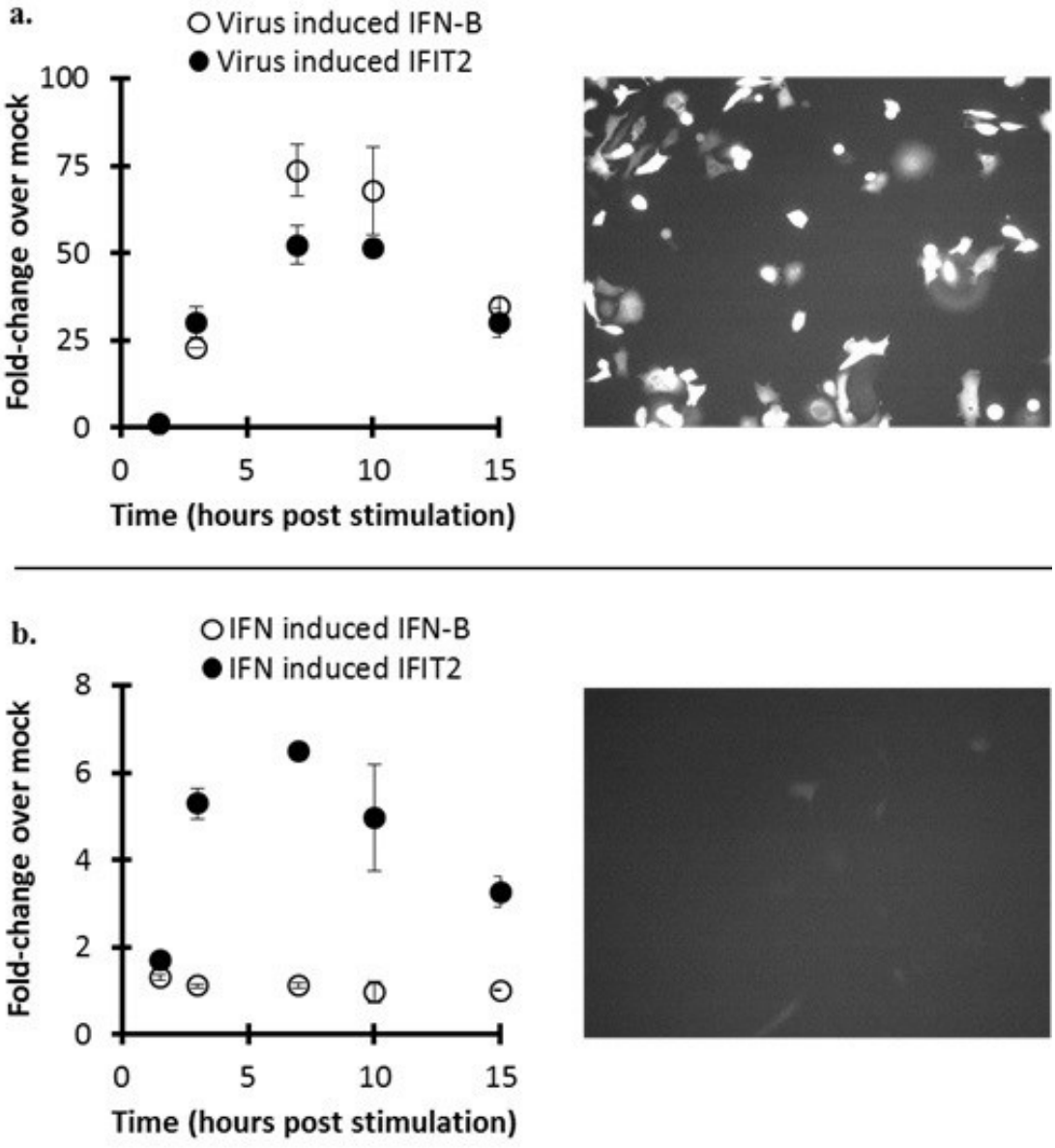

Figure 3.3-3: IFN-β and IFIT2 mRNA production kinetics after stimulation with either IFN-β or infection with virus. The images to the right of the plots are PC3-IFIT2 cells expressing the ZSGreen after stimulation with either virus or IFN-β. The images are representative of each condition and are at similar cell densities and were taken ~7 hours post stimulation.

3.3.3 Effects of IFN-β pre-treatments on the relative detection of IFIT2 and viral reporters in M51R infected cells

Cell monolayers were either mock-treated 3 hours before infection or treated with 200 units/ml IFN-β 6 hours or 3 hours before the monolayers were trypsinized and infected in-solution. The infected cells were seeded into microwells and imaged over time. Figure 3.3-4 shows the percentages of the total 'single-cell' population that were positive for either the virus or IFIT2 reporter or positive for both reporters at some point during imaging. The relative proportions of RFP+, GFP+, and RFP+GFP+ cells in the mock treated population were similar to what we have seen previously (Chapter 2) and are similar to monolayer culture (Swick n.d.). There is not much difference between the 3-hour pre-treatment results and the mock-treated results, but we did observe an increase in RFP-GFP+ cells. After 6-hours pre-treatment, the signaling trends changed and more cells were GFP+ than were positive for both the IFIT2 reporter and the virus reporter. Notably, the total percentage of RFP-GFP+ cells and RFP+GFP- cells decreased with 3-hours IFN-β pre-treatment and decreased further with 6-hour IFN-β pre-treatment (Figure 3.3-4 right panel). The IFN-β pre-treatments are affecting the number of detectable infections, but perhaps not because of IFN-induced IFIT2 expression.

To investigate the relationship between the virus and IFIT2 reporters in depth, we have defined several parameters to characterize the reporter kinetics. The parameters of delay-time, production rate, rise-time, and maximum intensity were also described in Chapter 2. The delay-time is defined as the first time at which the reporter signal crosses a limit of detection (the LOD is calculated based on the empty well signal at both wavelengths). The production rate is an

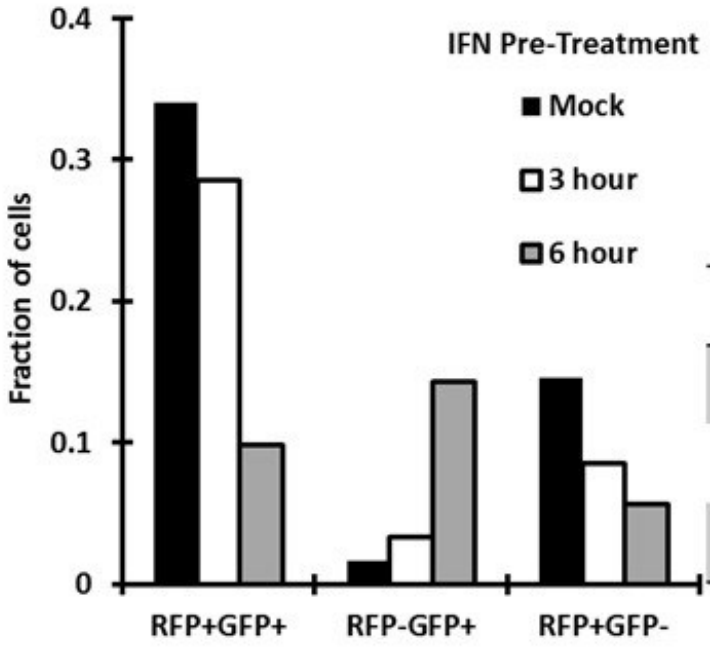

Pre-Treatment	RFP+	GFP+
Mock	49%	36%
3 hour	37%	32%
6 hour	16%	24%

Figure 3.3-4: Fraction of total single-cell population that are positive for either the virus reporter protein, the IFIT2 reporter, or positive for both reporters. The table or the right indicates the percentages of cells expressing a signal that are RFP or GFP positive under the three IFN-β pre-treatment conditions.

approximation of the maximum rate of reporter expression and is based on an exponential fit (Equation 3.3-1) of the first 4 time-points above the LOD. We use the parameters, α, as an approximate production rate.

Equation 3.3-1

$$Intensity = A \cdot \exp(\alpha \cdot time)$$

The maximum intensity is simply the highest measurement taken from a single-cell, and finally, the rise-time is the period between the delay-time and the time at which 85% of the maximum intensity is reached. This time represents the majority of the reporter production time for a given cell.

We have previously demonstrated that these parameters are useful for characterizing the kinetics of our viral and cellular reporter proteins. We have shown that the relative delays to detection of the IFIT2 and virus reporter are important to the outcome of the infection (Chapter 2). In our previous experiments, we found that IFIT2 reporter detection usually followed detection of the virus reporter by 2 hours. In this work we found that the median delay-times for the IFIT2 and virus reporters in RFP+GFP+ cells in the mock-treated population are 8.1 and 6.1 hpi, respectively – also a 2 hour difference. We hoped to perturb this relationship by pre-treating the cells with IFN-β, and we do observe a decrease in the difference between median delay-times. When PC3-IFIT2 cells are pre-treated with IFN-β for 3 hours the virus reporter only has a 1 hour advantage in median times (6.6 hpi vs. 7.6 hpi) and when cells are pre-treated with IFN-β for 6 hours, the median delay-times for both reporters are 9.6 hpi (Table 3.3-1, Table 3.3-2). The perturbation of the delay-times with IFN-β appears to increase the delay-time to detection of the virus reporter rather than speed up detection of the IFIT2 reporter. Distributions of both the viral and IFIT2 delay-times are shown in the first two rows of Figure 3.3-5 and both the mean and median delay-times at each condition are summarized in Table 3.3-1 and Table 3.3-2. The histograms in Figure 3.3-5 show that the delay-time distributions are broad and become broader with longer IFN-β pre-treatments. The bottom row of Figure 3.3-5 are comparison plots of the IFIT2 and virus reporter delay-times for each isolated cell at each pre-treatment condition, and clearly show a shift in the relative detection times.

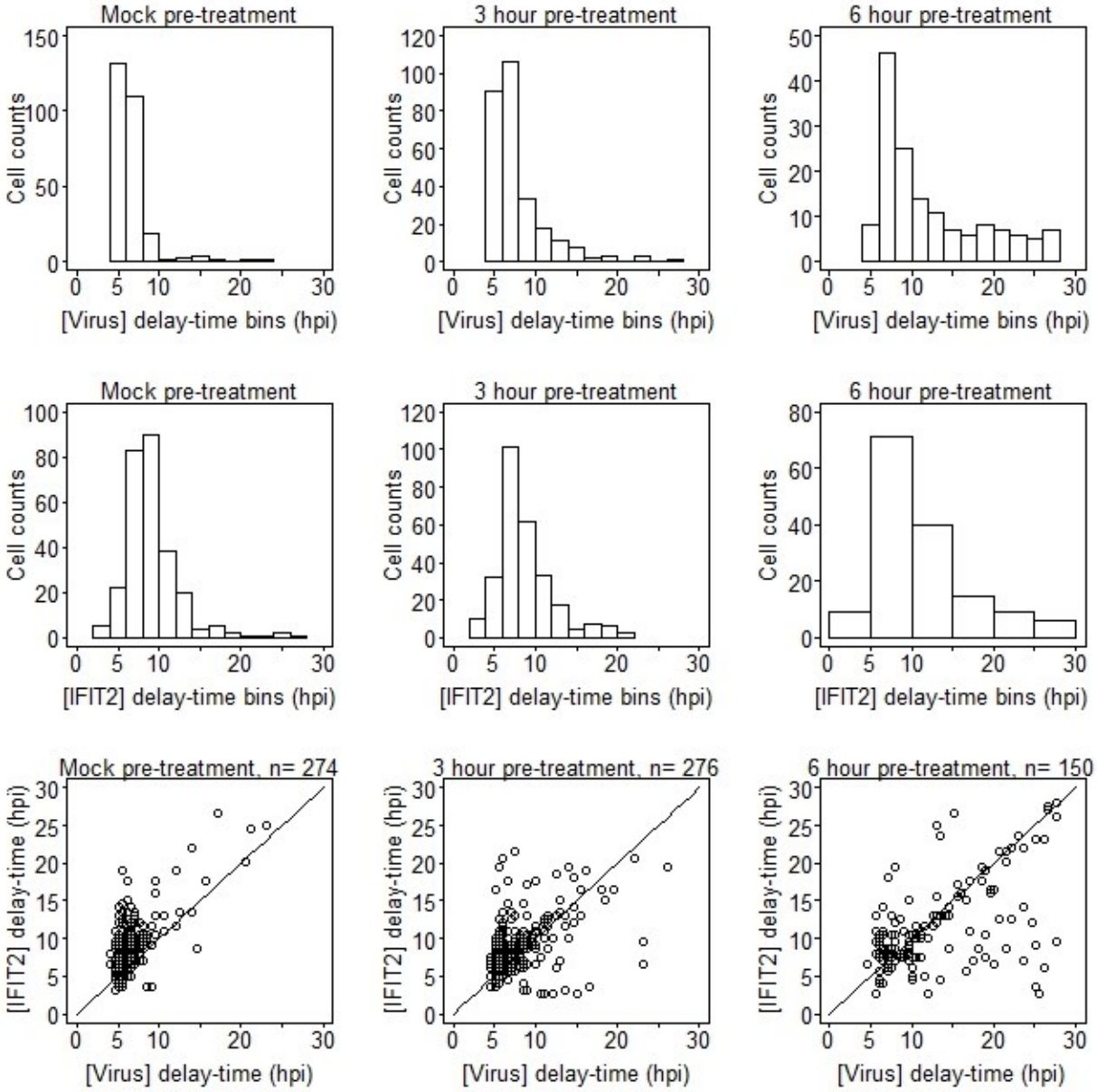

Figure 3.3-5: Delay-time distributions and relative delay-times for single-cell populations at the three IFN-β pre-treatment conditions. (top) Virus reporter delay-time histograms (middle) IFIT2 reporter delay-time histograms (bottom) Comparison plots of the virus and IFIT2 reporter protein delay-times from individual cells for (a.) mock, (b.) 3 hour, and (c.) 6 hour pre-treatments.

3.3.4 IFN-β pre-treatments significantly affect all viral reporter kinetics parameters

Our delay-time results indicate that the perturbation of the relative detections of the IFIT2 and virus reporters with IFN-β is caused by longer virus reporter delay-times, rather than shorter IFIT2 delay-times. The IFN-β pre-treatments affected all viral kinetic parameters significantly. We have prepared boxplots for the rise-time, production rate (alpha), and maximum intensity parameters of the viral RFP (Figure 3.3-6), and in general we found that at longer IFN-β pre-treatment times, the rise-times became much shorter, the production rates decreased, and the maximum intensities dropped. The means and medians of the RFP+GFP+ population are summarized in Table 3.3-1 (top). There was no significant difference between the production rates at the mock and 3 hour pre-treatment conditions ($p=0.79$), but every other pair of parameters did test as significant using the Mann-Whitney test (all p-values < 0.05).

We have previously shown that the maximum intensities are often correlated with the production rate, the rise-time, and the product of these two parameters (Chapter 2). The changes in these parameter distributions that occur as IFN-β pre-treatment times increase may suggest at what point in the virus replication cycle VSV is being targeted with ISGs. For example, the rise-time parameter characterizes the length of time viral protein is produced and can be shortened due to premature cell death. Some ISGs, including IFIT2, are known to be related to apoptosis (Stawowczyk 2011; Reich 2013). To determine if or how lysis, which is easily detectable in microwells, affects the reporter kinetics, we have divided the data into intact and lysed populations. The rise-times are shorter in the lysed population compared to the intact population at each pre-treatment condition (Mock: 11.1 h → 8.0 h, 3-hour: 9.0 h → 6.9 h), and are statistically different at the mock ($p = 0.00$) and 3-hour conditions ($p=0.00$). We did not perform significance tests on the 6-hour populations due to the small sample size of lysed cells. The

delay-times from mock treated cells were significantly lower in lysed compared to intact cells ($p = 0.01$). Also, the production rate at 3-hours pre-treatment was significantly higher in lysed cells than in intact cells ($p = 0.02$).

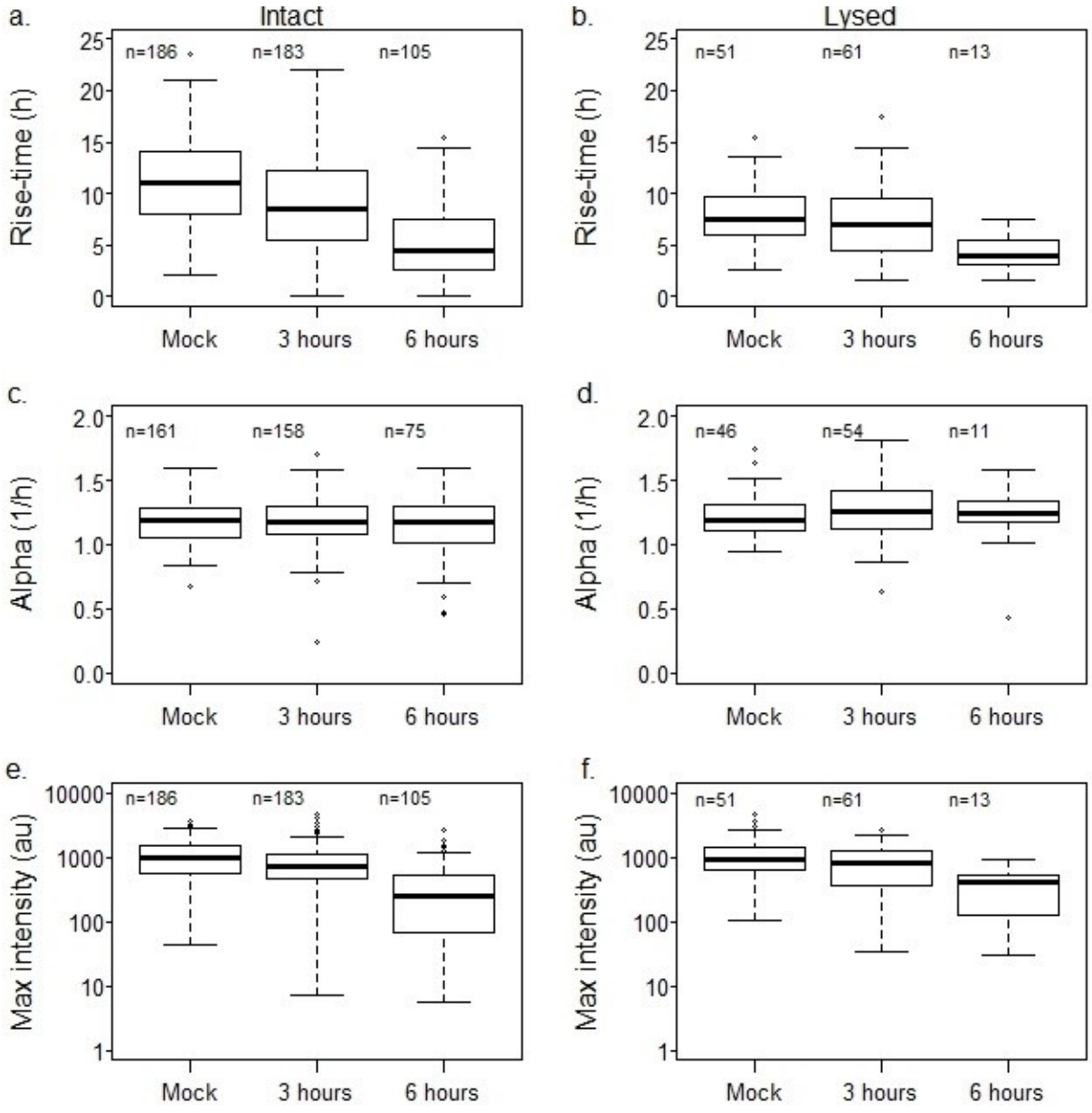

Figure 3.3-6: Boxplots of the virus delay-time, production rate, and max-intensity parameters. The plots on the left represent the population of cells that appeared to remain intact, and the plots on the right represent the population of cells that appeared to lyse during imaging.

One of the more interesting results of our previous work (Chapter 2) was the finding that RFP+, but GFP- cells had lower average maximum intensities and also lower production rates. To determine if this result was repeatable, we have analyzed the kinetic parameters of the RFP+GFP- population. The means and medians of these parameters are included in Table 3.3-1.

Table 3.3-1: Virus kinetic parameters for cells that are RFP+GFP+ (top) and cells that are RFP+GFP- (bottom). In both cases delay-times are longer when cells are pre-treated with IFN-β. In all cases delay-times are longer, reporter production is slower, rise-times are shorter, and yields are lower in cells that are GFP-.

RFP+GFP+ R parameters: n=700

IFN Pre-treatment Condition	Time Delay (hpi)	Alpha (1/h)	Rise Time (h)	Max Intensity (au)
Mock	6.5 / 6.1	1.20 / 1.21	10.5 / 10.5	1108 / 950
3 hours	7.7 / 6.6	1.20 / 1.19	8.5 / 8.0	895 / 728
6 hours	12.1 / 9.6	1.12 / 1.16	5.0 / 4.3	394 / 265

RFP+GFP- R parameters: n=286

IFN Pre-treatment Condition	Time Delay (hpi)	Alpha (1/h)	Rise Time (h)	Max Intensity (au)
Mock	7.8 / 6.1	1.15 / 1.15	9.0 / 8.5	696 / 558
3 hours	9.3 / 7.6	1.16 / 1.18	8.1 / 8.0	616 / 453
6 hours	12.8 / 9.6	1.10 / 1.10	5.4 / 4.0	412 / 180

The experimental conditions of the mock pre-treatment case and the work in Chapter 2 were nearly identical, and the results of these experiments are very similar. In the mock pre-treatment population, both the average production rate and average maximum yield were lower in cells that did not produce a detectable level of the cellular GFP compared to the population that did produce detectable GFP. The average viral reporter production rates and maximum yields were also lower in the GFP- population of 3-hour pre-treated cells. There was no statistical difference between the 6 hour GFP+ and GFP- populations.

3.3.5 IFIT2 kinetic parameter distributions in lysed and intact cells

The qPCR results (Figure 3.3-3) and the delay-time results (Figure 3.3-5) show that transcriptional activation of the IFIT2 reporter occurs primarily as a response to detection of virus. In comparison, IFN-β pre-treatments are a fairly weak inducer of the IFIT2 transcription. It is important to note that we have observed no correlations between the rates and magnitudes of IFIT2 induction and the virus reporter parameters, other than delay-time (Chapter 2). The same was true of the parameters extracted from this data set (results not shown). While our results indicated that IFIT2 reporter production does not continue to respond to viral infection after initial activation, we did observe very clear correlations between the relative delay-time to detection of the two reporters and either IFIT2 or viral reporter maximum intensities (Chapter 2). Continuing with our analysis of the IFIT2 parameters, we have prepared boxplots of the rise-time, production rate, and max intensity parameters for the intact and lysed cell populations (Figure 3.3-7). Unlike the viral reporter parameter distributions, there are no clear trends observed in the same IFIT2 reporter parameters. Rise-times do decrease at long IFN-β pre-treatment times, perhaps due to increases in the rates of cell lysis as we discussed in Section 3.3.4. The only statistically significant difference between the lysed and intact parameters is in

the 3-hour pre-treatment delay-times (Mann-Whitney, p-0.003). The means and medians of all the IFIT2 kinetic parameters are summarized in Table 3.3-2. We have not included information

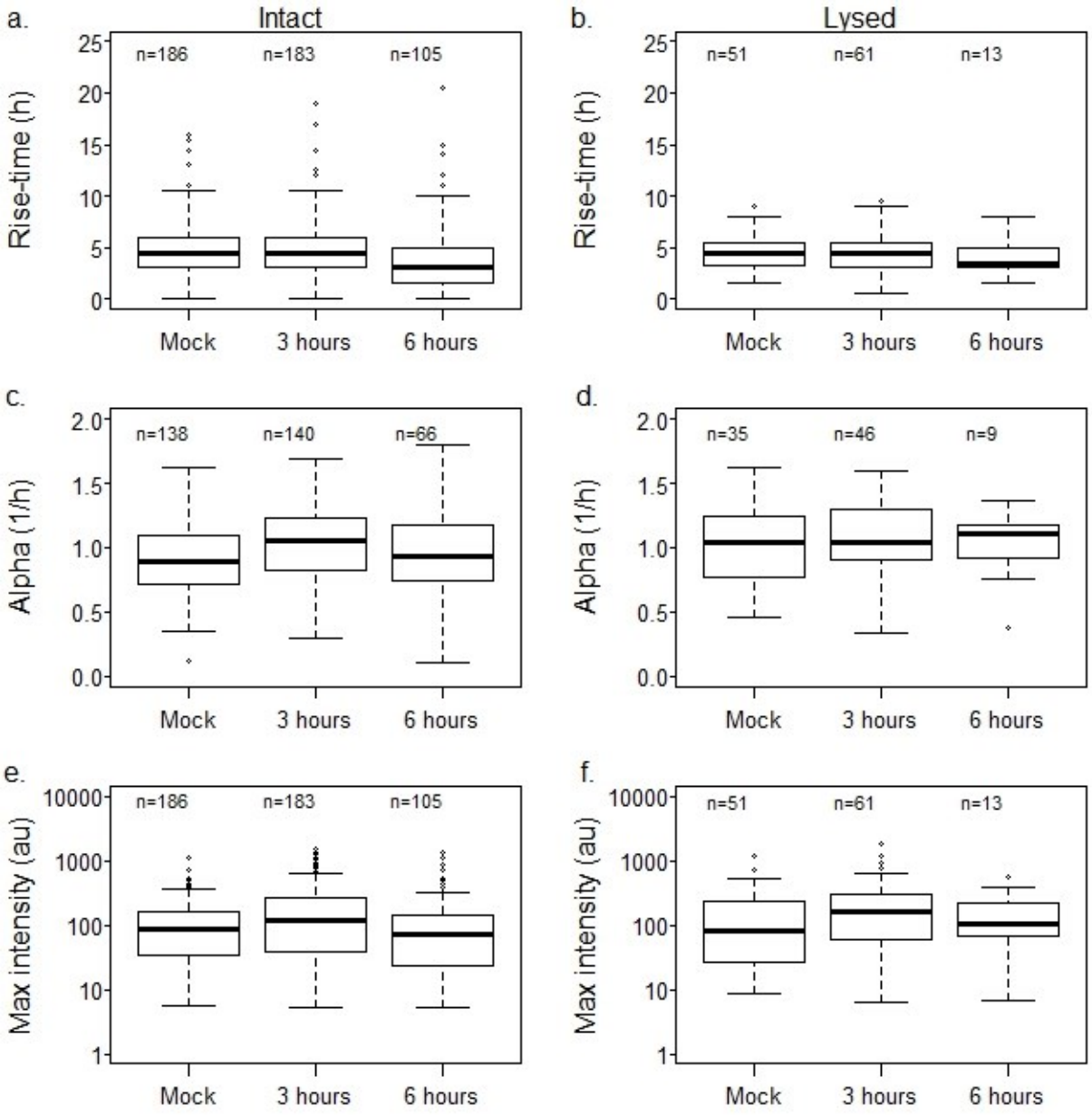

Figure 3.3-7: Boxplots of the IFIT2 delay-time, production rate, and max-intensity parameters. The plots on the left represent the population of cells that appeared to remain intact, and the plots on the right represent the population of cells that appeared to lyse during imaging.

regarding the RFP-GFP+ population because there was not a large enough sample size to obtain statistically relevant results.

Table 3.3-2: IFIT2 kinetic parameters for cells that are RFP+GFP+.

IFN Pre-treatment Condition	Time Delay (hpi)	Alpha (1/h)	Rise Time (h)	Max Intensity (au)
Mock	8.9 / 8.1	0.92 / 0.91	4.9 / 4.5	136 / 85
3 hours	8.6 / 7.6	1.04 / 1.06	4.8 / 4.5	231 / 127
6 hours	11.1 / 9.6	0.95 / 0.97	4.0 / 3.5	144 / 73

3.3.6 IFN-β pre-treatments shift advantage toward the host-cell in high-multiplicity infections

As the duration of IFN-β pre-treatments increase, we find that the relative delay-times of the IFIT2 reporter and the viral reporter shift closer together. The median delay-times of the two reporters are actually equal after 6 hours of IFN-β exposure (Figure 3.3-5). The results in Figure 3.3-8 show how this shift in delay-times affects the maximum virus reporter intensity (left) and maximum IFIT2 reporter intensity (right). We have plotted either the maximum intensity of the virus or IFIT2 reporter against the difference in delay-times ([IFIT2] delay-time – [Virus] delay-time). The data included in these plots is limited to the PC3-IFIT2 cells that expressed detectable levels of both the virus and IFIT2 reporters. There are two inset, example plots representing the relative timing of the virus and IFIT2 kinetics. All points to the left of the dashed line on all plots represent cells expressing detectable levels of IFIT2 reporter protein before the virus reporter protein, similar to the inset plot on the left. All points to the right of the dashed line represent

cells that expressed detectable levels of the virus reporter before the IFIT2 reporter. We see two shifts in the viral max intensities as the duration of the IFN-β pre-treatment increases. First, the virus reporter intensities decrease at longer pre-treatment times, implying less virus production from cells treated with IFN-β, suggesting an innate immune response is limiting virus reporter production. Second, more cells begin to express the IFIT2 reporter before the virus reporter protein at longer pre-treatment times. At mock pre-treatment conditions less than 8% of cells appear to produce the IFIT2 reporter before the virus reporter, while we detect the viral reporter first in ~ 87% of cells. When infecting after 3-hours of IFN-β exposure, those percentages shift and we detect the cellular GFP first in 26% of cells and the viral RFP first in 64% of cells. After pre-treating cells with IFN-β for 6-hours before infecting, there appears to be a critical shift and the IFIT2 reporter is detected first in the more cells than the viral reporter (GFP first: 47%, RFP first: 43%).

The trends in the IFIT2 reporter maximums are different and perhaps more complex. The average IFIT2 signal increases with a 3 hours pre-treatment, but then decreases at the longer 6 hour IFN-β pre-treatment. At every condition, we observe a limitation on the amount of IFIT2 reporter that may be produced when the viral reporter is detected before the IFIT2 reporter. Our results indicate that IFN-β pre-treatments delay viral reporter protein production compared to the control case, but have little effect on the IFIT2 reporter kinetics. IFN-β treatments potentially activate hundreds of ISGs that have any number of effects on virus replication. The following sections include preliminary results that suggest the mechanism of interference in virus replication in our individual cell trajectories.

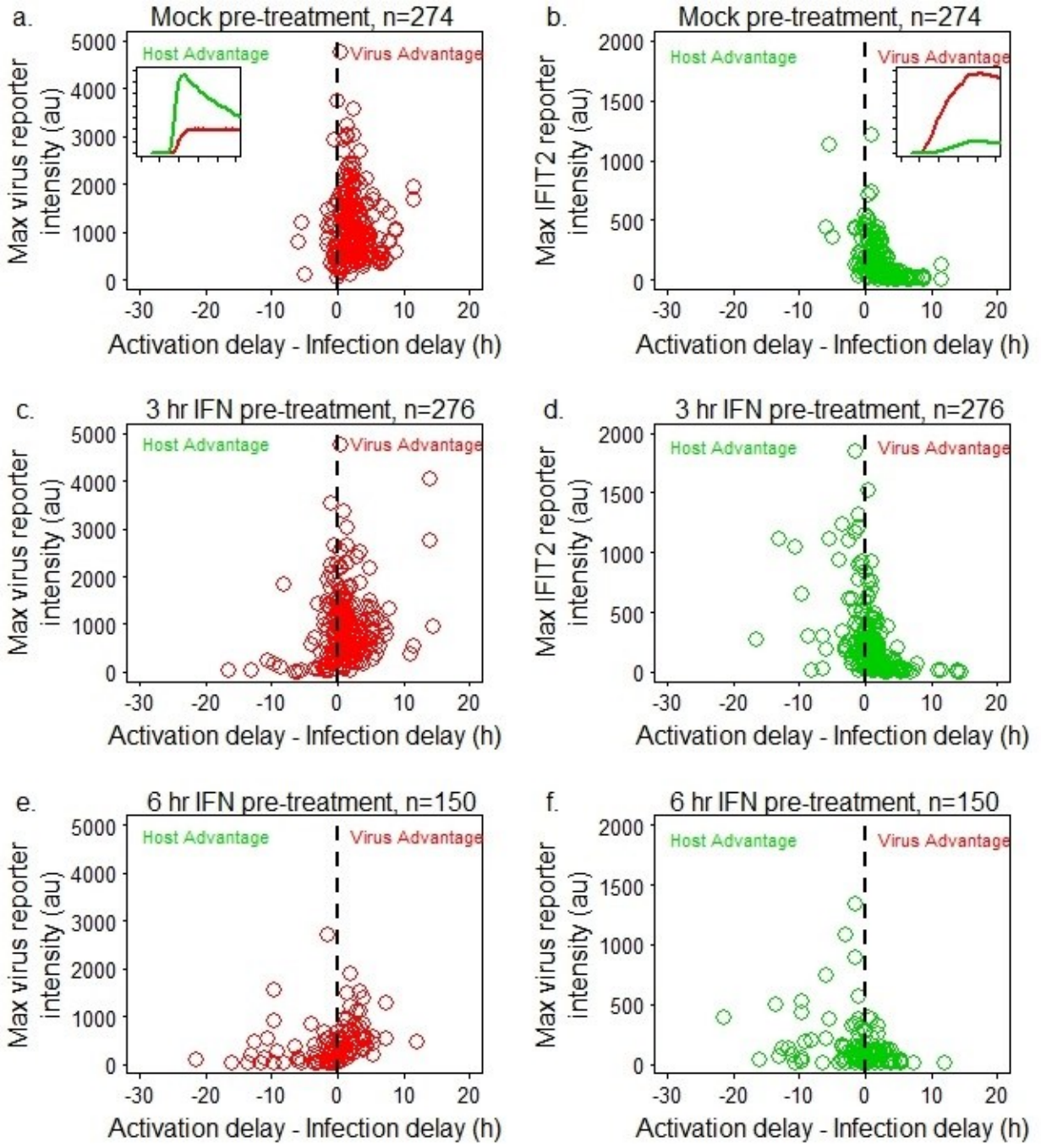

Figure 3.3-8: Maximum virus or IFIT2 reporter intensities plotted against the relative first detection times of these two reporter proteins. (a, c, e) Maximum virus reporter intensities plotted against the relative detection times with increasing IFN-β pre-treatment durations. (b, d, f) Maximum IFIT2 reporter intensities plotted against the relative detection times with increasing IFN-β duration times. In all plots the data to the left of the dashed line represents isolated single-cells in which the IFIT2 reporter was detected before the viral reporter. All points to the right of the dashed line represent isolated single-cells in which the viral reporter was detected before the viral reporter.

3.3.7 Potential mechanisms of ISG inhibition of virus replication

Much work has been done to investigate how the hundreds of ISGs may interact with different viral species. This work is complicated by the large number of ISGs coupled with the fact that gene expression can vary based on cell type and other factors. We have taken a few simple steps to explore how VSV protein production is affected by IFN-β pre-treatments. Our high-throughput single-cell methods provide us with a unique platform with which to perform these analyses.

The single-cell viral RFP trajectories show that delay-times increase with longer IFN-β pre-treatment durations. In PC3 cells, VSV often becomes trapped in endosomes and incapable of replication. It is unclear by what mechanism VSV becomes trapped, but certain ISGs are capable of preventing viral envelope fusion (Weidner 2010; Liu 2013). Other ISGs target endocytosis (Whitaker-Dowling 1983; Bukholm 1990). After infection, certain ISGs are known to degrade viral mRNA (Atasheva 2012), and still others suppress translation (Perwitasari 2011) and or inhibit release of viral particles (Weidner 2010). Our delay-time measurements lump together the time required to perform several early virus replication processes, including endocytosis, fusion, primary transcription, and translation. Some amount of translation needs to occur for the mature RFP protein to accumulate enough for detection. The rate of protein production is one small part of this process, but can determine how important this rate is in determining the detection time by plotting the delay-times against the viral production rates. In Figure 3.3-9 we have plotted viral reporter delay-times against production rates for each of the IFN-β pre-treatment conditions. These results show that some cells appear to have slower production rates and longer delay-times, but as a whole, the correlation is very weak.

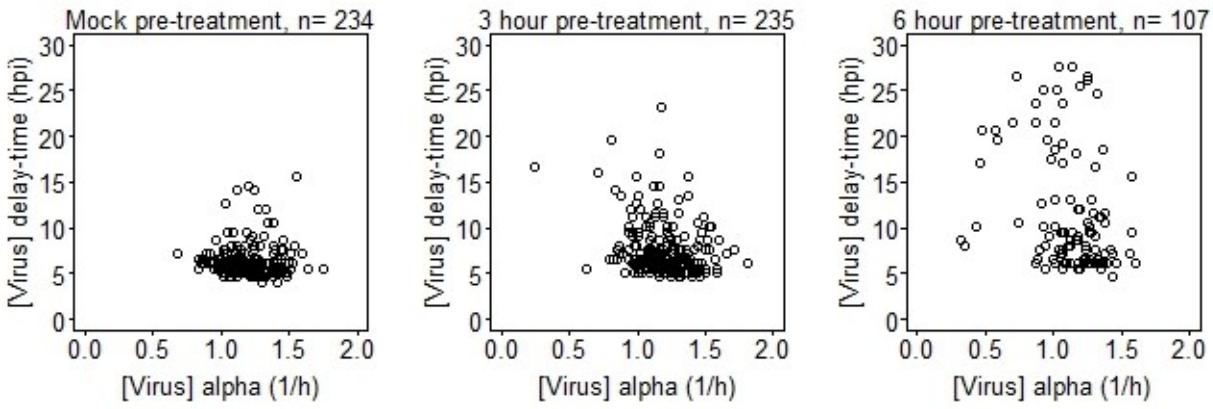

Figure 3.3-9: Single-cell viral reporter delay-times plotting against the viral reporter production rates at each IFN-β pre-treatment condition.

IFN-β also stimulates activation of some ISGs that are pro-apoptotic. Cell death can be a defense mechanism to limit virus production. We are able to easily detect such events in the microwells, and we observe apoptosis or lysis even more clearly at higher magnification, low-throughput experiments. PC3-IFIT2 cells or normal PC3 cells were infected in solution with N1-DSRed virus. Before infection some cells were exposed to IFN-β for either 3 or 6 hours. These cells were plated in multiple 96-well plates and one plate was chosen for imaging. The normalized per-cell virus production is plotted against the normalized maximum viral reporter signal for these cells in Figure 3.3-10. Similar to the parameter data shown in Sections 3.3.4 and 3.3.5, we have separated the cells that remained intact (filled circles) throughout imaging from those that appeared to lyse or apoptose (open circles). The normalized virus production was well correlated with the normalized RFP intensities with a Pearson correlation coefficient of 0.84. Three of the lysed cells produced less virus than we would have predicted based on the amount of viral RFP produced in these cells.

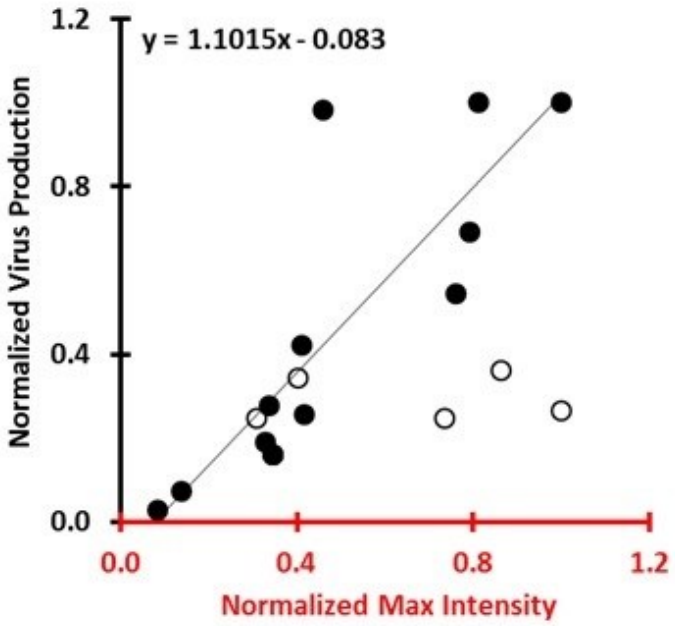

Figure 3.3-10: Normalized virus yield vs. normalized max intensity for 17 isolated cells. Filled circles represent cells that appeared to remain intact during imaging and open circles represent cells that appeared to lyse or apoptose during imaging.

In all, we were able to measure the amount of virus produced by 20 mock pre-treated, 19 cells pre-treated with IFN-β for 3-hours, and 21 cells pre-treated for 6-hours. The average yields for the cells producing detectable levels of virus dropped from 1719 PFU/cell at mock conditions to 897 PFU/cell and 440 PFU/cell at 3-hours and 6-hours of IFN-β pre-treatment, respectively. Compared to mock conditions, the percentage of cells that did not produce detectable virus output was 26% at 3 hours pre-treatment and 43% at 6 hours pre-treatment. Cells infected in solution at the 3 IFN-β pre-treatment conditions, were also plated at near population levels (7500 cells/well) in 96-well plates. The average population level yields taken from 2 wells at each condition were 2598, 815, and 278 PFU/cell at mock, 3-hours, and 6-hours pre-treatment, respectively.

Pre-treating PC3 cells with interferon before infection clearly results in an anti-viral state in cells. 3-hour pre-treatments lead to reductions in viral protein production and overall yields, but after 6-hours of interferon exposure, the protective effect is much stronger. There is evidence in this work and other work that the ISGs activated by interferons affect VSV replication at multiple stages. However, our delay-time results indicate that overall viral protein production is extremely sensitive to early events. We have chosen a few targets that were identified in Liu et al. as ISGs that likely have direct anti-viral effects that could cause the changes we observe in our viral reporter kinetics (Liu 2012). The first is IFITM3, which is an interferon induced transmembrane protein that has been shown to inhibit VSV production at a replication step after endocytosis, but prior to primary transcription in (Weidner 2010; Liu 2012). The second is cholesterol-25-hydroxylase (CH25H), which has been shown to broadly inhibit a variety of viral species including VSV by preventing fusion of the viral and cellular envelopes (Liu 2012; Liu 2013). The last target is PARP12, a member of the PARP superfamily that is not well characterized, but known to have anti-viral effects against alphaviruses in particular and also other viruses such as VSV, encephalomyocarditis virus, and Rift Valley fever virus (Atasheva 2012; Liu 2012). PARP12 has several structural similarities to PARP13, which inhibits virus growth by degrading viral RNA.

PC3-IFIT2 cells were stimulated with either a high multiplicity of M51R-DSRed or a high dose of IFN-β (1000 units/well – not removed). The mRNA kinetics were compared to a mock stimulation and the results are shown in Figure 3.3-11. Open circles represent the infected cells and filled circles represent the IFN-β stimulated cells. The results of the IFN-β and IFIT2 mRNA kinetic measurements from Section 3.3.2 are re-plotted here. The ISGs IFITM3 and PARP12 are up-regulated to a greater extent with IFN-β stimulation compared to virus infection, while

transcription of IFIT2 and CH25H mRNA is up-regulated primarily by the virus. We are not aware of any work that has shown these gene products to have direct anti-viral activity against VSV infections in PC3 cells, nor have we done the experiments to investigate any possible interaction; what we do see in the mRNA kinetics is that up-regulation of PARP12 and IFITM3 occurs on similar time-scales to both IFN-β and M51R stimulated IFIT2 production. PARP12 and IFIT2 both reach near maximum or maximum levels, by the 7-hour time-point. The magnitudes of the fold-changes for these two genes post IFN-β stimulation are similar, though the fold-change in IFIT2 production is much greater after virus infection. Notably, CH25H was only up-regulated after M51R infection and not after IFN-β stimulation. Several groups have observed that transcription of some ISGs and IFN-β itself cannot be activated only with addition of exogenous interferon, but require detection of a pathogen (Nakaya 2001; Ank 2006).

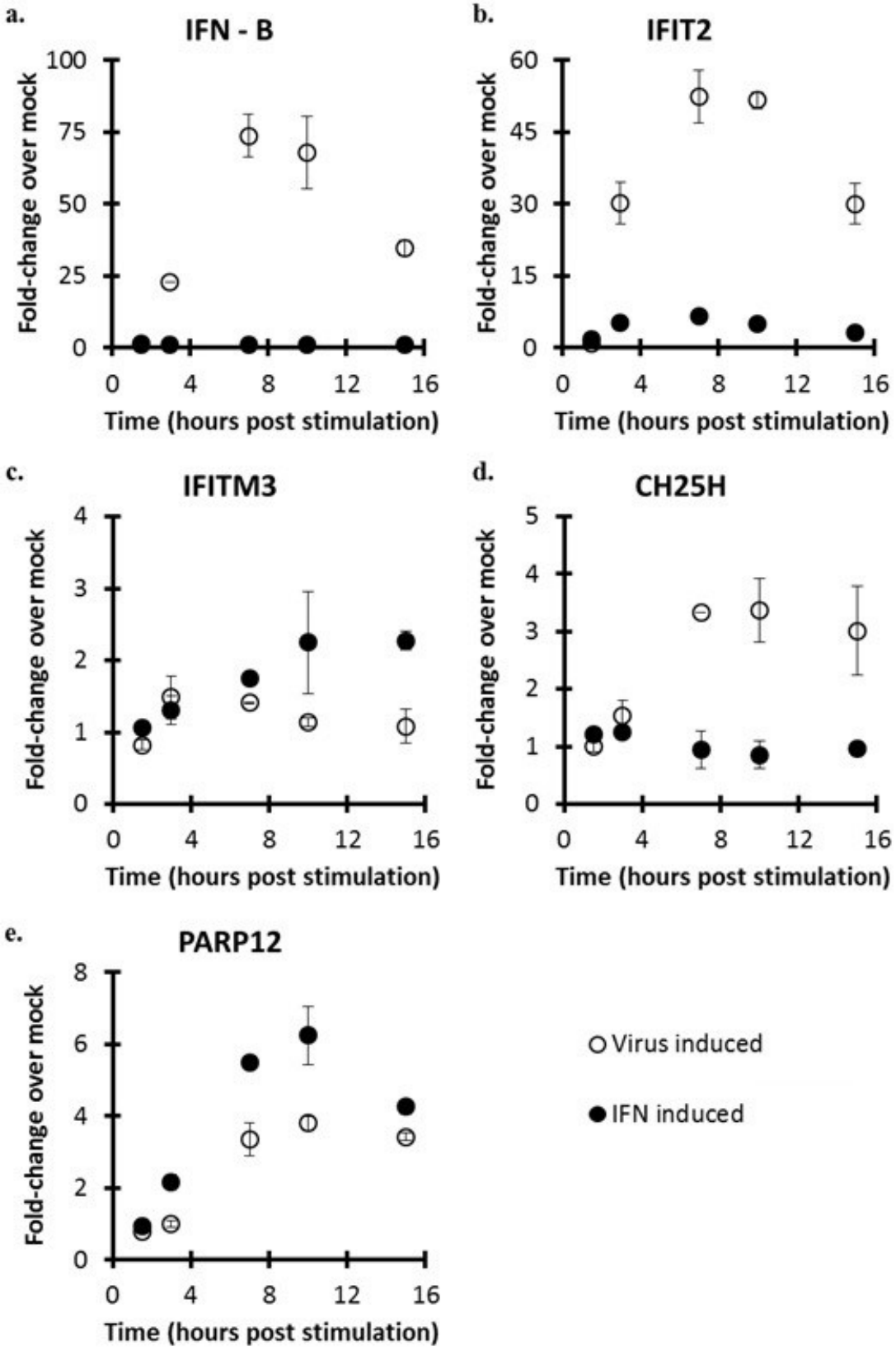
a.
IFN - B
Fold-change over mock
100
75
50
25
0
0
4
8
12
16
Time (hours post stimulation)
b.
IFIT2
Fold-change over mock
60
45
30
15
0
0
4
8
12
16
Time (hours post stimulation)
c.
IFITM3
Fold-change over mock
4
3
2
1
0
0
4
8
12
16
Time (hours post stimulation)
d.
CH25H
Fold-change over mock
5
4
3
2
1
0
0
4
8
12
16
Time (hours post stimulation)
e.
PARP12
Fold-change over mock
8
6
4
2
0
0
4
8
12
16
Time (hours post stimulation)
Virus induced
IFN induced

Figure 3.3-11: Transcriptional kinetics of IFN-β and various ISGs. Open circles represent the fold-change over mock after stimulation with M51R-DSRed infection and the closed circles represent the fold-change over mock after stimulation with IFN-β.

3.4 Discussion

The innate immune response to viral infection is the result of a complex mixture of redundant pathways designed to inhibit viral replication processes at every stage. The response to a viral infection is not uniform throughout an entire population of cells. There are many potential sources of variability including differences in gene expression, cellular resources, and ability of virus to suppress the innate immune response (Elowitz 2002; Levin 2011; Snijder 2011; Rand 2012). Local environmental factors such as degree of cell-cell contact also influence variability (Snijder 2009). The methods we developed reduce the effects of local environmental factors; however, the cells studied have a history from growing in a population. We still observe variability in cell size for example. Related work by our group explores spatial effects on the innate immune response in spreading infections (Swick, TBD).

The experiments presented here were performed using heterogeneous VSV and PC3-IFIT2 cell populations. We did not make any specific effort to reduce the heterogeneity other than using cold adsorption to synchronize the time of infection. We had previously found that there was a great deal of variability both in the kinetics of the viral RFP and cellular GFP production and that the early events controlling detection times were very important; we believe that the sub-population of cells producing the cellular GFP before the viral RFP may be important in controlling virus spread (Chapter 2). At this time, we only have indirect evidence that our reporters are proportional to the species they represent (viral protein, IFIT2 protein), but all results thus far indicate that they are accurately reporting on the state of infection and IFIT2

activation within a cell. Work is ongoing in the lab to measure protein levels using mass spectrometry, but this work is not complete. In order to verify our previous results and add further evidence supporting the accuracy of the reporter system, we aimed to perturb the system in a way that had predictable results. We added a new source of variability by pre-treating with IFN-β at different times before infection. IFN-β is known to inhibit VSV production and we verified this with population one-step infections with and without IFN-β pre-treatments (Figure 3.3-1). Although IFN-β is a weak inducer of IFIT2 production compared to M51R infection, we expected that IFN-β pre-treatments would still affect the relative detection times of the two reporters Figure 3.3-3. In fact we did observe a shift in the relative delay-times so that after 3 hours of IFN-β pre-treatment the time advantage of the virus was generally cut in half, and after 6 hours of IFN-β pre-treatments, we detected the IFIT2 reporter before the virus reporter in most cells.

This shift in relative delay-times is due principally to longer viral delays (Table 3.3-1 & Table 3.3-2). Several steps in the viral replication cycle must be completed before we can detect the viral reporter protein. ISGs produced after binding of IFN-β to the type-I interferon receptor can affect each one of those replication steps including endocytosis, fusion, transcription, and translation. We performed qPCR on several representative ISGs known to have direct anti-viral effects in order to get a sense of the timing required for induction (Figure 3.3-11). We did not observe any increase in CH25H mRNA levels after treatment with IFN-β, but IFIT2, PARP12, and IFITM3 mRNA levels all increased compared to mock three hours into the IFN-β treatment. PARP12 and IFIT2 reached near maximum or maximum fold-change levels by the 7 hour time-point. The length of time required for full transcriptional activation of these ISGs helps to explain why we observe such drastic differences in RFP kinetic parameters at 3-hours IFN-β pre-

treatment compared to 6-hours IFN-β pre-treatment. To put these results in the context of VSV mRNA production, Timm et al. measured that the delay to secondary viral transcription was approximately 3 hours in PC3 cells and varied slightly based on MOI (2.7-3.3 hpi) and further determined that a high dose of IFN-β one-hour prior to infection delayed secondary transcription slightly (2.9-3.8 hpi) (Timm 2013). The ISGs we chose to target are all thought to affect virus replication at or before translation of viral protein.

On average, we see significant differences between the IFN-β pre-treated cells and the un-treated cells. However, within these populations there is still a significant amount of variability. This variability is evident when examining the boxplots of the various kinetic parameters (Figure 3.3-6 & Figure 3.3-7) and when looking at the maximum reporter intensity versus relative delay-time plots in Figure 3.3-8. With the exception of the rise-times perhaps, none of the distributions appear to narrow with longer IFN- β pre-treatment times. The response to an interferon stimulus has been shown many times to be stochastic in nature, even when comparing sister cells after division (Hu 2011).

Multiple measures of viral and cellular activity are best to characterize the variability in virus-host interactions. We are able to obtain a great deal of information using just two reporters including the relative activation and infection times, maximum protein levels and production rates, and lysis times. With more manual single-cell experiments, we are also able to quantify virus yields from isolated infected cells. Using these various measures, we are able to identify several areas of VSV replication that are affected by IFN-β pre-treatments. For example, an ISG that targets fusion might delay detection of the viral reporter, but would not necessarily slow the rate of reporter production. The overall reduction of RFP+ cells in the 6-hour pre-treatment population compared to the other populations might indicate that an ISG is inhibiting

endocytosis. A slow rate of reporter protein production might indicate inhibition of translation or degradation of mRNA. Finally, ISGs that target late processes such as virus assembly or budding might register to us as cells that produced fewer viral particles than would be projected based on the maximum viral reporter intensity. These examples all demonstrate that the ability to obtain kinetic information is extremely important. Likewise, the addition of the IFIT2 reporter provides us with an important measure of the state of immune activation in cells, although IFIT2 itself is much more strongly induced by the virus compared to interferon. The parameters that we can currently measure give us a good picture of the heterogeneity in this virus-host system and how that system is affected when the type-I interferon pathway is activated. We are actively developing methods that will allow us to quantify virus production in the context of our microwell platform and that additional information will help us complete this picture. In addition, methods are being developed to perform PCR using our microwell system and so we could potentially measure interferon stimulated genes and viral genes in single-cells. Advances in cell-coding and other labeling techniques may allow us to obtain even more detailed information from isolated cells. We are limited in the number of wavelengths that can be differentiated using our fluorescent microscope, but this method could be adapted to utilize a different light source capable of distinguishing many more colors.

In conclusion, we have developed a technology that allows us to collect very quantitative and sensitive kinetic measurements of viral and cellular reporter proteins. When combined with other information including qPCR measurements of ISG induction and manual measurements of virus quantification we are able to infer what anti-viral activities are occurring in cells.

3.5 Acknowledgements

This work was aided by a collaboration with Jay Warrick, Ph.D.

3.6 References

1. **Ahmed, M., and D. S. Lyles**. 1997. Identification of a consensus mutation in M protein of vesicular stomatitis virus from persistently infected cells that affects inhibition of host-directed gene expression. Virology 237:378–388.

2. **Ank, N., H. West, and C. Bartholdy**. 2006. Lambda interferon (IFN-λ), a type III IFN, is induced by viruses and IFNs and displays potent antiviral activity against select virus infections in vivo. Journal of … 80:4501–4509.

3. **Atasheva, S., M. Akhrymuk, E. I. Frolova, and I. Frolov**. 2012. New PARP gene with an anti-alphavirus function. Journal of virology 86:8147–60.

4. **Bukholm, G., M. Degré, and P. Whitaker-Dowling**. 1990. Interferon treatment reduces endocytosis of virus and facultatively intracellular bacteria in various cell lines. Journal of interferon research 10:83–9.

5. **Carey, B. L., M. Ahmed, S. Puckett, and D. S. Lyles**. 2008. Early steps of the virus replication cycle are inhibited in prostate cancer cells resistant to oncolytic vesicular stomatitis virus. Journal of virology 82:12104–15.

6. **Elowitz, M. B., A. J. Levine, E. D. Siggia, and P. S. Swain**. 2002. Stochastic gene expression in a single cell. Science 297:1183–1186.

7. **Fensterl, V., J. L. Wetzel, S. Ramachandran, T. Ogino, S. a Stohlman, C. C. Bergmann, M. S. Diamond, et al.** 2012. Interferon-induced Ifit2/ISG54 protects mice from lethal VSV neuropathogenesis. PLoS pathogens 8:1–13.

8. **García-Sastre, A., and C. a Biron**. 2006. Type 1 interferons and the virus-host relationship: a lesson in détente. Science 312:879–882.

9. **Hu, J., G. Nudelman, Y. Shimoni, M. Kumar, Y. Ding, C. López, F. Hayot, et al.** 2011. Role of cell-to-cell variability in activating a positive feedback antiviral response in human dendritic cells. PloS one 6:e16614.

10. **Kato, H., O. Takeuchi, S. Sato, M. Yoneyama, M. Yamamoto, K. Matsui, S. Uematsu, et al.** 2006. Differential roles of MDA5 and RIG-I helicases in the recognition of RNA viruses. Nature 441:101–5.

11. **Lam, V., K. a Duca, and J. Yin**. 2005. Arrested spread of vesicular stomatitis virus infections in vitro depends on interferon-mediated antiviral activity. Biotechnology and bioengineering 90:793–804.

12. **Levin, D., D. Harari, and G. Schreiber**. 2011. Stochastic receptor expression determines cell fate upon interferon treatment. Molecular and cellular biology 31:3252–66.

13. **Liu, S.-Y., R. Aliyari, K. Chikere, G. Li, M. D. Marsden, J. K. Smith, O. Pernet, et al.** 2013. Interferon-inducible cholesterol-25-hydroxylase broadly inhibits viral entry by production of 25-hydroxycholesterol. Immunity 38:92–105.

14. **Liu, S.-Y., D. J. Sanchez, R. Aliyari, S. Lu, and G. Cheng**. 2012. Systematic identification of type I and type II interferon-induced antiviral factors. Proceedings of the National Academy of Sciences of the United States of America 109:4239–4244.

15. **Nakaya, T., M. Sato, N. Hata, M. Asagiri, H. Suemori, S. Noguchi, N. Tanaka, et al.** 2001. Gene induction pathways mediated by distinct IRFs during viral infection. Biochemical and biophysical research communications 283:1150–6.

16. **Perwitasari, O., H. Cho, M. S. Diamond, and M. Gale**. 2011. Inhibitor of κB kinase epsilon (IKK(epsilon)), STAT1, and IFIT2 proteins define novel innate immune effector pathway against West Nile virus infection. The Journal of biological chemistry 286:44412–23.

17. **Rand, U., M. Rinas, J. Schwerk, G. Nöhren, M. Linnes, A. Kröger, M. Flossdorf, et al.** 2012. Multi-layered stochasticity and paracrine signal propagation shape the type-I interferon response. Molecular systems biology 8:584.

18. **Reich, N. C.** 2013. A death-promoting role for ISG54/IFIT2. Journal of interferon & cytokine research : the official journal of the International Society for Interferon and Cytokine Research 33:199–205.

19. **Schwemmle, M., K. C. Weining, M. F. Richter, B. Schumacher, and P. Staeheli**. 1995. Vesicular stomatitis virus transcription inhibited by purified MxA protein. Virology 206:545–54.

20. **Sen G.C., S. S. N.** 2007. The interferon-stimulated genes: targets of direct signaling by interferons, double-stranded RNA, and viruses. CTMI 316:233–250.

21. **Snijder, B., and L. Pelkmans**. 2011. Origins of regulated cell-to-cell variability. Nature reviews. Molecular cell biology 12:119–25.

22. **Snijder, B., R. Sacher, P. Rämö, E.-M. Damm, P. Liberali, and L. Pelkmans**. 2009. Population context determines cell-to-cell variability in endocytosis and virus infection. Nature 461:520–3.

23. **Staeheli, P., and J. Pavlovic**. 1991. Inhibition of vesicular stomatitis virus mRNA synthesis by human MxA protein. Journal of virology 65:4498–501.

24. **Stawowczyk, M., S. Van Scoy, K. P. Kumar, and N. C. Reich**. 2011. The interferon stimulated gene 54 promotes apoptosis. The Journal of biological chemistry 286:7257–66.

25. **Swick, A., A. Baltes, and J. Yin**. 2014. Visualizing infection spread: dual-color fluorescent reporting of virus-host interactions. Biotechnology and Bioengineering.

26. **Terenzi, F., D. J. Hui, W. C. Merrick, and G. C. Sen**. 2006. Distinct induction patterns and functions of two closely related interferon-inducible human genes, ISG54 and ISG56. The Journal of biological chemistry 281:34064–71.

27. **Timm, C., A. Gupta, and J. Yin**. 2013. Kinetics of transcription and replication for an RNA virus: from simple to complex. Journal of Virology, waiting for submission.

28. **Trottier, M. D., B. M. Palian, and C. S. Reiss**. 2005. VSV replication in neurons is inhibited by type I IFN at multiple stages of infection. Virology 333:215–25.

29. **Weidner, J. M., D. Jiang, X.-B. Pan, J. Chang, T. M. Block, and J.-T. Guo**. 2010. Interferon-induced cell membrane proteins, IFITM3 and tetherin, inhibit vesicular stomatitis virus infection via distinct mechanisms. Journal of Virology 84:12646–12657.

30. **Whitaker-Dowling, P. A.** 1983. Interferon-Mediated Inhibition of Virus Penetration. Proceedings of the National Academy of Sciences 80:1083–1086.

Chapter 4: Single-cell analysis of DIP inhibition of virus production

4.1 Introduction

The replication of RNA viruses, such as vesicular stomatitis virus (VSV), is highly error prone and results in heterogeneous virus populations. Adding to this variability are sub-populations of many viruses called defective viral particles. These particles have the same composition as the infectious virus they were created from (i.e. viral proteins, lipid envelope), but the genetic material contained within these particles is incomplete. Defective viral particles often contain genomes missing several essential genes and those deletions make these defective particles incapable of self-replication. Some defective particles, however, have the ability to interfere with the replication of infectious virus. These *defective interfering particles* (DIPs) are essentially parasites of infectious virus, and interfere with normal virus replication by 'stealing' the viral polymerase and structural proteins for their own replication and assembly.

Defective interfering particles have been found in cultured lab strains of many DNA and RNA viruses, including VSV (Huang 1970; Lazzarini 1981). It was long thought that the production of these particles was the result of cell culture conditions, but in the last few years, defective interfering particles have been found in natural systems, specifically in people infected with Dengue virus (Li 2011) and birds infected with West Nile Virus (Pesko 2012). Several theories exist as to why DIPs might be produced during infections, including a way of naturally attenuating virus replication so that the host remains mobile, but contagious, making that host able to spread the virus more effectively (Li 2011). Another theory suggests a role for DIPs in the development of persistent viral infections (Holland 1974) and DIPs for various viruses including West Nile virus (Brinton 1982), Murray Valley encephalitis virus (Lancaster 1998),

and Japanese encephalitis virus (Schmaljohn 1977; Tsai 2007) have been isolated in persistently infected cell cultures.

The ability of DIPs to interfere with infections in culture has been well established and has given rise to the idea that DIPs could potentially be used in anti-viral therapies. The principal challenge in developing treatments for viruses, particularly fast evolving RNA viruses, is that these viruses adapt too quickly to new drugs and vaccines. Defective interfering particles, however, contain the highly conserved promoter regions necessary for virus replication. Therefore, the hypothesis is that RNA viruses would not be able to evolve to escape treatment with DIPs (Szathmary 1993; Kirkwood 1994).

DIPs are of great research interest because of their potential role in natural infections and possible therapeutic value. Despite the importance of DIPs, the exact mechanisms by which they interfere with viral infections are not well understood. Additionally, the established predator-prey relationship between DIPs and infectious particles makes the dosage of DIPs required to suppress an infection a complicated question. Co-infections, in both cell cultures and mice infected with VSV, can result in a cyclic pattern of virus production, and often lower DIP doses are more effective (Cave 1985). We believe we can gain insight into the interference mechanisms of DIPs and their effects on virus spread by studying co-infections of DIPs and infectious virus particles in isolated single-cells. Previous work by Sekellick and Marcus quantified the infections VSV production from Vero cells infected in monolayers and then isolated cells by aspirating with a micropipette (Sekellick 1980). Their results showed that the majority of cells co-infected with a multiplicity of DIPs of 1 or 16 produced no viral particles, but that some cells still had relatively high yields. We will perform similar experiments using single-cell methods that have been previously described (Timm 2012), and expand on that work

by utilizing a recombinant strain of vesicular stomatitis virus encoding an RFP gene, DSRed-Express (VSV-DSRed) and a stock of DIPs created from this reporter virus strain (Chapter 2). Using this reporter virus we can quantify both viral yields and the kinetics of a reporter of viral protein production.

4.2 Materials and Methods

4.2.1 Cell and virus culture

Baby hamster kidney cells (BHK) were passaged every 2-3 days and grown in MEM (Cellgro) supplemented with 10% FBS (Atlanta Biologicals) and 2mM GlutaMAX (Gibco). Infections were done in the same media, but with the FBS content reduced to 2%. The virus used in this study was a recombinant strain of vesicular stomatitis virus (VSV-DSRed) encoding the gene for DSRed-Express protein in the fifth position of the genome, after the glycoprotein gene and before the polymerase gene. By placing the reporter gene in this position, attenuation caused by adding an additional gene is limited, but virus replication still results in a strong fluorescent signal. The DIPs were created from our VSV-DSRed stock.

4.2.2 DIP production and stocking

The procedures for preparing the DIP stock virus have been previously described (Akpinar). DIPs were produced by high multiplicity serial infections (passages) using N1-DSRed virus. The passage with the highest DIP concentration ($2.3x10^8$ interfering units/ml) was stored at -80°C for later infections. No RFP expression was observed in only DIP infected cells.

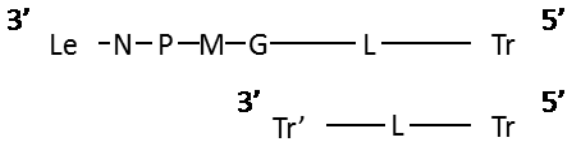

Figure 4.2-1: DIP structure. (top) VSV genome. (bottom) DIP genome. The VSV polymerase initiates either transcription or anti-genome production at the negative-sense Leader sequence and initiates genome replication at the positive-sense, Trailer sequence on the anti-genome. The 3' end of the DIP genome (negative-sense) contains the positive-sense, or complement of the 5' Trailer, which is the genomic replication start site. This is a panhandle type DI genome (Lazzarini 1981; Whelan 1997).

4.2.3 DIP adsorption experiment

BHK cells were infected in solution with an N1-DSRed MOI of 10, and varying amounts of DIPs that were approximately 140, 14, 1.4, and 0 DIPs per cell. The virus-cell solution was incubated on ice for 30 minutes to allow adsorption of virus and DIPs, warmed for 5 minutes in an incubator to internalize attached particles, and then centrifuged 3x to pellet cells and remove supernatants containing excess virus. The infected-cell solution was then diluted in a cell suspension of equal density and plated in 6-well plates. Based on the cell count in the infected-cell population, we expected 62 infected cells to be plated in the most dilute infected-cell solution. After 1.5 hours, the supernatant covering the new cell monolayers was removed and replaced with an agar solution. At 20 hpi, the plates were scanned on the Typhoon FLA 9000 and RFP positive plaques were identified. ImageJ was used to estimate the relative size of the RFP plaques in the Typhoon images.

4.2.4 Manual single-cell yield experiments

The in-solution infection procedures are the same as described above although the multiplicities of DIPs (MO-DIPs) used in this experiment were approximately 10, 1, 0.1, and 0 for these experiments. After the centrifugation and re-suspension was done three times for this experiment to increase the likelihood that all the DIPs were removed from the infected cell suspension, the cell suspensions were added to wells of 4 96-well plates at densities of approximately 13400 cells per well (control) or 1 cell per well. The plates were manually scanned to locate wells containing just one cell. High density wells and single-cell wells were sampled at 24 hpi and quantified via plaque assay. One plate was used for time-lapse imaging to acquire RFP kinetics from the DIP co-infected cells. These images were taken at 10x magnification and were analyzed using a macro written in ImageJ.

4.2.5 Cell density experiments

BHK cells were infected in-solution at an MOI of 5 with VSV and plated at 5 different densities spanning 4 orders of magnitude. Single-cell wells were manually identified and cells in wells containing ~10 cells/well were counted for accuracy. It was assumed that the three higher densities were 10, 100, and 1000 fold higher than the average of the ~10 cell/well average. Samples were collected from 10 wells at each density, 24 hpi. The virus produced by the cells in these wells was quantified with a plaque assay.

4.2.6 Nuclear labeling and VSV-DIP co-infections for microwell experiments

BHK cells were infected in-solution at an MOI of 10 with N1-DSRed and co-infected with varying amounts of DIPs. The methods for performing the in-solution infections have been

previously described (Timm 2012). Following the virus adsorption period, the temperatures of the virus-cell solutions were raised to 37°C in a water bath for 5 minutes to allow for internalization of the attached virus. To remove any excess virus, the cell solutions were centrifuged (1000 rpm, 4 min), the infection media decanted, and the infected cell pellet re-suspended in fresh media. This procedure was repeated 3x to eliminate excess virus and DIP in the cell suspension, which was adjusted in density to approximately 1-2 x 10^5 cells/ml. The re-suspension media contained Hoechst 33342 (AnaSpec, 1μM) and HEPES (Sigma-Aldrich, 25mM). Hoechst 33342 is a live-cell nucleic acid stain that can be used to identify the location and number of cells in microwells. HEPES is a buffer commonly used in microfluidics applications to protect the cells in systems with sub-optimal gas exchange.

4.2.7 Bull's-eye device seeding and assembly

4.2.7.1 Microwell device prep

One hour prior to the infection the microwell device was placed on a clean glass slide in the aluminum device holder (Section 1.2.2) and placed under a UV lamp for 30 minutes for sterilization. After UV treatment, the device was moved to a vacuum chamber to de-gas the PDMS microwell device for 30 minutes. Once the device was de-gassed, media droplets containing Hoechst 33342 (AnaSpec, 1μM) and HEPES (Sigma-Aldrich, 25mM) were placed on each bull's-eye and placed in a humidified incubator until cell seeding (~ 1 hour). Pre-wetting the device is necessary for good cell seeding and 'humidifying' the PDMS helps with overall cell health.

4.2.7.2 Cell Seeding

To seed the infected cells into the microwell device, the existing droplets were removed and replaced with 70-80µl droplets of the infected cell solution (1-2 x 10^5 cells/ml). After 30-60 seconds, the droplets were removed swiftly by placing the pipette tip in the recessed center and replaced quickly, but gently with fresh media. The swift removal of the droplets sweeps cells off the top surface of the device, but does not disturb the cells that have settled into the microwells. It is necessary to keep the pipette vertical and not pipette from an angle. The bull's-eyes were washed with fresh media twice more in the same manner. It is important not to overload the wells with cells, as they are difficult to wash away once seeded and overloading will cause cells to become trapped outside the wells and crushed during sealing. The nuclear stain of these cells will still be visible and will interfere with image analysis.

4.2.7.3 Device sealing

The device was sealed by quickly removing the droplets from all bull's-eyes and gently covering with a glass slide (top side treated with 0.1% tween). It is important not to add and then release pressure to the microwells as this causes bubbles to form and displaces cells. The tween is applied by pipetting on ~1 ml of 0.1% tween, then before sealing, removing all but a thin layer of the solution. Tween is a surfactant that prevents condensation droplets from forming on the top side of the sandwich device when inside the humid microscope chamber; instead, an even layer of liquid forms. The liquid layer does not affect fluorescence, and an even liquid layer instead of droplets allows for better topside phase contrast images. Pressure is applied to maintain the sealing as described in Section 1.2.2. Pressure was applied to enable complete

sealing of the microwells, but without permitting glass slides to break. In this experiment two bull's-eyes each were seeded with cells co-infected at one of the four MO-DIP conditions.

4.2.8 Time-lapse imaging

As described in Section 1.2.3.1, correction images were taken before beginning the time-lapse to correct for uneven light intensity. The exposure times for the illumination correction images was 5ms and the exposure time for the dark field correction images was 1500ms (or the longest exposure time used). All images for microwell experiments were taken at 4x magnification.

The aluminum device holder containing the bull's-eye device and several DPBS soaked Kim-wipes was placed on the automated microscope stage. The DPBS soaked Kim-wipes help provide a humid environment for the PDMS device. Fluorescent time-lapse imaging was done on a Nikon Eclipse TE300 microscope, using an EXI aqua camera (Q Imaging). The environmental conditions were controlled by an outer warming chamber encompassing the microscope and a stage-top incubator chamber (Pathology Devices) set to 37°C, 5% CO_2, and approximately 85% RH. Once the system had equilibrated to the correct temperature, the center locations of the bull's-eyes were identified and memorized and the stage was focused to the Hoechst 33342 stained nuclei. Images were taken in a 4 x 3 array around the center of each bull's-eye in the following order: bright-field (5ms exposure), blue channel (20ms exposure), red channel (1500ms exposure) using a Sedat quad cube. Imaging the entire array required approximately 7 minutes, and was looped at a 20 minute interval for 22 hours beginning 1.58 hpi.

4.2.9 Image processing workflow and data analysis

Image organization and processing was done in JEX as described previously (Warrick TBD). Briefly, the images were sorted according to location, time, and color and then registered

to correct for any small shifts in the device location. For this work, registration was done based on the phase contrast images. Following registration, the microwell locations were identified and numbered using JEX scripts. The maxima in the blue channel (# of nuclei) were located and the number in each microwell determined. Finally, an appropriate value for the cell radius was chosen and measurements were taken about the maximum signal in each single-cell well using a standard area based on this radius. The measurement and cell count data tables are exported and analyzed in Matlab.

4.2.9.1 Matlab analysis

The code used to analyze the microwell data can be found on the Yin lab's shared server in Past Group Members\Andrea\MatlabCode\Chapter4. In order to perform the analysis in Matlab, the ARFF files exported by JEX must be converted into a format readable by Matlab. This is done with the Matlab Weka Interface. The file names of various scripts necessary for each step are written in italics. The procedure, which is repeated here, is the same as the procedure described in Chapter 2, however several scripts require one to input that there is no GFP data in these experiments. That adjustment is clearly marked in the script files.

Step 1: Extract cell counts and cell location information

Run *CellCountDriver.m* → requires *CellCountFunction, loadARFF, weka2matlab, convertIndex,* and *wekaPathCheck* scripts

Step 2: Extract measurements

Run *MeasuresDriver.m* → requires *MeasuresFunction, loadARFF, weka2matlab, covertIndex,* and *wekaPathCheck* scripts

Wells that contained zero or one cell were identified and the measurements corresponding to those wells collected and organized according to image location for easier analysis. After this data extraction step, the data must be cleaned. Cleaning of the data entails sorting through the images taken at each color, and excluding microwell locations that contained fluorescent debris, bubbles, or other factors that might result in an incorrect measurement. A log of the errors is created, and those microwells are excluded from Matlab data tables.

Step 3: Create error log

Fill in *ErrorLogCreator.m* script file with the microwell numbers that must be eliminated from analysis. Run *ErrorLogCreator*, then run *ClearListsDriver* → requires *CleanROILists*

The empty wells were used to determine the signal from the PDMS (Ø signal) and the measurement threshold. The mode from the single-cell wells was subtracted from the cell signal at each time point. The mode is essentially the background signal at each well location. Finally, the measurement error was determined and found to be negligible until values drop below approximately 10 au (CV ~ 10%), near the limit of detection (Section 2.2.7.4).

Step 4: Run *AnalysisDriver.m*

→ loads time information, loads cleaned ROI lists, loads measurements, loads cleaned cell locations, loads illumination correction image and runs

measureBackground, measureThreshold, illuminationCorrection, and thresholdData.

At this point the cleaned, thresholded data is complete and is saved for more specific analysis. It is necessary at this point to check the maximum threshold used on all the data. Occasionally, a cell will not retain the nuclear stain and a well designated as empty will have a positive reporter signal and this will artificially raise our limit of detection. The individual thresholds for each image location should be checked for similarity. If one or more of the individual thresholds are too high, we identify the problem microwell, add that microwell number to the *ErrorLogCreator* and run through Steps 3 and 4 again.

Step 5: For the virus reporter data collected in this work, specific functions were created to identify and collect data from cells that were RFP+, plot reporter trajectories for these infected single-cell, and extract the desired kinetic parameters.

→ *RFP_GFPData* and *Delay_RFPDeath* → requires *fit_expo_fun, find_RSquared, expo_objfun, expofun* (fitting functions written primarily by Ankur Gupta)

4.3 Results

The effects of co-infections with DIPs and infectious virus are generally quantified with an interference assay, which is performed by serially diluting an unknown number of DIPs in solutions of infectious virus stock and then determining what dilution is required to eliminate interference. The interference assay assumes that only one DIP is required to interfere with virus production, and is based on population level yields (Bellett 1959). Here we develop single-cell

infection techniques that enable more direct measures of infections virus and DIP production from co-infected cells.

4.3.1 DIPs reduce number of productive infections and inhibit spread of infection

DIP particles are composed of viral envelope and structural proteins identical to those of an infectious virus particle. Therefore, we expect no significant difference in binding affinity to BHK cells in solution. By infecting cells in solution with different dilutions of DIPs, we expected to find a gradient in productive infections based on the multiplicity of DIPs (Mo-DIP). The interference was measured relative to the infection performed in the absence of DIPs (Figure 4.3-1). Adding an MO-DIP of ~1.4 to cells infected at an MOI of 10 with N1-DSRed reduces the number of productive infections ~75% and adding 10, and 100-fold more DIPs reduces virus production to less than 1% of the maximum infectivity. The Poisson distribution is often used to approximate the distribution of virus particles adsorbed by cells at various MOIs (Adang 2006; Stauffer Thompson 2009; Zhu 2009). According to the Poisson distribution, the probability that cells exposed to an MO-DIP of 14 will not internalize a DIP is negligible (less than 10^{-6}). The number of plaque forming infected cells at MO-DIP 14, and 140 was very low (less than 1% of MO-DIP 0 control), but it was not zero so these co-infected cells are able to produce infectious virus. The decrease in virus production observed with increased MO-DIP suggests that DIPs adsorbed efficiently to BHK cells.

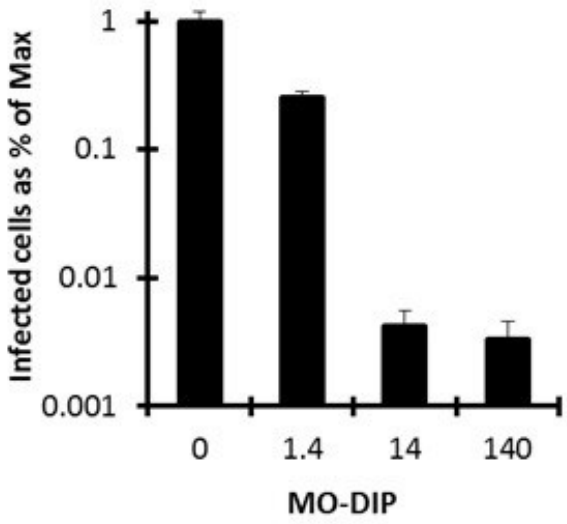

Figure 4.3-1: Plaque reduction with increasing MO-DIP. Plaque counts are normalized relative to the no DIP case. Plaque counts were reduced with the addition of DIP co-infections, and reduced significantly (less than 1% of max) when the DIP concentration added was enough for every cell to be co-infected with DIPs (MO-DIP 14, 140) and virus based on a Poisson distribution.

The results shown in Figure 4.3-1 indicate that DIPs very effectively shut down virus replication in co-infected cells. However, a plaque assay does not just measure the number of infectious viral particles. The formation of a plaque requires that the initial infection spreads to neighboring cells and spreads far enough to be visible on a macroscopic level. It is possible for a DIP co-infected cell to produce both DIPs and infectious virus, and it is possible that the production of DIPs from that initial infected cell is able to halt spread of infection enough to prevent formation of a visible plaque. To better understand the effects of DIPs on VSV replication and spread we analyzed the size of the plaques produced at each MO-DIP. The plaques were measured at 2 different time-points (22 and 27 hpi). At the later time, more plaques were visible at MO-DIPs 1.4, 14, and 140, implying plaque growth resulting from these co-infections could be slower. Example images of RFP+ plaques scanned at the early time-point are

shown in Figure 4.3-2 a-d. Plaque size was quantified using ImageJ at the early and late times and the average normalized plaque size for each MO-DIP condition is plotted in Figure 4.3-2 e. Using the plaques analyzed at both time-points we estimated the plaque growth rate at each condition (Figure 4.3-2 e). Compared to the no DIP condition, plaque sizes are smaller and growth rates are slower and more variable when cells are co-infected with DIPs.

4.3.2 DIPs reduce viral yields and viral protein production, but do not completely inhibit production

We have strong evidence that even at high MO-DIPs, VSV infections are not completely suppressed (Figure 4.3-1). We have also shown that the plaque growth is more variable at high MO-DIP infections (Figure 4.3-2). We would now like to better characterize this system by studying infectious virus yields from single-cells

The reporter virus, which encodes the red fluorescent protein DSRed-Express, has been shown to accurately report on virus replication kinetics and virus production (Chapter 2). For infections of BHK cells, the RFP expression has similar kinetics and spans similar orders of magnitude as the virus production kinetics (Figure 4.3-3).

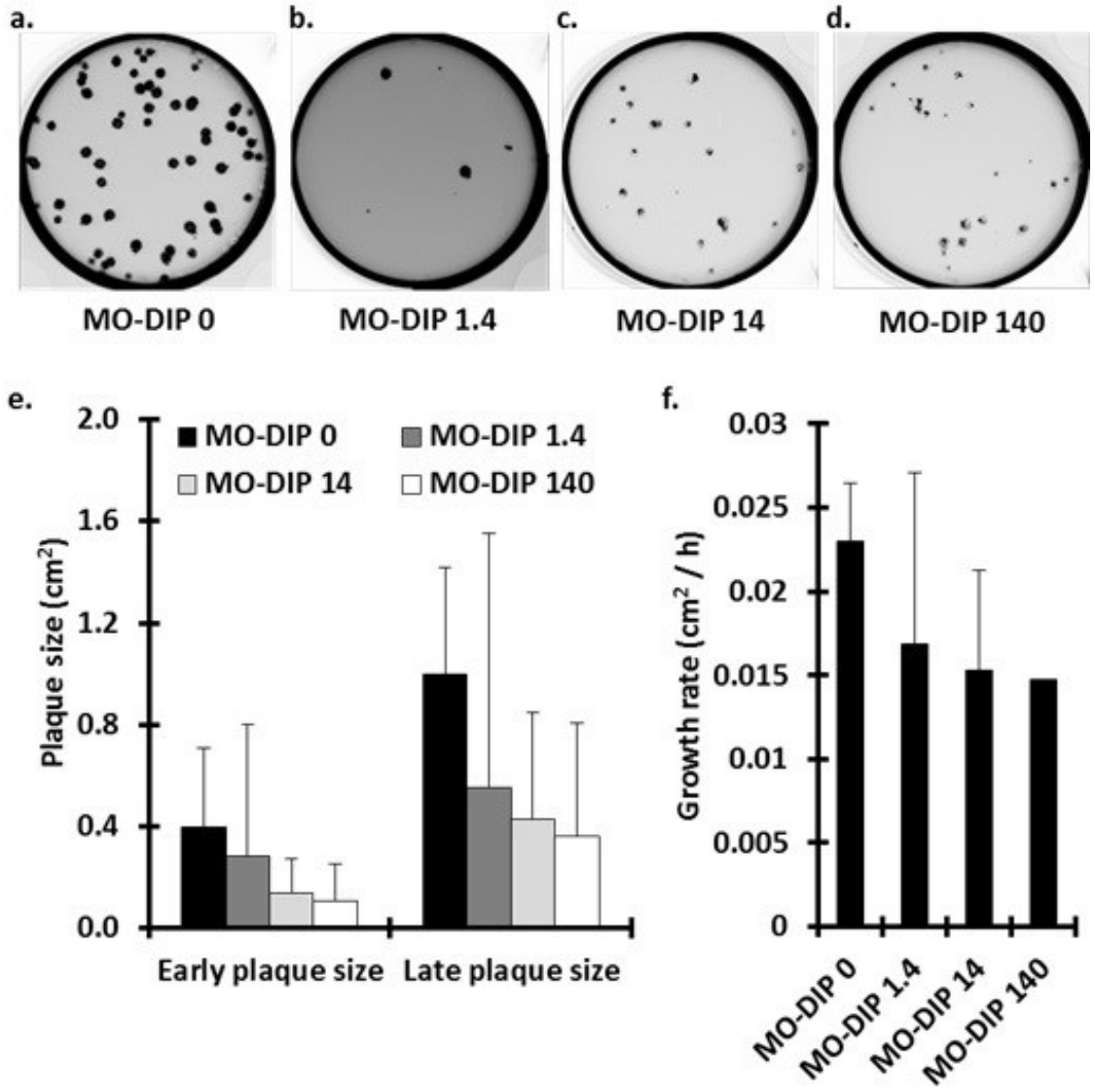

Figure 4.3-2: Plaque growth slower, more variable at high MO-DIPs. (a. & b.) Images of RFP+ plaques from MO-DIP 0 and MO-DIP 1.4 co-infections. (c. & d.) Images of RFP+ plaques from MO-DIP 14 and MO-DIP 140. (e.) Normalized plaque size comparisons of the four MO-DIP conditions measured at 22 hpi, and five hours later at 27 hpi. (f.) The growth rate is approximated by measuring the same plaques at the two different time-points.

BHK cells were infected in solution with a high MOI of N1-DSRed, sufficient to infect every cell, and varying MO-DIPs. Wells containing single-cells were identified and sampled 24 hpi. The amount of infectious virus produced from these isolated cells was quantified with plaque

assays and the yields from those cells are shown in Figure 4.3-4 (black circles). The average viral yields from isolated cells co-infected at MO-DIP 0, 0.1, 1, and 10 were 1758, 2005, 144, and 23, respectively. Virus production at MO-DIPs 0 and 0.1 were not statistically different (Mann-Whitney, p=.44), but virus production at MO-DIP 1 (p=0.00) and MO-DIP 10 (p=00) were significantly reduced. Notably, only 4 cells (1 cell at MO-DIP 1 and 3 cells at MO-DIP 10) produced no detectable infectious virions (LOD at ~2, with high error). Wells containing a high-density of infected cells (~13,400 cells/well) were also sampled at 24 hpi. The average yields from 3 wells per MO-DIP condition are shown in Figure 4.3-4 (red squares). The average per-cell yield from the population level infections was higher than the single-cell averages at each condition, but the yields decreased with each increase in MO-DIP from 7640 PFU/cell at MO-DIP 0 to 87 PFU/cell at MO-DIP 10.

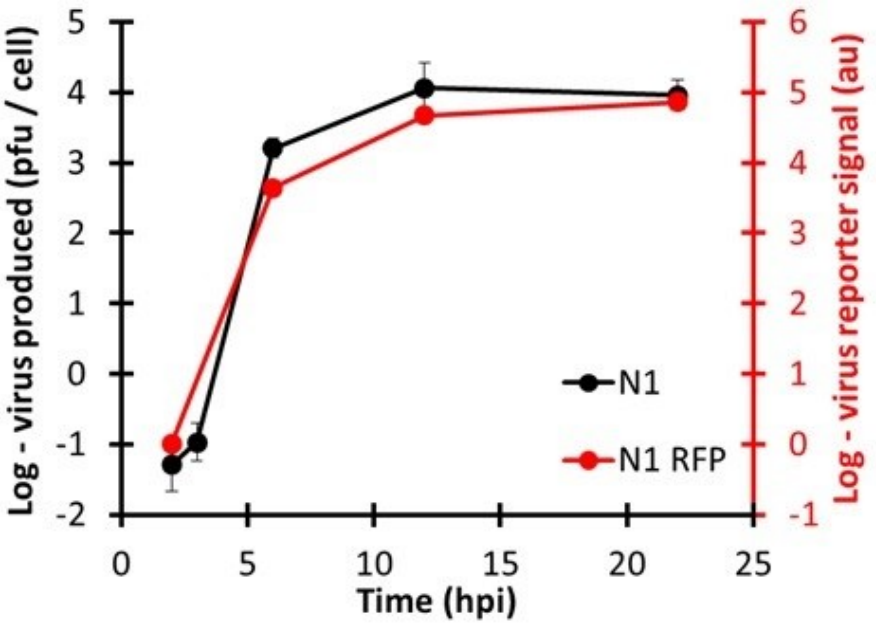

Figure 4.3-3: RFP intensity can be used to approximate virus production kinetics and yields.

We measured the virus production from ~ 70 isolated single-cell infections co-infected at different MO-DIP conditions. We were also able to track the RFP kinetics for all the isolated single-cells contained in one 96-well plate (21 cells) also co-infected at different MO-DIP conditions. We wished to determine how the RFP production kinetics might be related to infectious virus yields in single-cells. Due to the small number of samples at MO-DIP 0.1, it is unlikely that any of these cells were infected with a DIP, therefore, we have combined these cells with the cells at MO-DIP 0 and plotted the infectious virus yield of those cells plotted against the maximum measured RFP intensity. The maximum RFP intensity was correlated with yields (R^2 = 0.83) using this population of single-cells. However, if we compare cells unlikely to be co-infected with DIPs with those likely to be co-infected with DIPs (MO-DIP 1, 10) we observe a different relationship between the maximum viral reporter intensity and the infectious virus yields from these cells – one that predicts higher infectious virus yields than are observed. The viral proteins represented by the reporter signal are used for DIP replication as well as infectious virus replication, and also for DIP assembly. The table in Figure 4.3-4 d summarizes the average yields and max intensities at each MO-DIP condition and also suggests estimated amounts of DIP production assuming 2 DIPs can be made using the protein resources required for 1 infectious particle. We estimate 2 DIPs because of sequencing data that shows the DIP genomes in our stocks are composed of a large part of the L gene only, which is less than half the length of a full length genome (Timm n.d.).

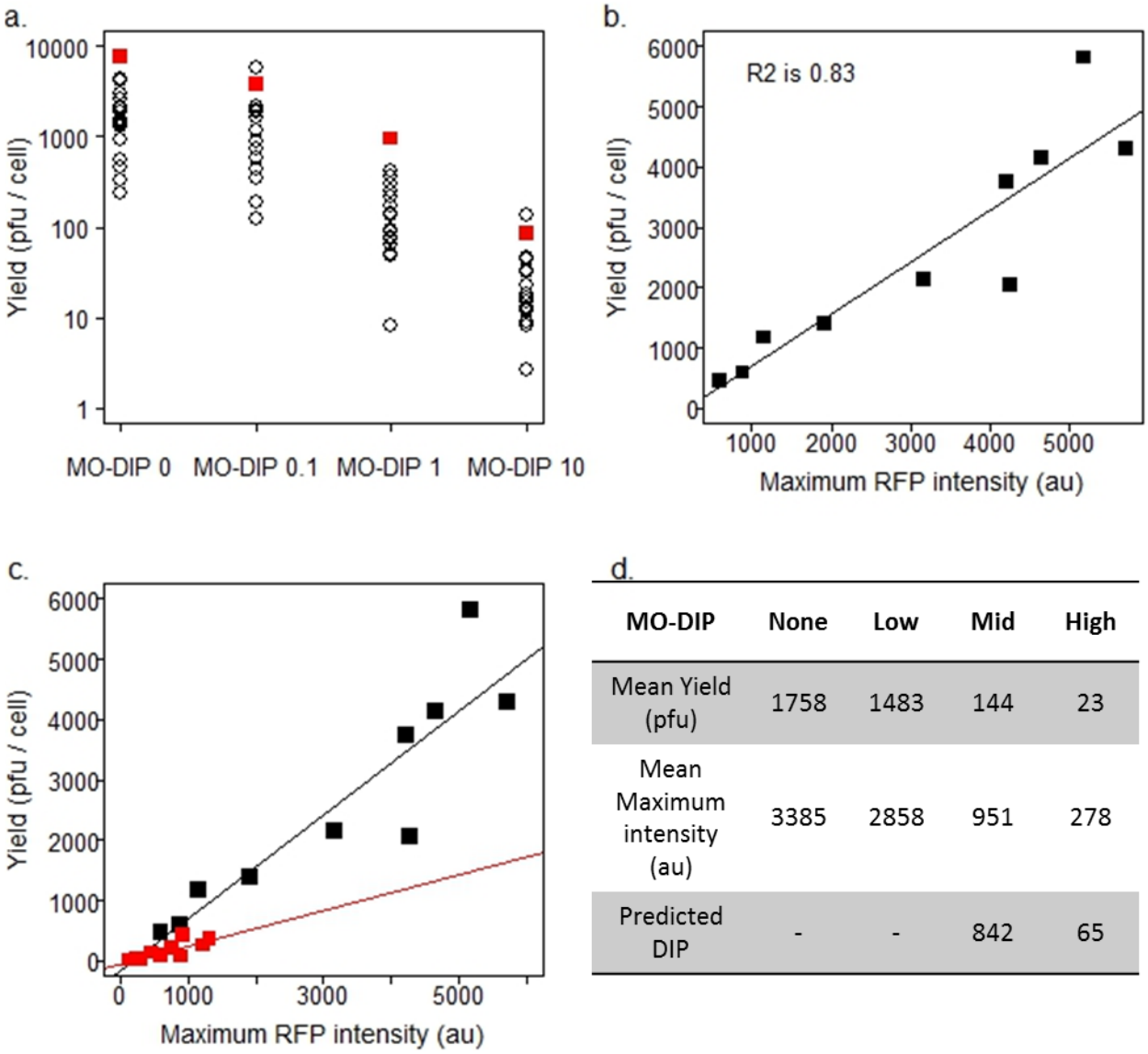

d.

MO-DIP	None	Low	Mid	High
Mean Yield (pfu)	1758	1483	144	23
Mean Maximum intensity (au)	3385	2858	951	278
Predicted DIP	-	-	842	65

Figure 4.3-4: Single-cell and population yields from co-infected cells. (a) Black circles represent the single-cell yields from each cell samples (three cells producing 0 PFU not shown). Red squares represent the per cell yields from high density wells. (b) Correlation of MO-DIP 0 and MO-DIP 0.1.

4.3.3 Increasing cell density, increases VSV per cell yields

BHK cells were infected in-solution with N1-VSV and plated at the densities indicated in Figure 4.3-5. The average virus produced per cell was plotted against the cell density. As the cell

density approaches the density of a confluent monolayer, the per-cell virus yields increase. The difference between the lower density and higher density yields is nearly 5-fold. This difference is similar to measured differences between the population yields and single-cell yields of the DIP co-infections (> 4-fold).

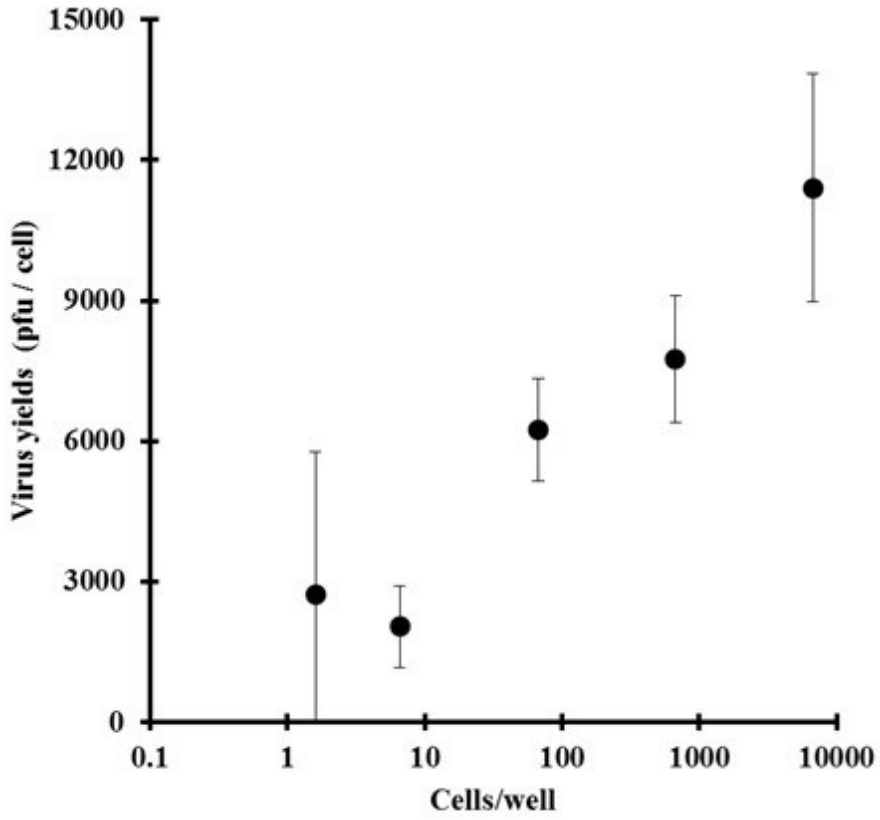

Figure 4.3-5: Viral yields increase with cell density. There is a greater than 4-fold increase in virus production per cell when infected BHK cells are plated at increasing densities from an average of 1.6 cells/well to ~6700 cells/well.

4.3.4 Microwell virus reporter kinetics from DIP-infectious virus co-infections

We are able to determine the yields of infectious virus produced from single-cells co-infected with DIPs, but we would like to investigate how the kinetics of viral protein production are changed by DIP co-infections. We use recombinant virus strains encoding fluorescent reporter

proteins to study virus replication inside of host cells. The use of these fluorescent reporter viruses allow us to increase our sample size significantly when combined with microfluidics and high-throughput imaging and data analysis. We are able to obtain similar trajectories to those shown in Figure 4.3-3 from individual cells by imaging isolated infected cells in microwells over the course of an infection. To characterize the virus reporter protein trajectories, we have defined several terms including the delay-time, the production rate, the rise-time, and the maximum intensity. These parameters have been previously described (Chapter 2). Briefly, the delay-time is the time at which the reporter signal first crosses our limit of detection. The rise-time is the period between the delay-time and the time at which 85% of the maximum intensity is reached. To approximate the production rate, we fit an exponential curve to the first four detectable data points and designate the exponential, alpha, as the approximate production rate (Equation 4.3-1)

Equation 4.3-1

$$Intensity = A \cdot \exp(\alpha \cdot time)$$

BHK cells were co-infected, in-solution with the N1-DSRed virus (MOI 10) and various amounts of DIPs and seeded in a microwell device. These infected cells were imaged every 20 minutes from ~1.5 hpi to ~24 hpi. Using the no DIP case as the theoretical maximum, we found that the number of infected cells in which we detected the viral reporter decreased with MO-DIP as indicated in Table 4.3-1. The maximum measured intensities also decreased significantly with each increase in MO-DIP (p=0), as did the distributions of those intensities (Figure 4.3-6). Finally, the reporter production rates (alphas) also decreased significantly as the MO-DIP was increased (p=0). We were only able to extract production rate information for a very few cells at MO-DIP 10 because most of the fits were not very good (criteria $R^2 \geq 0.9$). The bad fits were

usually due to the cells reaching a maximum in production very shortly (within 1.5 hours) of exceeding the limit of detection.

Table 4.3-1: Comparison of the percentage of RFP positive cells, maximum intensity means, and production rate means for the 4 MO-DIP conditions.

MO-DIP	Normalized % RFP Positive	Maximum Intensity (au)	Production Rate (1 / h)
0	100%	465	1.72
0.1	100%	199	1.51
1	76%	83	1.18
10	30%	14	0.48

We noted in Section 4.3.1 that the speed of infection spread at higher MO-DIPs seemed significantly slower, and the plaque sizes were highly variable. Plaque growth can be slowed by lower yields, but also by a slower virus replication. We examined the effects of DIPs on the production of the viral reporter protein and have prepared boxplots of the delay-times and rise-times for each MO-DIP condition. The increases in delay-times as the MO-DIP was increased were striking. We have noted before that the initial detection of progeny virus from VSV infections of BHK cells occurs in a very narrow window (Timm 2012). Furthermore, at MO-DIP 0 the distribution in detection times is extremely narrow with an average value of 4.3 hpi. In contrast, the average delay-time at MO-DIP 10 was nearly 12 hpi. To put this number in context, VSV infections of BHK cells are usually complete and have resulted in death of the cell around 12-14 hpi.

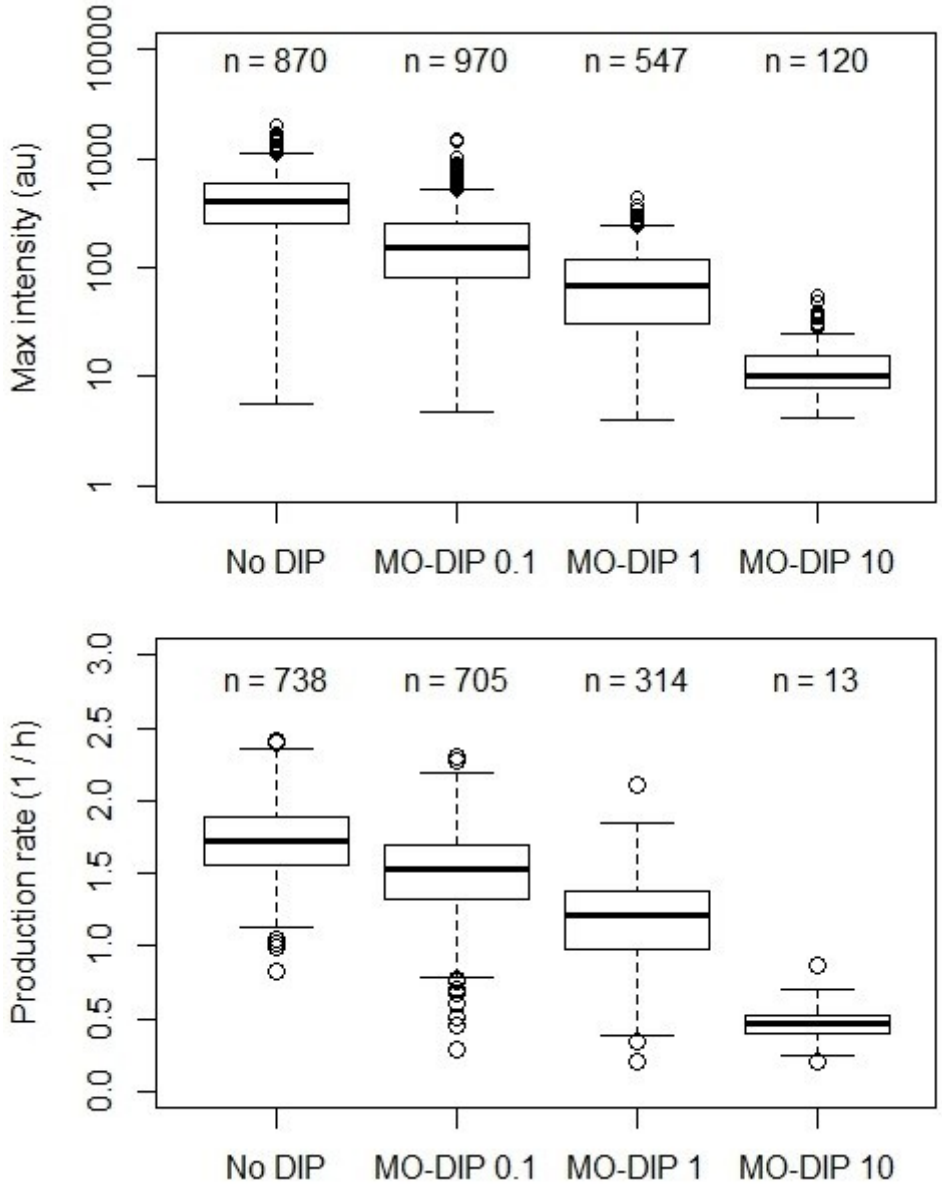

Figure 4.3-6: Maximum intensity and production rate data for each MO-DIP condition. (top) Maximum intensity data, cells that did not lyse or reach a plateau before the end of imaging were excluded from this analysis. (bottom) Production rate data, only good fits (defined as $R^2 \geq 0.9$) were included in this analysis. Both maximum intensities and rates of reporter production decreased at higher MO-DIPs.

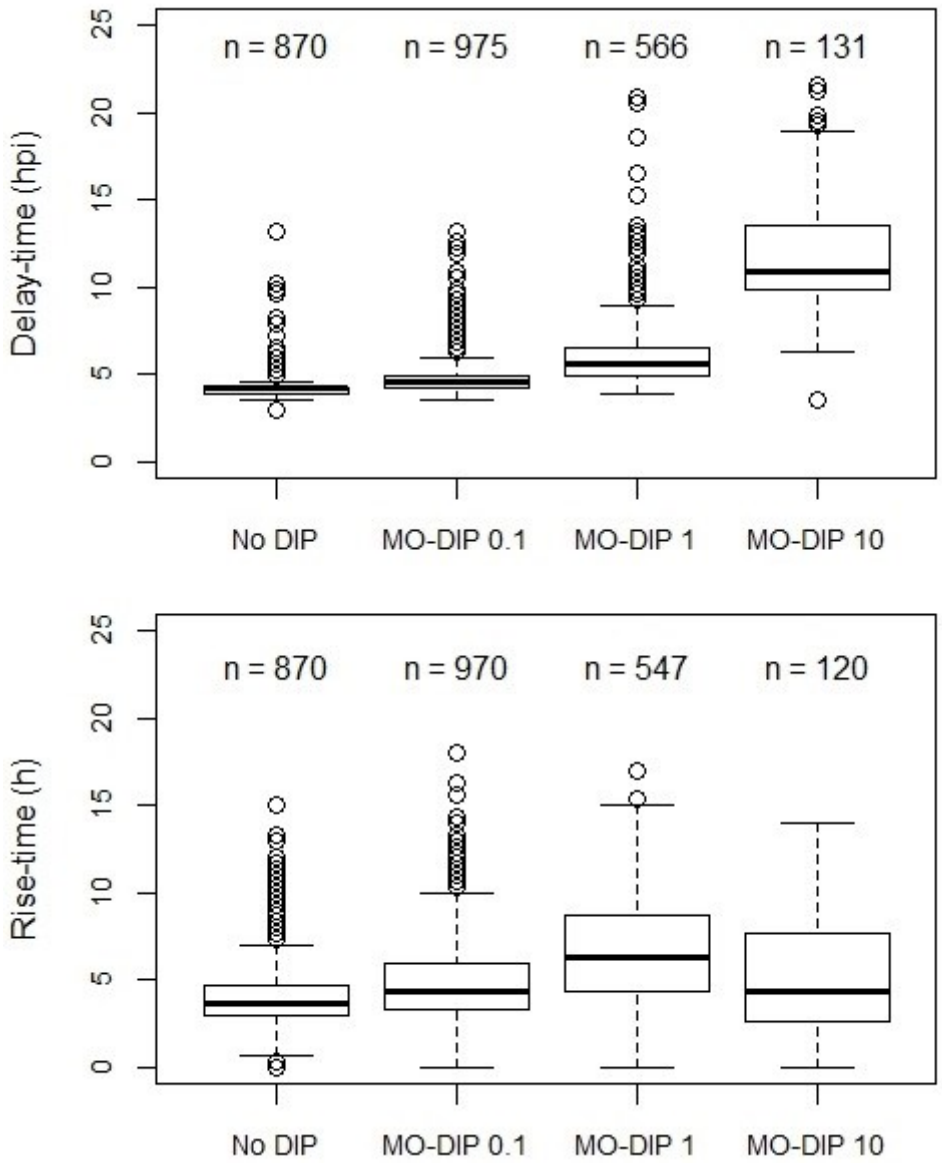

Figure 4.3-7: Delay-time and rise-time data for each MO-DIP condition. (top) Delay-time data, the delay to detection of the RFP reporter increased significantly at higher MO-DIPs. (bottom) Rise-time data, cells that did not lyse or reach a plateau before the end of imaging were excluded from this analysis.

4.3.5 Longer delay-times likely due to slower protein production

Our analysis of the various viral reporter kinetic parameters clearly shows that increasing the MO-DIP causes significant decreases in the maximum intensities and production rates, and also causes significant delays in detection time. The delay-time represent a series of early viral infection steps all lumped together including endocytosis, fusion of the viral and cellular membranes and release of the viral genome, primary transcription, and translation of viral protein. It is probable that genome replication, and secondary transcription and protein translation are also required before we reach detectable levels of viral reporter protein. Therefore, the delay-time we measure is dependent on the rate of protein production (alpha) among many other factors. We plotted the production rate against the delay-time to determine the degree to which the delay depends on the production rate (Figure 4.3-8). We observe in Figure 4.3-8a, as we also saw in Figure 4.3-7 top, that the delay-time distribution at MO-DIP 0 is narrow and not greatly influenced by the production rate. However, at MO-DIP 0.1 and 1, longer delay-times do appear to be related to lower production rates.

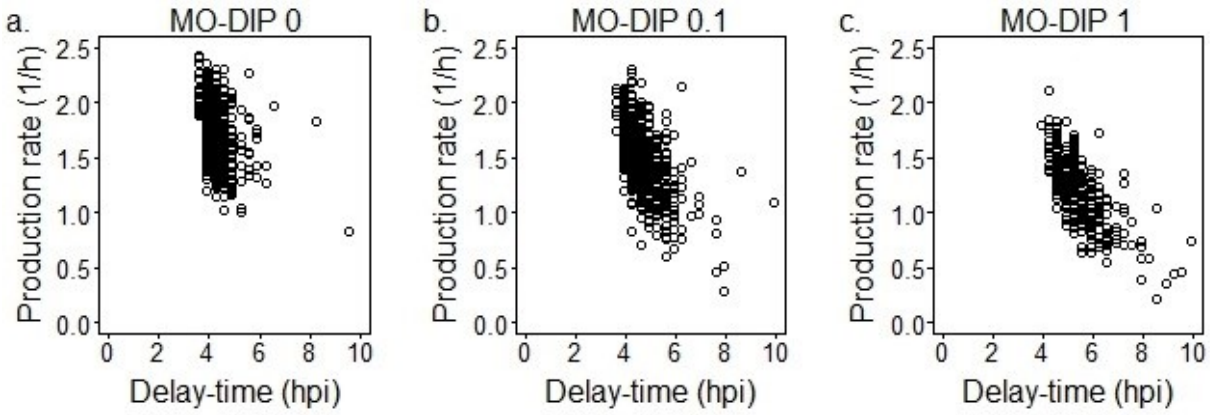

Figure 4.3-8: Longer delay-times associated with lower production rates at MO-DIP 1 and 10.

4.4 Discussion

Defective interfering particles are interesting subjects of research due to their potential use as anti-viral therapies and their recently discovered role in natural infections (Li 2011; Pesko 2012). DIPs are attractive possibilities for use as anti-viral therapies due to the fact that they contain the highly conserved primer regions of the virus they originated from, and so it would be difficult for that virus to evolve away and escape treatment with DIPs. Much work is already being done to developed vaccines based on interference (Noble 2004; Mann 2006; Marriott 2010).The similarities that DIPs share with viruses also present challenges to their detection, quantification, and determination of anti-viral activity. The single-cell analysis and non-traditional detection methods presented in this paper represent steps forward in the characterization of DIP quantification and interference activity.

Previous work was done by Sekellick and Marcus to quantify infectious VSV production from single-cells (Sekellick 1980). There were similarities, but also significant differences between their work and ours. First, we used similar MOIs (Sekellick – 8.5; Timm – 10), and similar MO-DIPs (Sekellick: 0, 1, 15; Timm: 0, 0.1, 1, and 10), but the maximum yield we observed at MO-DIP 10 was 136 and Sekellick and Marcus observed many cells at MO-DIP 16 producing thousands of infectious particles. Additionally, they also observed many cells, both at MO-DIP 1 and MO-DIP 16 that produced no detectable virions (> 40%) and our rate of non-producers was much lower (~10%). We should note that their sample size was much larger than our low-throughput single-cell yield measurements (n = 180 at MO-DIP 16, n = 160 at MO-DIP 1 vs. n = 19 at both MO-DIP 1, and 10); however, we believe the differences in non-producer ratios are due to the infection procedure rather than a difference in sampling. The in-solution

methods we use to co-infect cells with infectious virus and DIPs likely result in much more uniform particle distributions. Both the single-cell yield and plaque growth results strongly indicate that a single DIP or even 10 DIPs are rarely able to completely shut down virus production, but that infectious virus production is significantly and fairly uniformly reduced. Unlike the results of Sekellick and Marcus, we do not see indications of viruses that are able to escape the effects of the DIPs (i.e. outliers producing average amounts of virus).

The decrease in maximum viral reporter intensities mirrors the decrease we see in viral yields. Unlike our infectious virus yields, we detect a much higher percentage of cells that appear to be 'non-producers' based on viral protein expression. Seventy percent of cells co-infected with infectious virus and an MO-DIP of 10 did not produce detectable levels of viral reporter protein in microwell experiments (Table 4.3-1). Based on our single-cell virus yield experiments, we expect that viral reporter protein is produced, but the small amounts necessary to produce viral particles on the order of 10s is not detectable at 4x magnification. We did not observe any RFP- cells when imaging the isolated single-cells in 96-well plates at 10x magnification.

In addition to the nearly 2 order of magnitude drop in average maximum intensities that occurs between MO-DIP 0 and MO-DIP 10, we also observe significant changes in viral protein production rates and delay-times. While there is a great deal of variability in single-cell virus kinetics, we noted during our analysis that the general shape of the reporter protein trajectories changed depending on the MO-DIP, from very fast kinetics with short rise-times at MO-DIP 0 to longer and slower reporter production kinetics at the higher MO-DIPs. To demonstrate this difference, we have compiled the average trajectories from the single-cell 'populations' (Figure

4.4-1). Co-infection with DIPs clearly disrupts the normal pattern of VSV replication in BHK cells.

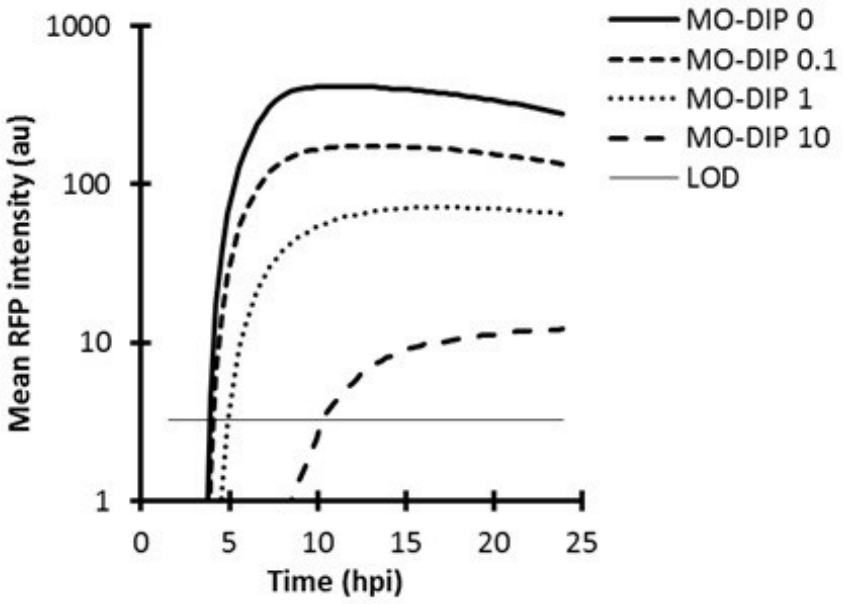

Figure 4.4-1: 'Single-cell' population reporter expression kinetics. The limit of detection shown does not apply to these averages, which have already been thresholded – the LOD is just shown to demonstrate where we would begin to detect the signal if these average trajectories had been from a single-cell.

The primary differences between infections in the absence of DIPs and high MO-DIP infections appears to be the delay-times and maximum intensities; however, we showed in Figure 4.3-8 that the lower protein production rates in MO-DIP 1 and 10 influence the delay-times. While the exact mechanisms of DIP interference are not known, the primary theory states that DI genomes take the viral replication resources and structural protein resources away from the replication of infectious virus genomes. Robust VSV mRNA transcription and protein translation does not occur until enough nucleoprotein is created to switch to genome replication. More genomes and polymerases are required to produce the level of viral protein and genomes

characteristic of this rapidly growing virus. Therefore, we suggest that the majority of infectious virions are produced shortly after the switch to replication, but then the majority of protein resources produced is soon shifted to produce the DI genomes and particles. When comparing the reporter protein produced in isolated single cells with the infectious virus produced, we see that DIP co-infected cells follow a different pattern than cells infected only with wild-type VSV (Figure 4.3-4). The DIP co-infected cells produce less infectious virus than would be predicted by the maximum RFP signal quantified from these cells. We have approximated the number of DIPs produced by assuming two DIPs can be formed using the protein resources of one full length particle. To approximate the DIP production, we must assume that the viral RFP remains a reliable indicator of viral protein production in individual cells even when co-infected with DIPs. We believe this assumption is valid for two reasons: first, the DIPs in our stocks should not be transcriptionally active based on their structure; and second, there is no mechanism we are aware of that would regulate translation of the RFP gene. The approximate amount of DIPs and full length particles produced by cells co-infected at MO-DIP 10 was on average less than 100 total particles, while the total particle count at MO-DIP 1 was nearly 1000 particles per cell. The reason for this difference interests us because previous work in our group has shown that the total particle count remains fairly constant, except at very high DIPs (~ 100 DIP/cell) (Akpinar n.d.). This property of DIP co-infections appears to hold at lower MO-DIPs, but at MO-DIP 10 the amount of viral protein produced based on the reporter signal appears to be insufficient to produce large numbers of DIP particles. While self-interference of DIPs is generally thought to occur at much higher DIP to infectious virus ratios, we suggest that DIP production is limited at MO-DIP 10 in the work presented here and further suggest that the source of the limitation is the limited number of transcriptionally active genomes available to make viral mRNA and thus

protein. More work needs to be done to measure the total particle production from single-cells co-infected with DIPs and to determine the source of what appears to be limiting protein production.

Single-cell techniques have the unique ability to characterize the variability in infectious virus and DIP co-infections and connect parameters such as protein kinetics with viral and DIP yields. It is vital to be able to completely characterize the mechanism of DIP production and interference to better understand how these particles can be used in the formation of vaccines and also to better understand the role of DIPs in naturally occurring infections.

4.5 Acknowledgements

The work presented here was done in collaboration with Fulya Akpinar.

4.6 References

1. **Adang, L. a, C. H. Parsons, and D. H. Kedes**. 2006. Asynchronous progression through the lytic cascade and variations in intracellular viral loads revealed by high-throughput single-cell analysis of Kaposi's sarcoma-associated herpesvirus infection. Journal of Virology 80:10073–10082.

2. **Bellett, D.** 1959. Some Properties of the Transmissible Interfering Component of Vesicular Stomatitis 498–509.

3. **Brinton, M. A.** 1982. Characterization of West Nile virus persistent infections in genetically resistant and suceptible mouse cells 98:84–98.

4. **Cave, D. R., F. M. Hendrickson, and a S. Huang**. 1985. Defective interfering virus particles modulate virulence. Journal of virology 55:366–73.

5. **Holland, J. J., and L. P. Villarreal**. 1974. Persistent noncytocidal vesicular stomatitis virus infections mediated by defective T particles that suppress virion transcriptase. Proceedings of the National Academy of Sciences of the United States of America 71:2956–60.

6. **Huang, A., and D. Baltimore**. 1970. Defective viral particles and viral disease processes. Nature 226:325–327.

7. **Kirkwood, T. B., and C. R. Bangham**. 1994. Cycles, chaos, and evolution in virus cultures: a model of defective interfering particles. Proceedings of the National Academy of Sciences of the United States of America 91:8685–9.

8. **Lancaster, M. U., S. I. Hodgetts, J. S. Mackenzie, and N. Urosevic**. 1998. Characterization of Defective Viral RNA Produced during Persistent Infection of Vero Cells with Murray Valley Encephalitis Virus. Journal of Virology 72:2474–2482.

9. **Lazzarini, R., J. Keene, and M. Schubert**. 1981. The origins of defective interfering particles of the negative-strand RNA viruses. Cell 26:145–154.

10. **Li, D., W. B. Lott, K. Lowry, A. Jones, H. M. Thu, and J. Aaskov**. 2011. Defective interfering viral particles in acute dengue infections. PloS one 6:1–12.

11. **Mann, A., A. C. Marriott, S. Balasingam, R. Lambkin, J. S. Oxford, and N. J. Dimmock**. 2006. Interfering vaccine (defective interfering influenza A virus) protects ferrets from influenza, and allows them to develop solid immunity to reinfection. Vaccine 24:4290–6.

12. **Marriott, A. C., and N. J. Dimmock**. 2010. Defective interfering viruses and their potential as antiviral agents 51–62.

13. **Noble, S., L. McLain, and N. J. Dimmock**. 2004. Interfering vaccine: a novel antiviral that converts a potentially virulent infection into one that is subclinical and immunizing. Vaccine 22:3018–25.

14. **Pesko, K. N., K. a Fitzpatrick, E. M. Ryan, P.-Y. Shi, B. Zhang, N. J. Lennon, R. M. Newman, et al.** 2012. Internally deleted WNV genomes isolated from exotic birds in New Mexico: function in cells, mosquitoes, and mice. Virology 427:10–7.

15. **Schmaljohn, C., and C. D. Blair**. 1977. Persistent infection of cultured mammalian cells by Japanese encephalitis virus. Journal of virology 24:580–9.

16. **Sekellick, M., and P. Marcus**. 1980. Viral interference by defective particles of vesicular stomatitis virus measured in individual cells. Virology 104:247–252.

17. **Stauffer Thompson, K. a, G. a Rempala, and J. Yin**. 2009. Multiple-hit inhibition of infection by defective interfering particles. The Journal of general virology 90:888–99.

18. **Szathmáry, E.** 1993. Co-operation and defection: playing the field in virus dynamics. Journal of theoretical biology 165:341–356.

19. **Timm, A., and J. Yin**. 2012. Kinetics of virus production from single cells. Virology 424:11–7.

20. **Timm, C., F. Akpinar, and J. Yin**. n.d. Quantitative characterization of defective virus emergence by deep sequencing.

21. **Tsai, K.-N., S.-F. Tsang, C.-H. Huang, and R.-Y. Chang**. 2007. Defective interfering RNAs of Japanese encephalitis virus found in mosquito cells and correlation with persistent infection. Virus research 124:139–50.

22. **Warrick, J., A. Timm, A. Swick, and J. Yin**. n.d. A massively-parallel, pipette-based platform for single-cell kinetic studies of virus-host interactions. PloS ONE in prep.

23. **Whelan, S. P. J., and G. W. Wertz**. 1997. Defective Interfering Particles of Vesicular Stomatitis Virus: Functions of the Genomic Termini. Seminars in Virology 8:131–139.

24. **Zhu, Y., J. W. Warrick, K. Haubert, D. J. Beebe, and J. Yin**. 2009. Infection on a chip: a microscale platform for simple and sensitive cell-based virus assays. Biomedical microdevices 11:565–70.

Chapter 5: Suggestions for Future Projects

5.1 Summary of accomplished work

In the first few chapters new methods were detailed describing techniques used to study virus infections in isolated single cells. A few examples of the types of information one can obtain using our high-throughput single-cell platform were discussed. We demonstrated in Chapters 2 and 3 that using single-cell analyses, one can take advantage of the naturally occurring heterogeneity in virus-host systems to understand the importance of the relative timing of immune activation and virus replication processes. We have evidence based on our IFIT2 reporter protein that the extent of anti-viral cytokine production may be limited when VSV replication processes start very quickly, even when the strain of VSV used is a mutant that is not able to shut down the host-response. Likewise, we demonstrated that host immune activation can limit viral protein production and likely inhibits virus production at many stages during the infection processes. Using interferon pre-treatments, we showed that a few hours of forewarning before infection hugely affects virus production. We observed decreases in virus protein production with 3-hours of IFN-β pre-treatment, but the anti-viral effects were much more extensive when the cells were exposed to IFN-β for 6 hours before infection. Some of this information can be gathered using traditional population level measures, but much more information can be gathered using single-cell techniques. For example, we can distinguish potentially important sub-populations of cells that are strongly activated and activated before we detect virus replication. We observed many cells that produced viral reporter intensities far exceeding the average at the mock IFN-β pre-treatment conditions, showing that activation of the type-I interferon pathway does not uniformly affect virus production. We further observed that

those IFN-β pre-treated cells producing high amounts of viral reporter protein were usually in the population of cells in which we detected the viral reporter before the cellular reporter. At that duration of IFN-β exposure, those cells expressing the viral RFP before the cellular GFP were in the minority.

Another application for our high-throughput single-cell infection platform was discussed in Chapter 4. Defective interfering particles (DIPs) are viral sub-species, created by many different types of viruses during replication. DIPs are formed due to some error during virus replication, and are nearly identical to the viruses they were created from in structure, but their genomes are defective, often missing several genes required for replication. These defective particles are called interfering particles because when they co-infect a cell containing infectious virus, the protein and replication resources created by the infectious virus are effectively stolen away by defective genomes for their own replication. The result is a decrease or elimination of infectious virus production from those co-infected cells. Historically, for the purposes of DIP quantification via the interference assay, it has been assumed that a single DIP is sufficient to prevent infectious virus production. Previous work measuring infectious virus from cells believed to be infected with a high multiplicity of DIPs showed that infectious virus could in fact be produced from DIP co-infected cells; however, these results showed that DIP co-infected cells were capable of producing thousands of infections virus particles (Sekellick 1980). Our results contradict those made by Sekellick and Marcus. We have confirmed that DIP co-infected cells are capable of infectious virus production, and we actually observe at least some infectious virus production in nearly every DIP co-infected cell. However, we did not observe any cells that produced average amounts of VSV (~1000 – 10,000 PFU/cell). The highest producing cell infected at a high MO-DIP produced less than 200 infectious units. Further, our high-throughput microwell results

showed that co-infected cells only produced low levels of viral RFP. These results strongly suggest that DIP co-infections of VSV in BHK cells always inhibit virus production, but rarely eliminate virus production. We are not assuming this relationship holds for DIPs of other forms, or DIPs created from other viruses, but our methods may be useful for more thorough characterization of DIP interference.

Single-cell analyses allow us to obtain unique information. The methods we have developed thus far have one very important limitation and that is that we cannot efficiently quantify virus yields from a large number of isolated cells. We are able to quantify virus production from single-cells using the low-throughput, manual experimental techniques, but we are limited in the number of cells that can be analyzed for two reasons. First, the cells must be manually identified, which requires a lot of time and must be done within a few hours of infection while the cells are still adherent. The second limitation is the method of quantification, which is the plaque assay. For large sample numbers, plaque assays become extremely time consuming and also quite expensive for the amount of information they provide. While we have shown that our virus reporter is a very good estimate of actual virus production, we have also shown that there are reasons for a mismatch between maximum virus reporter expression and virus yields. The results of the IFN-β treated PC3 cells showed that cells that undergo lysis often produce fewer virus particles than would be predicted by the viral RFP expression. We also found that DIP co-infections altered the ratio of RFP intensity to yields because the viral protein resources are being shared between infectious particles, which are counted during a plaque assay, and DIP particles which are not. Therefore, the next priority of this project is a fast and inexpensive method of virus quantification for single-cells. The following sections detail our plan to accomplish this goal and demonstrate the applications of such an improvement.

5.2 High-throughput virus quantification

The ability to quantify actual virus yields is the most important component of any high-throughput cell based viral assay; however, this is a very difficult feat to accomplish. There are several high-throughput methods for virus quantification including flow-cytometry, qPCR, and some Coulter Counter type devices such as the qViro. These methods all have certain advantages and disadvantages, but the primary limitation shared by all these methods is that quantification can only be done using high total numbers of virus particles. The lower limit of detection for these methods is simply too high to apply to the single-cell measures we are interested in (Joelsson 2010; Grigorov 2011). There have been many advances in single-cell qPCR, but these assays are made to target intracellular species (Li 2009; McWilliam Leitch 2013). We are not aware of any single-cell qPCR techniques that can accurately quantify virus production from single-cells in a high-throughput way.

There is a need for methods that can detect very dilute concentrations of virus. We hope to apply these techniques to our assay, but they were originally developed for bio-defense purposes. Biosensors are needed to quantify minute amounts of highly pathogenic biological agents in our environment. Professor Selim Unlu's group at Boston University has developed an extremely sensitive, optical, label-free sensing technique which they have called interferometric reflectance imaging sensor, or IRIS. The most well know optical, label-free sensing technology is surface plasmon resonance (SPR). IRIS is a different type of technology, but has similar sensitivity to SPR (Ozkumur 2008).

We have worked with Professor Unlu's group to adapt their technology to work with our high-throughput, single-cell infection platform. The following sections describe the protocols that we have developed and show some preliminary results. Briefly, we are provided with silicon oxide wafers spotted with covalently bound anti-VSV antibody and use these wafers to seal our microwell devices instead of using a glass slide. Virus is produced by infected cells in the microwells, diffuses up to the surface, and binds the antibody. At the end of infection, we separate the wafer from the PDMS device, proceed through a washing protocol, and then ship the wafers to our collaborators in Boston for analysis. The device setup with and without the wafer is shown in Figure 5.2-1.

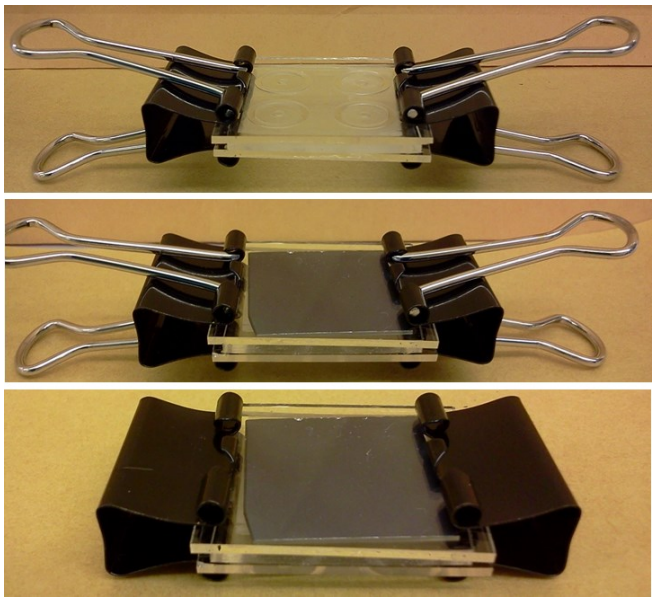

Figure 5.2-1: Device setup for single-cell virus quantification experiments. (top) PDMS device sandwiched between two glass slides and held together with binder clips. (middle) PDMS device sealed with the silicon oxide wafer and sandwiched between two glass slides. (bottom) The arms of the binder clips raise the imaging plain too high for our automated stage. Removing the arms makes automated imaging possible and provides a more stable base so that the devices do not shift as the stage moves.

5.2.1 Interferometry virus quantification

5.2.1.1 Wafer functionalization

The preparation of the silicon oxide wafers used in these experiments have been described (Cretich 2004; Pirri 2004). Briefly, the wafers used in these experiments are made by thermally growing a completely uniform, smooth, and flat silicon dioxide layer on a silicon wafer. A copolymer composed of (N,N-dimethylacrylamid (DMA)-acryloyloxysuccinimide (NAS))-3(trimethoxysilyl)-propyl methacrylate (MAPS) is adsorbed to the silicon dioxide surface. Two of the components, DMA and MAPS, ensure good adsorption and stability, while the NAS component allows for covalent attachment of antibody through primary amine groups. Anti-VSV antibody is spotted in an array on the wafer, which was left in a humid chamber overnight, and then washed and sonicated (Lopez 2011).

5.2.1.2 Experimental Setup

The infection procedures are the similar to those described in the previous three chapters, but the microwells of the device are sealed with a silicon oxide wafer. Additionally, the dark background of the silicon oxide wafer makes it impossible to locate the microwells using phase contrast images. Therefore, we use a FITC-labeled dextran for this purpose and for image registration. The FITC-dextran is added to media (~0.6 µl/ml) and is used for the post-seeding washing steps. The device 'sandwich' is composed of a glass slide base, the PDMS microwell device, the silicon oxide wafer, and another glass slide. Pressure is applied using two binder clips (Figure 5.2-1). After sealing of the device, the arms of the binder clips are removed and the device sandwich placed in an Omni Trey surrounded by sterile PBS soaked Kimwipes

(Kimberley Clark). It is extremely important that the sandwich device is never inverted once sealed. The device is imaged as described in previous chapters, but instead of collecting phase contrast images, we collect green channel image to visualize the FITC-Dextran filled wells.

5.2.1.3 Silicon-oxide wafer washing and shipment preparations

After the infection period is complete, the antibody-coated silicon-oxide wafer must be washed and prepped for shipment to our collaborators at Boston University. The arms are re-inserted into the binder clips, then the device is submerged in PDMS before the pressure is released and the wafer is separated from the PDMS device. To ensure a clean wafer with no cross-contamination, it is necessary for the wafer to remain wet throughout the washing steps. Three PBS washes of 3 minutes each are performed, then a one minute wash in 10% PBS, followed by a rinse in sterile Milli-Q water before drying. Any excess water droplets left on the wafer are immediately removed using a can of compressed gas (3M) inside the bio-safety cabinet. The wafers are exposed to UV light for 60 minutes to inactivate the virus adsorbed to the silicon-oxide wafer so that they are safe for shipping.

5.2.1.4 Virus quantification

The general detection method is based on the quantification of a change in wafer thickness. IRIS uses three LED illumination wavelengths of 450, 525, and 635 nm and a 50x NA=0.9 objective. The light is scattered by bound particles and reflected back, providing a signal that can be used to detect individual particles and also estimate the aspect ratio of those particles. Prior to the high magnification virus quantification, low magnification scans of the silicon wafers are performed. An example is shown in Figure 5.2-2. The wafers are spotted with anti-VSV antibody

prior to experiments. The array of antibody spots is easily seen in Figure 5.2-2. Where these spots cover microwells containing infected cells, we are able to see clear evidence of antibody bound virus particles. By aligning the mirror image of the wafer with our fluorescent images, we are able to match up microwells in which we detect a positive viral RFP signal and a positive virus particle signal. That alignment is shown in Figure 5.2-2. In this manner, we can identify microwells containing isolated single-cells and microwells containing no cells to scan at high magnification for analysis. The process of quantifying the virus produced in this experiment is ongoing. Also in progress is a method to align, or register the signal from these two measurements in an unbiased way (5.2.2.1).

The experiment shown in Figure 5.2-2 is of BHK cells infected with N1-DSRed or co-infected with N1-DSRed and DIPs (Chapter 4). IRIS is capable of distinguishing individual virus particles and by using interference patterns from targets exposed to three wavelengths of LED light, our collaborators are able to determine the aspect ratio of the particle. We have provided Professor Unlu's group with inactivated stocks of our N1-DSRed virus and corresponding DIPs and they have successfully been able to differentiate the two types of particles (data not shown). Preliminary work indicates that their ability to accurately quantify the size of these particles is concentration dependent. It may be possible to identify single-cell wells that have produced particles of different sizes characteristic of either DIPs or infectious particles.

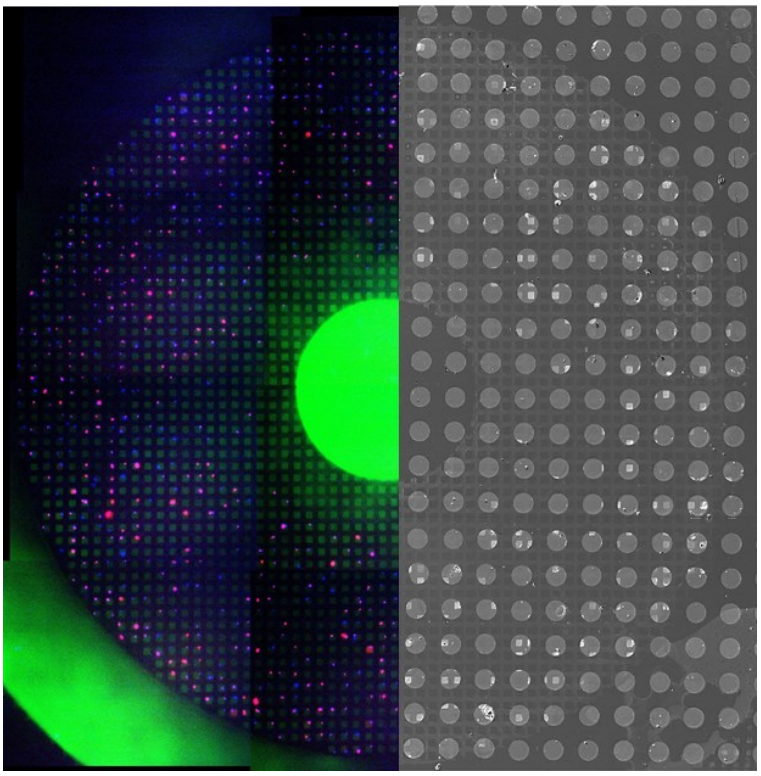

Figure 5.2-2: Fluorescent image data and virus production data. On the left is a stitched overlay image of a bull's-eye seeded with N1-DSRed infected BHK cells. The green signal is from a FITC-labeled dextran we use to visualize the microwells when phase contrast images cannot be acquired. On the right is a low magnification scan of the silicon-oxide wafer that sealed the bull's-eye for 24 hours. Notice the residue left by the PDMS that allows us to visualize the microwell locations. The array of circles observed in the wafer image is the antibody spot array. Antibody arrayed wafer image provided by George Daaboul, PhD.

5.2.2 Future device and protocol improvements

5.2.2.1 Device registration

Currently, it is necessary to scan large sections of the silicon wafer at a low magnification so that we can recognize patterns in the PDMS residue and in detection of virus production. These scans take a lot of time and are not use for virus quantification. After the scans are finished, areas

of interest can be identified and measured using higher magnification detection. To eliminate the low magnification scan, we will introduce modifications to the PDMS device so that the detection location can be identified more readily at high magnification. A pattern of rotated microwells will be introduced in a variable manner through-out each bull's-eye (Figure 5.2-3).

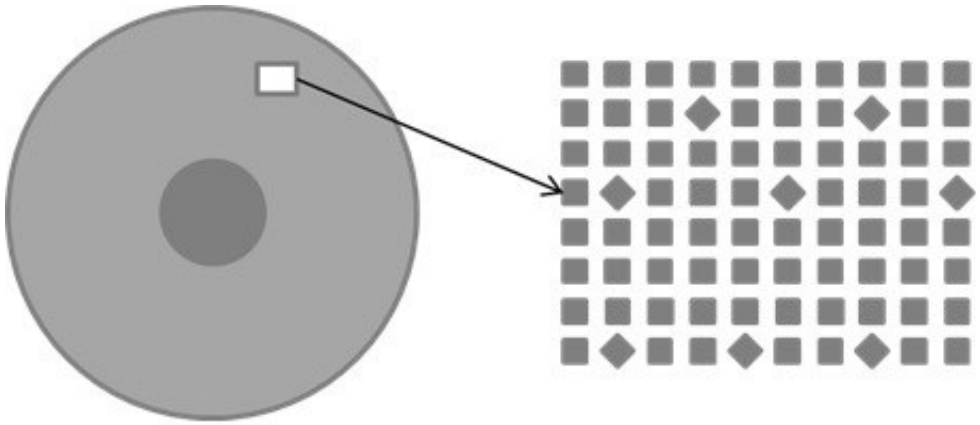

Figure 5.2-3: Example pattern to be introduced into microwell array.

Preliminary experiments have shown that the amount of virus often produced in VSV infections saturates the IRIS signal. Some work has been done to modulate virus production over a wide range in order to determine the upper limit of detection. We are considering increasing the microwell size to limit of the frequency of saturation.

5.2.2.2 Clamping mechanism

The binder clips that add pressure to keep the device sealed are an ideal size for the smaller devices used in these experiments. We place these devices in an Omni Trey for imaging, and using small binder clips we are just barely able to bring the cells into focus. Using the automated stage at this focal plane often results in errors during the time-lapse. The automated stage simply

does not handle this stress well, and so a new clamping mechanism or recessed holder for the binder clip system needs to be devised for future experiments.

5.2.2.3 Kinetic measures of virus particle production

Professor Unlu's group is working on a method to perform IRIS analyses using a clear substrate instead of the opaque silicon oxide wafer. If they are successful, it will be possible to measure virus attaching to a surface over-time. They believe the only instrument requirements will be an LED or laser based light source and a perfect focus system that can automatically focus to the desired surface. Our lab has access to a fluorescent microscope with these properties and so we may soon be able to perform these experiments.

5.3 Application for high-throughput single-cell infection assay

Thus far we have demonstrated the type of data we can obtain using our single-cell infection assay including effects of innate immunity on virus-host interactions and effects of DIP co-infections on viral protein production. The microwell based platform makes our assay very adaptable for general cell-based screening assays as well. Our microwell device has an advantage over most in that it is separated into different bull's-eye sections, which allow one to perform analyses on cell populations treated under different conditions. These different experiments can be performed in parallel without risk of cross-contamination.

5.3.1 Drug resistance

RNA viruses mutant very rapidly, often developing resistance to anti-viral drug treatments. Deep sequencing techniques can be used to characterize the genetic variability in a virus

population, but quantifying virus production from infections is the best way to determine inhibitory effects of anti-viral drugs. It is estimated that rate of mutation during VSV replication is equivalent to ~ 1 mutation per genome (Drake 1999).

5.3.1.1 Proof of concept experiments

The frequency at which we are able to detect phenotypic mutants in our single-cell infections implies that we may more easily be able to find desired mutants than would be possible through population level selection. Our group has used the mutagens 5-fluorouracil and Ribavirin in the development of drug-susceptibility assays (Zhu 2007; Zhu 2009a; Lindsay 2011). These drugs are used as broad-spectrum anti-virals in research and function by inducing error catastrophe in the already error prone replication of RNA viruses. Published protocols for selecting for drug resistant VSV mutants to these mutagens suggest that months of passaging under selection pressure might be required to create such a stock (Cuevas 2005; Sierra 2007). Creating drug-resistant stocks is necessary for proof of concept experiments to show our assay can identify drug resistant mutants. I believe that by performing low-throughput, low cell-density infections under a high-dose of drug, finding resistant mutants may be relatively fast and easy compared to selection through passaging.

Once a drug-resistant stock is created, we can combine this stock with our normal virus stocks in different ratios to infect cells in solution. The infections will proceed in microwells under high doses of the drug. The result of drug-screens using the microwell system will result on the mode of action of the drug. With these mutagens, the effects may vary greatly. Mutations acquired by nascent genomes may be sufficient to reduce secondary transcription and affect

protein production noticeably. However, the effect may not be evident without spread of the infection. We have attempted infection spread experiments previously by mixing infected cells with un-infected cells, but we could not distinguish the cell populations because of cell staining issues. Improvements in cell labeling methods will make these experiments, and many others possible (Yamanaka 2012).

5.4 Cell-signaling and virus protein production and yields

In Chapter 2 we suggested that immune activation of PC3 cells might initially be beneficial for VSV replication due to increased transcriptional and translation activity within the cell. In Chapter 4 we presented data showing that viral yields increase as a function of cell density, and it has been previously shown by our group and others that VSV replication is cell-cycle dependent (Oliere 2008; Zhu 2009b). Cell-cell contact or cell-cell signaling appears to affect VSV protein production and replication, perhaps in many ways. The following is a simple proposal describing methods to elucidate the effects of cell-cell contact and signaling using methods commonly used in our lab.

Recent results indicate that correlations exist between the fluorescent signals emitted from infected cells and the amount of virus produced from those cells. We can see this correlation with N1-DSRed infections of PC3 cells (Figure 5.4-1). The yields from infected cells that reached a plateau in RFP signal correlated very well with the maximum level of RFP expression from each cell. It would be beneficial to know if this correlation remains at population levels where cell-cell signaling has been shown to affect the outcome of virus infections (Figure 4.3-5).

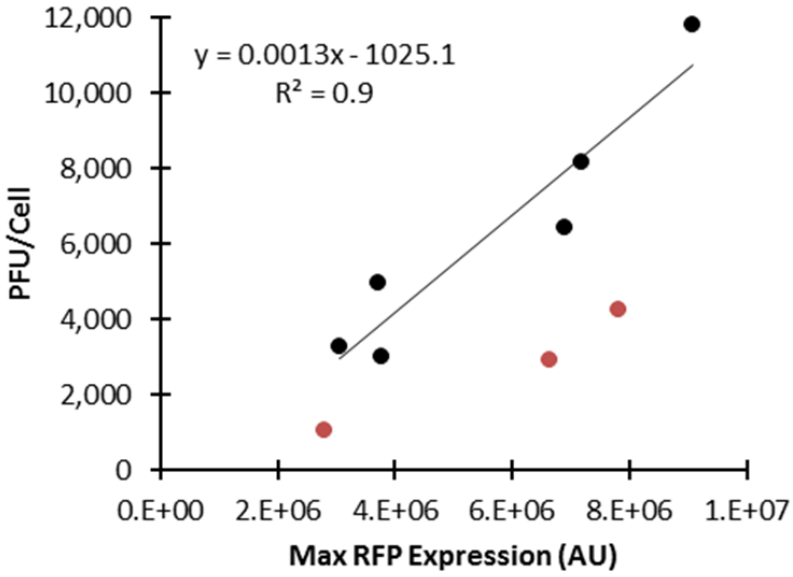

Figure 5.4-1: Maximum virus reporter correlation with viral single-cell yields: This data was shown in part in Chapter 3. Single cells in which the RFP signal from the reporter virus reached a plateau are indicated by black circles. Cells that did not reach a plateau before the end of the experiment and cells that died before reaching a signal plateau are indicated by red circles.

We may be able to explore the effects of cell signaling to a greater extent by using nuclear stains to determine approximate cell state and by studying infections at various cell densities using reporter PC3 cells and the M51R virus. The goal would be to determine if the fluorescent signal from reporter viruses is still correlated to yields at population densities and to explore how cell culture geometry affects virus-host systems (Figure 5.4-3). The techniques that will be used are described below.

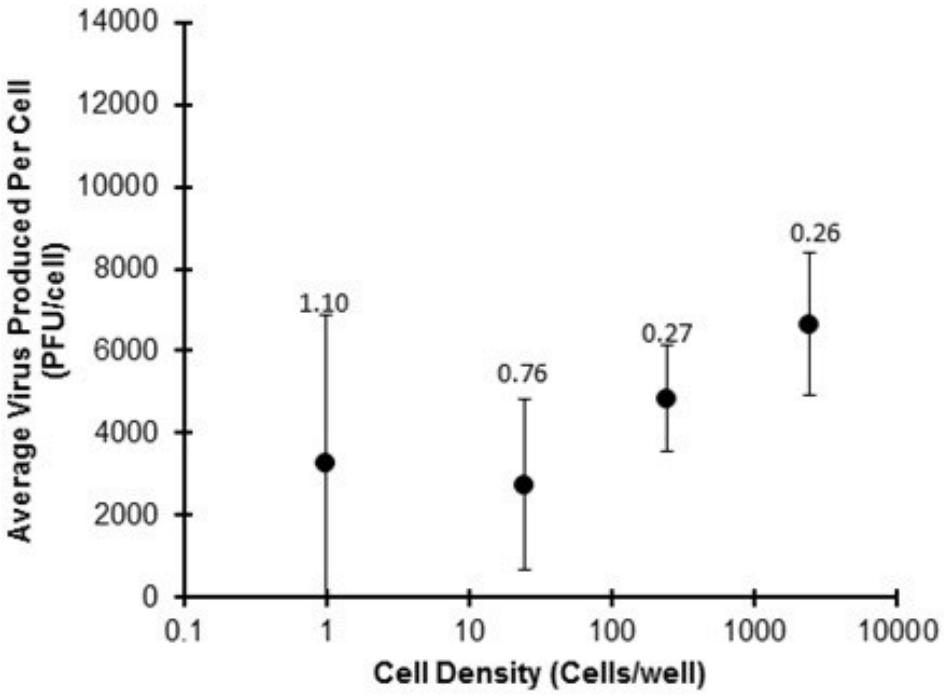

Figure 5.4-2: Average yield per cell vs. cell density. N1-DSRed VSV infections of PC3 cells show increasing yields and decreasing variability as cell density increases. This pattern is the same when using VSV to infect BHK cells (Chapter 4). Number listed above the error bar is the coefficient of variation.

5.4.1 Use in-solution infection technique to control infection parameters in patterned devices.

In previous cell patterning work done by our lab, cells were infected after seeding on patterned slides. This method makes it difficult to control the multiplicity of infection and synchronize the infection. We gain more control over the infection process by performing the infection in solution before adding to patterns. The low-throughput, single-PC3 cells experiments we have done suggests that binding of the newly infected cells to the patterns should not be an issue.

5.4.2 Normalize RFP signal to purified protein standard and correlate RFP expression to yields

In order to compare the viral RFP signal across different experiments, we must normalize the reporter signal to a protein standard. Serial dilutions of known concentrations of purified fluorescent protein stock confined in a space with equal height to an average cell can be used to determine a signal to protein molecule standard (Wells 2008). Our current commercial protein stock is not concentrated enough for this assay, but there may be other sources.

We will set up these experiments so that the supernatants can be collected and quantified. Through a collaboration with Professor Unlu's group at Boston University, we should soon be able to quantify virus production from cells in microwells. Isolated single-cell results may also be obtained via low-throughput experiments, by seeding individual cells in wells of 96-well plates. Figure 5.4-1 shows us that there might be multiple correlations depending on the phenotype of the infection.

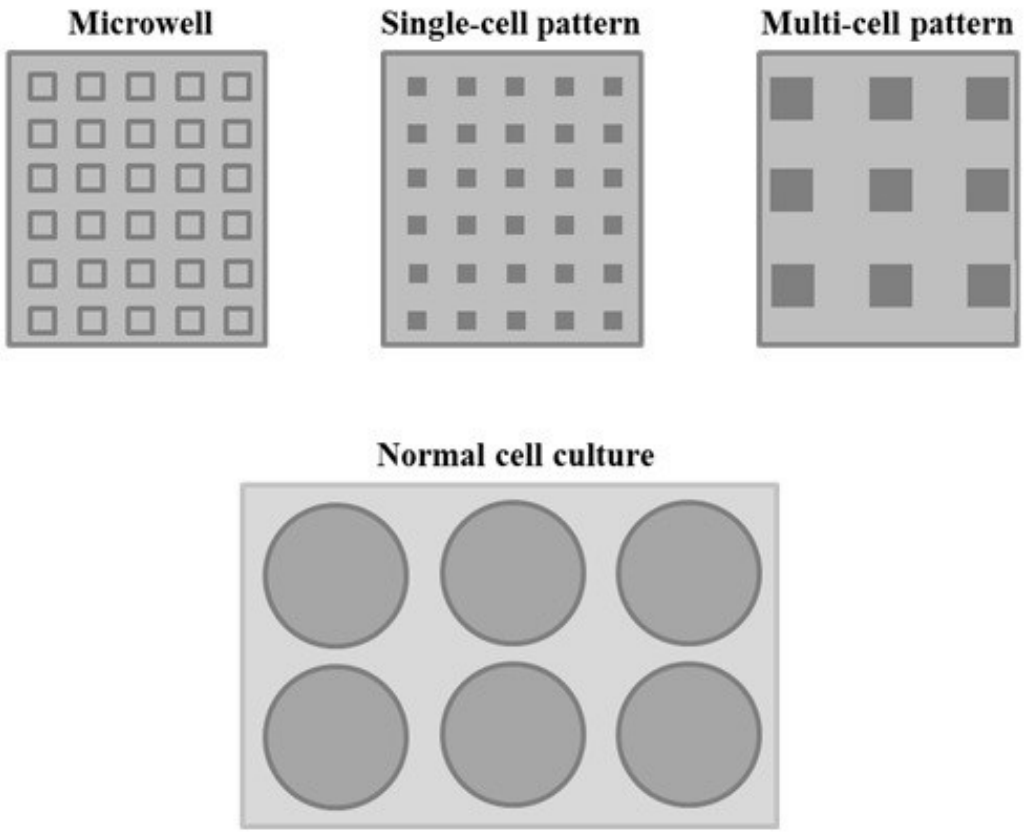

Figure 5.4-3: Diagram of various cell culture environments. Microwells isolate both cells and cell signals; the single-cell pattern eliminate cell-cell contact, but permits cell-cell signaling; the multi-cell pattern allows both cell-cell contact and signaling and is similar to a normal cell culture plate.

5.5 References

1. **Cretich, M., G. Pirri, F. Damin, I. Solinas, and M. Chiari**. 2004. A new polymeric coating for protein microarrays 332:67–74.

2. **Cuevas, J. M., R. Sanjuán, A. Moya, and S. F. Elena**. 2005. Mode of selection and experimental evolution of antiviral drugs resistance in vesicular stomatitis virus. Infection genetics and evolution journal of molecular epidemiology and evolutionary genetics in infectious diseases 5:55–65.

3. **Drake, J. W., and J. J. Holland**. 1999. Mutation rates among RNA viruses. Proceedings of the National Academy of Sciences of the United States of America 96:13910–13913.

4. **Grigorov, B., J. Rabilloud, P. Lawrence, and D. Gerlier**. 2011. Rapid titration of measles and other viruses: optimization with determination of replication cycle length. PloS one 6:1–12.

5. **Joelsson, D., I. V Gates, D. Pacchione, C. J. Wang, P. S. Bennett, Y. Zhang, J. McMackin, et al.** 2010. Rapid automation of a cell-based assay using a modular approach: case study of a flow-based Varicella Zoster Virus infectivity assay. Journal of virological methods 166:1–11.

6. **Li, Y., X. Huang, B. Xia, and C. Zheng**. 2009. Development and validation of a duplex quantitative real-time RT-PCR assay for simultaneous detection and quantitation of foot-and-mouth disease viral positive-stranded RNAs and negative-stranded RNAs. Journal of virological methods 161:161–7.

7. **Lindsay, S. M., A. Timm, and J. Yin**. 2011. A quantitative comet infection assay for influenza virus. Journal of Virological Methods 179:351–358.

8. **Lopez, C. a, G. G. Daaboul, R. S. Vedula, E. Ozkumur, D. a Bergstein, T. W. Geisbert, H. E. Fawcett, et al.** 2011. Label-free multiplexed virus detection using spectral reflectance imaging. Biosensors & bioelectronics 26:3432–7.

9. **McWilliam Leitch, E. C., and J. McLauchlan**. 2013. Determining the cellular diversity of hepatitis C virus quasispecies by single-cell viral sequencing. Journal of virology 87:12648–55.

10. **Oliere, S., M. Arguello, T. Mesplede, V. Tumilasci, P. Nakhaei, D. Stojdl, N. Sonenberg, et al.** 2008. Vesicular stomatitis virus oncolysis of T lymphocytes requires cell cycle entry and translation initiation. Journal of Virology 82:5735–5749.

11. **Ozkumur, E., J. W. Needham, D. a Bergstein, R. Gonzalez, M. Cabodi, J. M. Gershoni, B. B. Goldberg, et al.** 2008. Label-free and dynamic detection of biomolecular

interactions for high-throughput microarray applications. Proceedings of the National Academy of Sciences of the United States of America 105:7988–92.

12. **Pirri, G., F. Damin, M. Chiari, E. Bontempi, and L. E. Depero**. 2004. Characterization of a polymeric adsorbed coating for DNA microarray glass slides. Analytical chemistry 76:1352–8.

13. **Sekellick, M., and P. Marcus**. 1980. Viral interference by defective particles of vesicular stomatitis virus measured in individual cells. Virology 104:247–252.

14. **Sierra, M., A. Airaksinen, C. González-López, R. Agudo, A. Arias, and E. Domingo**. 2007. Foot-and-mouth disease virus mutant with decreased sensitivity to ribavirin: implications for error catastrophe. Journal of virology 81:2012–24.

15. **Wells, A. L., J. S. Condeelis, R. H. Singer, and D. Zenklusen**. 2008. Single-Molecule Techniques. (P. R. Selvin & T. Ha, eds.) (pp. 233–235). John Inglis.

16. **Yamanaka, Y. J., G. L. Szeto, T. M. Gierahn, T. L. Forcier, K. F. Benedict, M. S. N. Brefo, D. A. Lau, et al.** 2012. Cellular Barcodes for E ffi ciently Pro fi ling Single-Cell Secretory Responses by Microengraving.

17. **Zhu, Y., J. W. Warrick, K. Haubert, D. J. Beebe, and J. Yin**. 2009a. Infection on a chip: a microscale platform for simple and sensitive cell-based virus assays. Biomedical microdevices 11:565–70.

18. **Zhu, Y., and J. Yin**. 2007. A quantitative comet assay: imaging and analysis of virus plaques formed with a liquid overlay. Journal of Virological Methods 139:100–102.

19. **Zhu, Y., A. Yongky, and J. Yin**. 2009b. Growth of an RNA virus in single cells reveals a broad fitness distribution. Virology 385:39–46.